Massive Star Geriatrics

DISSERTATION

Presented in Partial Fulfillment of the Requirements for the Degree Doctor of Philosophy in the Graduate School of The Ohio State University

By

Rubab Khan

Graduate Program in Astronomy

The Ohio State University

2014

Dissertation Committee:

Professor Krzysztof Stanek, Advisor

Professor Christopher Kochanek

Professor John Beacom

Abstract

In this dissertation, I present a series of observational studies investigating how mass loss from massive stars affects their evolution in the last stages of life prior to death by core-collapse.

First, I carry out a mid-infrared photometric search for massive, luminous, self-obscured stars similar to the dust-obscured progenitors of the luminous outbursts in NGC 6946 (SN 2008S) and NGC 300 in 2008 at the extreme end of the AGB sequence in four nearby galaxies: M 33, NGC 300, M 81, and NGC 6946. I verified that stars analogous to the progenitors of these two transients are truly rare in all four galaxies with only ~ 1 such object existing in any galaxy at a time.

Next, I present the discovery of a previously unknown luminous star in M 33 that we dubbed "Object X" — the brightest mid-infrared star in M 33. I propose that Object X is a $M \gtrsim 30 M_\odot$ evolved star obscured in its own dust ejected during episodic mass loss events over at least ~half a century. It may emerge from its current ultra-short evolutionary phase as a hotter, post red supergiant star.

Finally, I present the results of a mid-infrared search in 7 nearby ($\lesssim 4\,$Mpc) galaxies using *Spitzer* IRAC images for analogs of $\eta\,$Carinae, the most massive

(100-150 $M_\odot$) and most luminous ($\sim 3 \times 10^6\, L_\odot$) star to have gone through an eruption in recent times. I identified an emerging class of 18 luminous, heavily obscured, evolved massive stars that have luminosities $\log(L/L_\odot) \simeq 5.5 - 6.0$. In this regime, red supergiants may have photospheric instabilities that drive greatly enhanced mass loss as they evolve blue-wards on the Hertzsprung-Russell diagram. The Galactic/LMC/SMC examples are so rare and heterogeneous that there are no good statistics on their abundances, lifetimes or total mass losses. My well defined sample provides an unique opportunity to better understand this tumultuous evolutionary phase towards the end of the lives of the most massive stars.

Dedication

To Bangladesh

Acknowledgments

My implausible journey from the middle class of a country with no institution containing an Astronomy department to writing this thesis has been made possible by the kindness, friendship, and guidance of some truly extraordinary individuals. While I can only name a few of them here, my gratitude is no less to the rest.

I would like to thank my PhD adviser, Kris Stanek, for everything that he has taught me about science and life. Kris has the mindset of an observer and has a strictly empirical evidence driven objectivity unadulterated by theory. While I have learnt as many tricks of the trade and bread-and-butter skills from him over the years as I possibly could, his most important lesson was to make me look at nature as it is. Kris has taught me to “keep things simple, because otherwise it would be complicated”. But I shall not trivialize our relationship to merely that of a mentor-mentee. Kris’s intense non-linear sense of humor brightens the department, and it has always been uplifting for me to have Kris stop by my desk or for me to stop by his, because no matter how the day might be going up to that point, he would always lighten it in some way or other. Kris is someone I can trust and rely on, one who cares no less for my weaknesses — and heaven knows they are way too many — than for my strengths. His constant support in the most difficult hours has kept me going. It has been a privilege to be trained and guided by Kris, and a true honor to have him as a friend.

I am grateful to Chris Kochanek for always being that person who would listen to my every question, and answer every single one of them unfailingly. His constant presence down the hall from 07:14:59.9 to 16:00:00.1 — every, single, day — taught me more about extreme discipline and total dedication than any other experience in my life. I wish to act on this lesson for the years ahead with ever increasing vigor. I must thank Chris for his close scrutiny and excruciatingly detailed near-real-time feedback to my drafts. I have absolutely no doubt that he is the single most efficient physicist of any subtype alive as far as helping students with improving their writing goes, and I can not fathom what I would have done without him.

John Beacom brought the perspective of an outsider who also happens to be an insider. Being an Astrophysicist, rather than either a pure Physicist like Chris or a hardcore Astronomer like Kris, John can always look at any problem at hand from a refreshingly unique perspective. Every time I discussed a concept with him, I walked away with new insights, ideas for making a new figure, and simple explanations of complex concepts. I would like to thank John for the numerous discussions that we have had, and for all his helpful pointers and support along the way.

I would like to thank Szabi Marka, my undergraduate adviser, for molding me from a teenage high school student into a young researcher. In the loneliest years of my life, Szabi was at a time a strict guardian, a caring parent, a friendly sibling, a keen teacher, and an unconditional patron for me. He always treated me as a member of his family, helped me build a strong foundation beginning from absolute zero, and I will forever be in his debt of kindness.

I would like to thank the Columbia University's Global Scholars Program, the Ohio State University's Department of Astronomy, the National Science Foundation, the National Aeronautics and Space Administration, and the US Department of Energy for their financial support over the past ten years. I am grateful to the United States, and specifically to the cities of New York and Columbus, for being such wonderfully hospitable and generous hosts.

But then, there are those who I can thank, and then there are those who I dare not, because any such audacity is sure to prove childishly inadequate for the purpose. They include my mother who always encouraged me to do whatever makes me happy regardless of the enormity of the grief that it would cause her, my father who influenced me in ways that probably only Freud could explain, my brother Ayon (Dr. Lashkar Kashif) who erased the word "impossible" from my life's dictionary, and last but the most, my wife Tithi (Dr. Faiza Faria) who sacrificed more for my career than I can ever make up for.

Vita

October 26, 1986	Born – Dhaka, Bangladesh
2008	A.B., Astrophysics, Columbia University
2010	M.S., Astronomy, The Ohio State University
2008 – 2014	Graduate Teaching and Research Associate.

Publications

Research Publications

1. **R. Khan**, K. Z. Stanek, C. S. Kochanek, J. Gerke. Finding η Car Analogs in Nearby Galaxies Using Spitzer: II. Identification of An Emerging Class of Extragalactic Self-Obscured Stars. In preparation.
2. **R. Khan**. "Possible Spitzer Counterpart of PSN J01364816+1545310". The Astronomer's Telegram, 5230, July 2013.
3. D. Murphy et al. (incl. R. Khan). Detecting Long-Duration Narrow-Band Gravitational Wave Transients Associated with Soft Gamma Repeater Quasi-Periodic Oscillations. Physical Review D, 87, 103008, May 2013.
4. **R. Khan**, K. Z. Stanek, C. S. Kochanek. Finding η Car Analogs in Nearby Galaxies Using Spitzer: I. Candidate Selection. Astrophysical Journal, 767:52, April 2013.
5. C. S. Kochanek, **R. Khan**, X. Dai. "On Absorption by Circumstellar Dust, With the Progenitor of SN2012aw as a Case Study." Astrophysical Journal,759:20, November 2012.

6. R. Assef et al. (incl. R. Khan). Black Hole Mass Estimates Based on CIV are Consistent with Those Based on the Balmer Lines. ApJ, 742:93, December 2011.

7. **R. Khan**, K. Z. Stanek, R. Stoll, J. L. Prieto. Super-Chandrasekhar SNe Ia Strongly Prefer Metal-Poor Environments. Astrophysical Journal Letters, 737:L24+, August 2011.

8. Szczygiel, D.; **Khan, R.**; Kochanek, C. S. "Further Properties of the Candidate Progenitor of SN 2011dh in M51." The Astronomer's Telegram, 3431, June 2011.

9. **R. Khan**, K. Z. Stanek, C. S. Kochanek, A. Z. Bonanos. Object-X: The Brightest Mid-IR Point Source in M33. Astrophysical Journal, 732:43-+, May 2011.

10. J. Abadie et al. (incl. R. Khan). A search for gravitational waves associated with the August 2006 timing glitch of the Vela pulsar. Physical Review D, 83(4):042001-+, February 2011.

11. **R. Khan** et al. Pre-discovery and Follow-up Observations of the Nearby SN 2009nr: Implications for Prompt Type Ia Supernovae. Astrophysical Journal, 726(2):106-+, Jan. 2011.

12. Prieto, J.; **Khan, R.**; Hornochova, P. "M31N 2010-01a and M31N 2010-12c." Central Bureau Electronic Telegrams, 2610, 2, December 2010.

13. Prieto, J.; **Khan, R.**; Garnavich, P.; Pagnini, J.; Yusa, T. "Apparent Nova in M31." Central Bureau Electronic Telegrams, 2594, 1, December 2010.

14. R. M. Humphreys et al. (incl. R. Khan). SN 2010U: A Luminous Nova in NGC 4214. Astrophysical Journal Letters, 718:L43-L47, July 2010.

15. J. Abadie et al. (incl. R. Khan). Search for Gravitational-wave Inspiral Signals Associated with Short Gamma-ray Bursts During LIGO's Fifth and Virgo's First Science Run. Astrophysical Journal, 715:1453-1461, June 2010.

16. B. P. Abbott et al. (incl. R. Khan). Search For Gravitational-wave Bursts Associated with Gamma-ray Bursts using Data from LIGO Science Run 5 and Virgo Science Run 1. Astrophysical Journal, 715:1438-1452, June 2010.

17. **R. Khan** et al. Census of Self-Obscured Massive Stars in Nearby Galaxies with Spitzer: Implications for Understanding the Progenitors of SN 2008S-Like Transients. Astrophysical Journal, 715:1094-1108, June 2010.

18. Hornoch, K.; **Khan, R.**; Bird, J.; Pejcha, O.; Garnavich, P.; Littlefield, C.; Paul, N.; Bouzid, S. "Nova in M31: M31N 2010-05a." CBET, 2319, 1, June 2010.

19. Prieto, J. L.; Bond, H. E.; Kochanek, C. S.; **Khan, R.**; Stanek, K. Z.; Thompson, T. A. "Optical and Near-IR Follow-up of SN 2010da: Evidence for Warm Dust." The Astronomer's Telegram, 2660, June 2010.

20. **Khan, R.**; Stanek, K. Z.; Kochanek, C. S.; Thompson, T. A.; Prieto, J. L. "Mid-IR progenitor of SN 2010da in NGC 300." The Astronomer's Telegram, 2632, May 2010.

21. J. Abadie et al. (incl. R. Khan). All-sky search for gravitational-wave bursts in the first joint LIGO-GEO-Virgo run. Physical Review D, 81(10):102001-+, May 2010.

22. B. P. Abbott et al. (incl. R. Khan). Searches for Gravitational Waves from Known Pulsars with Science Run 5 LIGO Data. Astrophys. Journal, 713:671-685, April 2010.

23. Hornoch, K. et al. (incl. R. Khan). "Apparent Nova in M81: M81N 2010-01c." Central Bureau Electronic Telegrams, 2180, 1, February 2010.

24. Hornoch, K. et al. (incl. R. Khan). "Apparent Novae in M81: M81N 2010-01a and M81N 2010-01b." Central Bureau Electronic Telegrams, 2170, 1, February 2010.

25. Hornoch, K.; Prieto, J.; **Khan, R.**; Pejcha, O. "M31N 2010-01a." Central Bureau Electronic Telegrams, 2136, 1, January 2010.

26. Hornoch, K.; Prieto, J.; **Khan, R.**; Pejcha, O.; Green, D. W. E. "Novae in M81." Central Bureau Electronic Telegrams, 2132, 1, January 2010.

27. Prieto, J. L.; **Khan, R.** et al. "Supernovae 2009ns-2009nx and 2010I-2010M." CBET, 2131, 1, January 2010.

28. Hornoch, K. et al. (incl. R. Khan). "M31N 2010-01a." CBET, 2127, 1, January 2010.

29. Prieto, J.; **Khan, R.** "Supernovae 2010C and 2010D." Central Bureau Electronic Telegrams, 2122, 1, January 2010.

30. **Khan, R.**; Prieto, J. "Supernovae 2009mx and 2009my." Central Bureau Electronic Telegrams, 2120, 1, January 2010.

31. Prieto, J.; **Khan, R.** "Supernova 2010B in NGC 5370." Central Bureau Electronic Telegrams, 2118, 1, January 2010.

32. Prieto, J. L.; **Khan, R.** et al. "MDM classification of CRTS supernova discoveries." ATel, 2388, January 2010.

33. B. P. Abbott et al. (incl. R. Khan). Search for high frequency gravitational-wave bursts in the first calendar year of LIGO's fifth science run. Phys. Rev. D, 80(10):102002-+, November 2009.

34. B. P. Abbott et al. (incl. R. Khan). Search for gravitational-wave bursts in the first year of the fifth LIGO science run. Physical Review D, 80(10):102001-+, November 2009.

35. B. P. Abbott et al. (incl. R. Khan). Search for gravitational wave ringdowns from perturbed black holes in LIGO S4 data. Phys. Rev. D, 80(6):062001-+, September 2009.

36. B. P. Abbott et al. (incl. R. Khan). First LIGO search for gravitational wave bursts from cosmic (super)strings. Physical Review D, 80(6):062002-+, September 2009.

37. B. P. Abbott et al. (incl. R. Khan). Stacked Search for Gravitational Waves from the 2006 SGR 1900+14 Storm. Astrophysical Journal Letters, 701:L68-L74, August 2009.

38. B. P. Abbott et al. (incl. R. Khan). An upper limit on the stochastic gravitational-wave background of cosmological origin. Nature, 460:990-994, August 2009.

39. B. P. Abbott et al. (incl. R. Khan). Einstein@Home search for periodic gravitational waves in early S5 LIGO data. Physical Review D, 80(4):042003-+, August 2009.

40. B. P. Abbott et al. (incl. R. Khan). Search for gravitational waves from low mass compact binary coalescence in 186 days of LIGO's fifth science run. Physical Review D, 80(4):047101-+, August 2009.

41. **R. Khan** and S. Chatterji. Enhancing the Capabilities of LIGO Time-Frequency Plane Searches Through Clustering. Classical and Quantum Gravity, 26(15):155009 (14pp), August 2009.

42. P. Kalmus, **R. Khan**, L. Matone, S. Marka. Search method for unmodeled transient gravitational waves associated with SGR flares. Classical and Quantum Gravity, 24:659-+, October 2007.

43. B. Abbott et al. (incl. R. Khan). Observation of a kilogram-scale oscillator near its quantum ground state. New Journal of Physics, 11(7):073032-+, July 2009.

44. B. Abbott et al. (incl. R. Khan). Search for Gravitational Waves from Low Mass Binary Coalescences in the First Year of LIGO's S5 Data. Phys. Rev. D, 79(12):122001-+, June 2009.
45. B. Abbott et al. (incl. R. Khan). All-Sky LIGO Search for Periodic Gravitational Waves in the Early Fifth-Science-Run Data. Phys. Rev. Letters, 102(11):111102-+, March 2009.
46. B. Abbott et al. (incl. R. Khan). Einstein@Home search for periodic gravitational waves in LIGO S4 data. Physical Review D, 79(2):022001-+, January 2009.
47. B. Abbott et al. (incl. R. Khan). First joint search for gravitational-wave bursts in LIGO and GEO 600 data. Classical and Quantum Gravity, 25(24):245008-+, December 2008.
48. B. Abbott et al. (incl. R. Khan). Search for Gravitational-Wave Bursts from Soft Gamma Repeaters. Physical Review Letters, 101(21):211102-+, November 2008.
49. B. Abbott et al. (incl. R. Khan). Beating the Spin-Down Limit on Gravitational Wave Emission from the Crab Pulsar. Astrophysical Journal, 683:L45-L49, August 2008.
50. B. Abbott et al. (incl. R. Khan). Astrophysically triggered searches for gravitational waves: status and prospects. Class. and Quantum Gravity, 25(11):114051-+, June 2008.

Fields of Study

Major Field: Astronomy

Table of Contents

List of Tables

List of Figures

Chapter 1: Introduction

Deaths of massive stars by core-collapse are associated with some of the highest energy phenomena in the universe such as core-collapse supernovae (ccSNe), long-duration gamma-ray bursts, and Gravitational Wave bursts. They are the source of heavier elements contributing to the chemical enrichment of galaxies and played a crucial role in the metallicity evolution of the early universe through stellar feedback. The physical mechanism, energetics and observed properties associated with these events depend on the structure and terminal mass of the evolved stars at core-collapse, which in turn are determined by stellar mass loss.

Our understanding of the role of episodic mass loss in the final stages of the evolution of massive stars is surprisingly limited. Short lived, episodic eruptions, rather than steady winds, may be the dominant mass loss mechanism for the most massive ($> 25\,M_\odot$) stars. Determining the rate of these eruptions and the effects of the mass ejections are two of the crucial outstanding challenges facing stellar evolution theory. I have concentrated on leveraging the mid-infrared excess emission from warm circumstellar dust to identify post-eruptive massive stars and to characterize their evolutionary states.

The most spectacular example of post-eruptive circumstellar dust formation is seen around $\eta\,$Carinae, the most massive (100-150$\,M_\odot$) and most luminous ($\sim 3\times10^6\,L_\odot$) Galactic star to have had a recent eruption. After the Great Eruption between 1840 and 1860, $\eta\,$Car faded optically and, aside from a brief brightening in $\sim$ 1890, remained fainter until $\sim$ 1950 when it began to optically brighten. The $\sim 10 M_\odot$ of ejecta are now seen (Figure 1.1) as a dusty nebula around the star absorbing and then re-radiating $\sim$ 90% of the light in the mid-infrared (mid-IR). These dusty ejecta are a powerful and long-lived signature of eruption. The dust emission peaks in the mid-IR with a characteristic red color and a rising spectral energy distribution (SED) in the *Spitzer* mid-IR bands (see Figure 5.1). To date, no true analog (mass, luminosity, energetics, mass lost, time since explosion, spectral energy distribution etc.) of this exotic object has been found in any galaxy, but there have also been no systematic searches.

Eruptions appear to occur just before the ccSNe in certain cases. The Type Ib SN 2006jc was coincident with a bright optical transient that occurred in 2004 (Pastorello et al. 2007). SN 2009ip underwent a series of outbursts in 2009, 2010, and 2011 before probably exploding as a Type IIn SN in 2012 (Mauerhan et al. 2013; Prieto et al. 2013; Pastorello et al. 2012). The progenitor of the Type IIn SN 2010mc underwent an outburst 40 days prior to its explosion (Ofek et al. 2013). Moreover, some of the most luminous ccSNe are inferred to have originated from progenitors embedded in $\sim M_\odot$ of recently ejected material. They include SN 2006gy (Smith & McCray 2007) which showed clear signs of interaction of the SN ejecta with a massive circumstellar shell, SN 2007va (Kozłowski et al. 2010) that was completely enshrouded in its own dust, and SN 2010jl which was buried in $10\,M_\odot$ material ejected in the decades prior to explosion (Ofek et al. 2014b).

Our understanding of the role of episodic mass loss is surprisingly limited because these phases are difficult to model theoretically and simulate computationally. The $M_{initial} > 25\,M_\odot$ stars undergo periods of photospheric instabilities leading to stellar transients ($M_V \lesssim -13$) followed by rapid ($\dot{M} \gtrsim 10^{-4}\,M_\odot$/year) mass-loss and circumstellar dust obscuration in the last stages of their evolution. Deciphering the

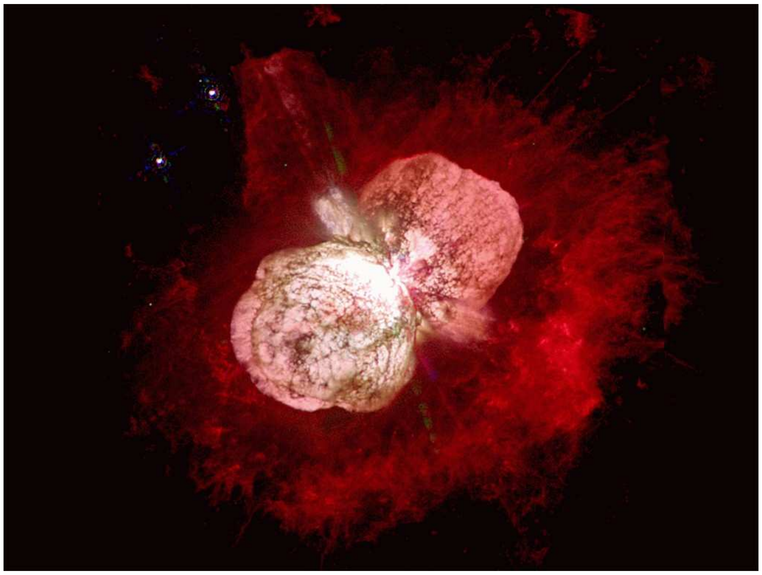

Fig. 1.1.— The dust obscured super-massive super-luminous Galactic star η Carinae, located 2.3 kpc away, as seen by *Hubble* (Morse et al. 1998). The hourglass shaped dusty shell has ten times the mass of the Sun and it is hundreds of times larger than the size of the solar system. 90% of the light from the star is first absorbed by the dust in the hourglass and then re-radiated in the mid-IR, which means that this optical HST image captures only 10% of the star's energy output.

effects of the mass ejections and the rate of these eruptions are challenging since the associated transients are significantly fainter than supernova explosions and are easily missed. I have demonstrated in Khan et al. (2010b, 2011, 2013, 2014) that it is possible to observationally address this issue using archival *Hubble*, *Spitzer*, and *Herschel* data.

What is completely new about this research program is that I identify these sources post-eruption both while they are optically luminous prior to circumstellar dust formation and after the obscuring dust forms in the ejecta using the mid-IR radiation from the warm dust. This allows me to address open questions such as whether these events happen to all massive stars or only to some of them, if it happens only once in a star's lifetime or multiple times, and if there is a causal connection between eruptions and the final ccSNe. The dust obscured massive stars I identify make up a potential progenitor catalog of future ccSNe, especially the Type IIn SNe where very few have had progenitors identified so far (SN 1961V, Kochanek 2011a; SN 2005gl, Gal-Yam & Leonard 2009; and SN 2009ip, Smith & Frew 2010).

Here, I include my work on this topic. Relevant work by others are referenced to throughout and listed at the end of this dissertation.

In Chapter 2, I focus on links in the causal mapping between massive stars and potentially fatal explosive transients, that opened with the 2008 discovery of the dust-obscured progenitors of the luminous outbursts in NGC 6946 and NGC 300. We carry out a systematic mid-IR photometric search for massive, luminous, self-obscured stars in four nearby galaxies: M33, NGC 300, M81, and NGC 6946. For detection, we use only the 3.6 μm and 4.5 μm IRAC bands, as these can still be used for multi-epoch *Spitzer* surveys of nearby galaxies ($\lesssim 10$ Mpc). We combine familiar

PSF and aperture-photometry with an innovative application of image subtraction to catalog the self-obscured massive stars in these galaxies. In particular, we verify that stars analogous to the progenitors of the NGC 6946 (SN 2008S) and NGC 300 transients are truly rare in all four galaxies: their number may be as low as ~ 1 per galaxy at any given moment. This result empirically supports the idea that the dust-enshrouded phase is a very short-lived phenomenon in the lives of many massive stars and that these objects constitute a natural extension of the AGB sequence. We also provide mid-IR catalogs of sources in NGC 300, M81, and NGC 6946.

In Chapter 3, we discuss the nature of the brightest mid-IR point source (which we dub Object X) in the nearby galaxy M33. Although multi-wavelength data on this object have existed in the literature for some time, it has not previously been recognized as the most luminous mid-IR object in M33 because it is entirely unremarkable in both optical and near-IR light. In the Local Group Galaxies Survey, Object X is a faint red source visible in VRI and Hα but not U or B. It was easily seen at JHK_s in the 2MASS survey. It is the brightest point source in all four *Spitzer* IRAC bands and is also visible in the MIPS 24 μm band. Its bolometric luminosity is $\sim 5 \times 10^5 L_\odot$. The source is optically variable on short time scales (tens of days) and is also slightly variable in the mid-IR, indicating that it is a star. Archival photographic plates (from 1949 and 1991) show no optical source, so the star has been obscured for at least half a century. Its properties are similar to those of the Galactic OH/IR star IRC+10420 which has a complex dusty circumstellar structure resulting from episodic low velocity mass ejections. We propose that Object X is a $M \gtrsim 30 M_\odot$ evolved star obscured in its own dust ejected during episodic mass loss events over at least ~half a century. It may emerge from its current ultra-short evolutionary phase as a hotter post-RSG star analogous to M33

Var A. The existence and rarity of such objects can be an important probe of a very brief yet eventful stellar evolutionary phase.

In Chapter 4, I search 7 galaxies for extragalactic analogs of η Carinae. The late-stage evolution of the most massive stars such as η Carinae is controlled by the effects of mass loss, which may be dominated by poorly understood eruptive mass ejections. Understanding this population is challenging because no true analogs of η Car have been clearly identified in the Milky Way or other galaxies. We utilize *Spitzer* IRAC images of 7 nearby ($\lesssim 4\,\mathrm{Mpc}$) galaxies to search for such analogs. We find 34 candidates with a flat or rising mid-IR spectral energy distributions towards longer mid-infrared wavelengths that emit $> 10^5\,\mathrm{L}_\odot$ in the IRAC bands (3.6 to $8.0\,\mu\mathrm{m}$) and are not known to be background sources. Based on our estimates for the expected number of background sources, we expect that follow-up observations will show that most of these candidates are not dust enshrouded massive stars, with an expectation of only 6 ± 6 surviving candidates. Since we would detect true analogs of η Car for roughly 200 years post-eruption, this implies that the rate of eruptions like η Car is less than the ccSN rate. It is possible, however, that every $\mathrm{M} > 40\,\mathrm{M}_\odot$ star undergoes such eruptions given our initial results.

In Chapter 5, we present the results of our examination of those candidates. We characterized and classified the candidates using multi-wavelength data from the optical through the far-IR. While a true analog of η Car remains to be found, we identify 18 extragalactic luminous, heavily obscured, evolved massive stars that have luminosities $\log(L/L_\odot) \simeq 5.5 - 6.0$ which suggests they may be similar to the Galactic stars IRC+10420, ρ Cas, and HR 8752. Our findings are consistent with every $\mathrm{M} \gtrsim 25\,\mathrm{M}_\odot$ star undergoing a prolonged (~centuries) self-obscuration phase following episodic enhanced mass loss. The median estimated mass causing the obscuration is $\sim 0.5 M_\odot$, and the total mass lost is of order 0.3-$1.9^{-1} M_\odot$. This implies that periods of optically thick mass loss cannot dominate the overall mass loss of these stars and the obscuration phases represent a negligible fraction of the post-main-sequence life times of the stars. In the long term, the sources that we identified will be prime candidates for detailed physical analysis with *JWST*.

Finally, in Chapter 6, I summarize the conclusions of this dissertation and reflect on the future prospects of this research.

Chapter 2: Census of Self-Obscured Massive Stars in Nearby Galaxies with *Spitzer*

Note: This chapter is based on the paper "Census of Self-Obscured Massive Stars in Nearby Galaxies with Spitzer: Implications for Understanding the Progenitors of SN 2008S-Like Transients", by R. Khan, K. Z. Stanek, J. L. Prieto, C. S. Kochanek, T. A. Thompson, and J. F. Beacom, published in the Astrophysical Journal, 715:1094-1108, in June 2010 (Khan et al. 2010a).

2.1. Introduction

The conventionally-understood fate of massive ($M > 8M_{\odot}$) stars is death by a core collapse that produces a neutron star or black hole, and an outgoing shock wave that successfully ejects the overlying stellar envelope to create a bright Type II or Ib/c supernova (SN). Given the detection of a SN-like optical event, the next challenge is to characterize the progenitor star in order to understand the last years of the life of a massive star. A more direct method for understanding the relation between massive stars and their transients is to simply catalog all the massive stars in the local universe ($D \lesssim 10\,\mathrm{Mpc}$) and then determine their individual fates. This is particularly important because we lack observational constraints on the number of failed SN that form a black hole without a SN-like optical transient (e.g., Kochanek et al. 2008; Smartt et al. 2009), and because the boundary between SN and other luminous transients of massive stars is uncertain (e.g., Chiosi & Maeder 1986; Woosley et al. 2002). While surveys for bright optical transients in the local universe are well-developed (e.g., Li et al. 2001), a complete census of massive stars in nearby galaxies are relatively recent (Massey et al. 2006) and efforts to study their fates have just started (Kochanek et al. 2008). Despite the technical challenges required by the depth, area, and cadence of the observations, these surveys are critical for our understanding of the correspondences between massive stars and their end states. The long-term promise of these surveys is to produce a catalog where the characteristics (luminosity, mass, binarity, winds, etc.) of the progenitors of future SN are listed.

A new link in this causal mapping between massive stars and their explosions opened with the discovery of the dust-obscured progenitors of the luminous outbursts in NGC 6946 (SN 2008S; Arbour & Boles 2008; Prieto et al. 2008) and NGC 300 (hereafter NGC 300-2008OT; Monard 2008; Bond et al. 2009; Botticella et al. 2009) in the mid-IR with *Spitzer*. In both cases, the progenitor was not detected in the optical, but as a ~ 400K mid-IR source with luminosity of $\sim 5 \times 10^4 L_\odot$ (Prieto et al. 2008; Prieto 2008) and a implied mass range of $\sim 6-15\ M_\odot$ (Prieto et al. 2008; Botticella et al. 2009; Berger et al. 2009; Gogarten et al. 2009). The dust temperature and the stringent upper limits on the optical fluxes (Prieto 2008; Botticella et al. 2009; Berger et al. 2009) demonstrated that both objects were enshrouded by a dusty wind. Whether progenitors of some massive star outburst or SN, the fact that these progenitors are completely self-obscured by dust implies that any complete census of the progenitors of luminous transients now requires mid-IR data as well.

In essence, we need a comprehensive survey for bright mid-IR sources in all nearby galaxies ($\lesssim 10\,\mathrm{Mpc}$) with (warm) *Spitzer*, analogous to the survey proposed by Kochanek et al. (2008) in the optical. For a first look, Thompson et al. (2009b) searched in M33 for deeply-embedded point sources that had similar properties to the progenitors of the transients in terms mid-IR colors, luminosities, and variability in archival *Spitzer* observations of M33, and detected only 18 sources with any similarity, and even fewer (one or two) as extreme in color and luminosity. They argued that transients such as SN 2008S and NGC 300-2008OT constitute a class of their own and are relatively common (of order $\sim 10\%$ of the SN rate), although the progenitors of this class are extremely rare among a galaxy's massive stars at a given time. Thus, Thompson et al. (2009b) argued that a significant fraction of all massive stars must undergo a dust-enshrouded phase within $\lesssim 10^4$ years prior to some kind of explosion.

Our understanding of the role of dust and variability in the final stages of the evolution of massive stars is surprisingly limited, despite it being a powerful probe of the physics of their last days. The goal of our project is to expand the Thompson et al. (2009b) survey to catalog the population of obscured massive stars and to identify the sub-population of massive stars from which these progenitors emerge. We use only the 3.6 μm and 4.5 μm IRAC bands, as they can be used in a future multi-epoch *Spitzer* survey of all nearby galaxies ($\lesssim 10$ Mpc) lacking the necessary archival data. We conduct our search in four galaxies: M33 ($D \simeq 0.96$ Mpc, Bonanos et al. 2006), NGC 300 ($D \simeq 1.9$ Mpc, Gieren et al. 2005), M81 ($D \simeq 3.6$ Mpc, Saha et al. 2006), and NGC 6946 ($D \simeq 5.6$ Mpc, Sahu et al. 2006), so that we can compare our results with Thompson et al. (2009b) and test our search method in relatively distant and crowded galaxies, where a novel application of image subtraction helps us overcome the poor spatial resolution of *Spitzer* compared to the stellar crowding. We will also examine these populations in the LMC and SMC using the published catalogs of Blum et al. (2006) and Bolatto et al. (2007), respectively. These galaxies span a broad range in distance, luminosity, star formation rate (SFR) and metallicity.

This chapter is organized as follows. Section 2.2 describes our methodology for identifying obscured massive stars in nearby galaxies in detail. Section 2.3 discusses the nature of this stellar population using the color-magnitude diagrams (CMDs) for the galaxies and spectral energy distributions (SEDs) for the individual obscured stars. Section 2.4 considers the implications of the findings for our understanding of the nature of progenitors of SN 2008S-like transients and the arguments for conducting a multi-epoch survey of all nearby galaxies ($\lesssim 10\,\mathrm{Mpc}$) with (warm) *Spitzer*. Also, we provide lists of the obscured massive stars that we identified in the four galaxies, and the mid-IR catalogs of sources in NGC 300, M81, and NGC 6946. The mid-IR catalog of sources in M33 was published in Thompson et al. (2009b) (also see McQuinn et al. (2007)).

2.2. Search for Obscured Massive Stars

In this section, we describe the methodology of our search for self-obscured massive stars in archival *Spitzer* IRAC (Fazio et al. 2004) data. Our goal is to carry out this inventory and demonstrate how it can be done despite the crowding problems created by the limited spatial resolution of *Spitzer* at greater distances. For M33, we used the six co-added epochs of data from McQuinn et al. (2007) that were used by Thompson et al. (2009b). For NGC 300, we used the data collected by the Local Volume Legacy (LVL) Survey (Dale et al. 2009). For NGC 6946 and M81 we used the data collected by the SINGS Legacy Survey (Kennicutt et al. 2003). Our images of the galaxies are selected regions of the full mosaics available for each galaxy. The M33 image covers an area of $\approx 33' \times 33'$ (1600×1600 pixels, with $1''.2$/pixel), the NGC 300 image covers an area of $\approx 15' \times 15'$ (1250×1250 pixels with $0''.75$/pixel), the M81 image covers an area of $\approx 18' \times 18'$ (1450×1450 pixels with $0''.75$/pixel), and the NGC 6946 image covers an area of $\approx 12' \times 12'$ (1000×1000 pixels with $0\overset{''}{.}75$/pixel). Figures $1-4$ show the 4.5 μm images of the four galaxies.

We searched for obscured stars in three stages and order the identified objects by the stage at which we can fully measure the source properties. We use the same criteria of $[3.6]-[4.5] > 1.5$ magnitude and $M_{4.5} < -10$ magnitude used by Thompson et al. (2009b) to select extremely red and bright objects (Extreme Asymptotic Giant Branch or EAGB objects) similar to the SN 2008S and NGC 300-2008OT progenitors. First, we searched for objects directly identifiable in both the 3.6 μm and 4.5 μm images. Second, we searched for objects detectable at 4.5 μm but not at 3.6 μm. Finally, in a novel application of difference imaging methods, we searched for obscured stars not directly detectable in either the 3.6 μm or 4.5 μm IRAC bands. For nearer galaxies, we expect most red sources to be detectable in either or both of the IRAC bands. But for the more distant galaxies, the difference imaging method helps us identify confused sources in crowded images.

All normal stars have the same mid-IR color (Vega $[3.6]-[4.5] \simeq 0$), because of the Rayleigh-Jeans tails of their spectra. Stars with dusty envelopes lie off the main stellar locus at color 0 towards redder colors. This means that if we use difference imaging methods to match the 3.6 μm image to the flux scale and point spread function (PSF) structure of the 4.5 μm image and then subtract, all the normal stars “vanish” to leave us only with the stars having significant dust emission. In practice, we use the ISIS image subtraction software package (Alard & Lupton 1998) following the procedures from Hartman et al. (2004). We use the 4.5 μm image as the reference from which the 3.6 μm image is subtracted. ISIS automatically sets the flux scaling and backgrounds to optimally subtract the two bands, and utilizes a spatially variable kernel. Figures $1-4$ show the results of this procedure for our target galaxies. The result is visibly stunning: almost all the stars “vanish” to leave us with a clean image of the red self-obscured stars. Now we can identify and accurately measure positions for red sources that could otherwise be confused due to crowding.

We define objects directly identifiable in both the 3.6 μm and 4.5 μm bands as Class–A objects. This stage should be most successful for the nearest galaxies, and for sources with significant 3.6 μm flux. The procedure followed at this stage is similar to that followed by Thompson et al. (2009b), except that we verify the color limits for the candidates. Also, for all objects that are not red enough based on DAOPHOT PSF-fitting methods, we re-estimate the magnitudes and colors through aperture-photometry to ensure that we do not miss any candidate objects due to small measurement variations. Figure 2.5 shows a Class–A object detected in NGC 300.

We define objects detectable at 4.5 μm but not at 3.6 μm as Class–B objects. For point sources that had a 3σ detection in the 4.5 μm image based on PSF-photometry but lacked a 3.6 μm counterpart within a 0.5 pixel matching radius, we used aperture-photometry at the position of the 4.5 μm source to estimate or set limits on the 3.6 μm magnitude and color ($[3.6]-[4.5]$). Figure 2.6 shows a Class–B object detected in M33.

We define objects detectable only in the wavelength differenced image (hereafter "[3.6]-[4.5] image") as Class–C objects. We used DAOPHOT PSF-fitting to identify sources on the [3.6]-[4.5] image. For the detected objects lacking a counterpart in the 4.5 μm catalog within a 1 pixel matching radius, we use aperture-photometry on both the 3.6 μm and 4.5 μm images at the source position in the differenced image to estimate magnitudes and colors. Figure 2.7 shows a Class–C object detected in M81. For comparison, we show the SN 2008S and NGC 300-2008OT in Figures 2.8

and 2.9. These are detected as Class–B and Class–A objects, respectively, in our blind searches of NGC 6946 and NGC 300, as described in Section 2.3.

Given this broad outline, we now describe the specific technical details of how we performed the photometric measurements at the various stages of the search and then verified the properties of the candidates.

We used the DAOPHOT/ALLSTAR PSF-fitting and photometry package (Stetson 1992) to identify point sources in both the 3.6 μm and 4.5 μm IRAC images. The point source catalogs (Tables 5, 7, and 9) are comprised of those sources detected at $> 3\sigma$ at 4.5 μm and with a 3.6 μm counterpart within 0.5 pixels. We measure the properties of the sources using either DAOPHOT/ALLSTAR to do PSF-photometry or APPHOT/PHOT to do simple aperture-photometry. The PSF-magnitudes obtained with ALLSTAR were transformed to Vega-calibrated magnitudes using aperture corrections derived from bright stars. For aperture-photometry magnitudes, the aperture correction is determined from the *Spitzer* point response function reference image obtained from the IRAC website[1], and we empirically verified that for bright stars the magnitudes determined through PSF and aperture-photometry agree within ±0.05 magnitude. When performing aperture-photometry, we estimate the local background for each object using APPHOT/PHOT employing a 2σ outlier rejection procedure in order to exclude sources located in the local sky annulus, and correct for the excluded pixels assuming a Gaussian background distribution.

For every candidate object, we implement a strict detection criteria. We require a $> 3\sigma$ detection at 4.5 μm regardless of the search stage at which an object is detected and how its properties are determined (PSF or aperture-photometry).

---

[1] http://ssc.spitzer.caltech.edu/irac/psf.html

Initially, we determine the 2σ limit on $m_{3.6}$ using the local background estimated using APPHOT/PHOT. If the estimate of $m_{3.6}$ is brighter than the 2σ local background limit, then we treat the $m_{3.6}$ estimate as the measured flux, otherwise we use the 2σ background estimate as an upper limit on the flux. Thus, we get a 2σ lower limit on the $[3.6] - [4.5]$ color of the objects for which we do not have reliable measurements at 3.6 μm. This color limit verification is done identically in every stage of the search. Stars for which only limits could be determined are included in the tables and CMDs, but we do not show their SEDs. We visually inspected all candidate red stars in the 3.6 μm, 4.5 μm, and wavelength differenced images and rejected candidates that do not appear likely to be a star. The differenced images are very useful because they cleanly remove most of the crowding, as is apparent in Figures $5 - 9$.

Due to how we organized the search, we first identify candidates that can be detected it at least one of the 3.6 μm and 4.5 μm images before searching for additional objects in the differenced image. Most of the Class–A and the Class–B objects are detected independently in the [3.6]-[4.5] image as well, and the Class–C objects represent only the additional sources that can be hidden by crowding, especially in the more distant galaxies. The progenitor of SN 2008S is an excellent example: although we identified it in NGC 6946 as a Class–B object, Figure 2.8 makes it clear that had we missed it at 4.5 μm, it would be detected without any confusion as a Class–C object. There was a tendency for DAOPHOT to split objects detected in the [3.6]-[4.5] images, presumably due to the non-standard statistical properties of these images. Generally there was a primary, true detection and a secondary detection offset by roughly a pixel. These off-center detections represented the major source of false-positives for the Class C objects, and we systematically rejected these duplicate detections.

2.3. Inventory of Obscured Massive Stars

Figures 10 – 13 present the $m_{4.5}$ versus [3.6] – [4.5] CMDs for each galaxy. For comparison, we include the progenitors of NGC 300-2008OT and SN 2008S (Prieto et al. 2008; Prieto 2008) as well as the $[3.6] - [4.5] > 1.5$ and $M_{4.5} < -10$ selection region for extremely red and bright objects. The candidates that meet this criteria are shown with symbols indicating the stage of the search at which they were identified. Where applicable, color limits are indicated by arrows. Figures 10 – 13 also present the mid-IR SEDs of the candidate objects as compared to the SEDs of the SN 2008S and NGC 300 transient progenitors. Here we include the 5.8 μm and 8.0 μm fluxes as determined using aperture-photometry for the position of the 4.5 μm source. Due to significant PAH emissions in these two bands, we view the aperture-photometry measurements in these bands as less reliable. The SEDs of some fainter sources show a sharp decline at 5.8 μm before rising again at 8.0 μm due to PAH dominated background contamination. Figure 2.14 shows a summary of the CMDs of these four galaxies as well as those for the LMC and SMC from Blum et al. (2006) and Bolatto et al. (2007), respectively. Figure 2.15 shows the spatial distribution of the sources. All the objects identified at both 3.6 μm and 4.5 μm with DAOPHOT are reported in Tables 2.6, 2.8, and 2.10 for NGC 300, M81, and NGC 6946 respectively. Since Thompson et al. (2009b) published a source catalog for M33, we do not publish a new catalog for this galaxy. In this section, we discuss the results of our search for obscured massive stars in each of the targeted galaxies. Lists of the candidates are presented in Tables 2.5, 2.7, 2.9, and 2.11, sorted by the stage at which we measured the source properties (Class–A objects first, followed by Class–B objects and then Class–C objects), for all four galaxies.

2.3.1. M33

We first discuss our analysis of M33 ($D \simeq 0.96\,\mathrm{Mpc}$, Bonanos et al. 2006), the nearest of the targeted galaxies, using our improved methods. Initially, we identify 15 Class–A objects based on PSF-photometry exactly following the procedures of Thompson et al. (2009b) except where we estimate the color limits. We identify 4 additional Class–A objects through aperture-photometry, as well as 3 Class–B objects and 1 Class–C object. On visual inspection, we reject 1 object in each class, leaving 20 candidates. These objects include 12 of the 18 stars identified by Thompson et al. (2009b) as self-obscured EAGBs. For one of these objects (Class–B), we could only determine a 2σ color limit. The only Class–C object was rejected as a duplicate detection of one of the Class–A objects. Table 2.5 presents the candidate EAGB sources. See Table 1 in Thompson et al. (2009b) for the mid-IR point source catalog.

Of the 6 stars in Thompson et al. (2009b) that were not identified in our present census as candidates, 5 are actually found in our search (3 in the first stage, 1 in the second stage, 1 in the third stage), but they are all located close to the color and magnitude selection boundaries, and small shifts in the color and magnitude estimates excluded them from the sample. The only object among the 18 that we missed entirely lay outside the search region in M33, which is slightly different from that of Thompson et al. (2009b). Only 1 source, the same in both searches, is brighter than the NGC 300 transient progenitor and redder than the SN 2008S progenitor color limit.

2.3.2. NGC 300

As the host of one of the optical transients, NGC 300-2008OT ($D \simeq 1.9$ Mpc, Gieren et al. 2005) is of particular interest. Initially, we identify 8 Class–A objects based on PSF-photometry only (including the NGC 300-2008OT progenitor, as shown in Figure 2.8), 1 additional Class–A object through aperture-photometry, 2 Class–B objects, and 4 Class–C objects. However, all 4 Class–C objects were rejected as duplicate detections of Class–A/B objects. Overall, we found 10 candidate objects in NGC 300 apart from the transient progenitor. The color determined for each of these 10 objects is above the 2σ local background limit and none of them is brighter than the NGC 300-2008OT progenitor and redder than the SN 2008S progenitor color limit. Table 2.6 provides a catalog of the 11,241 sources identified in both bands, and Table 2.7 lists the candidate EAGB sources.

We estimate the NGC 300-2008OT progenitor properties to be $M_{3.6} = -7.36$, $M_{4.5} = -10.25$, and $[3.6] - [4.5] = 2.89$ which agrees with the previous measurement of $M_{3.6} = -7.63$, $M_{4.5} = -10.39$, and $[3.6] - [4.5] = 2.72$ (Prieto 2008).

2.3.3. M81

As a large, nearby, nearly face-on spiral galaxy at an intermediate distance (more distant than NGC 300 and closer than NGC 6946), M81 ($D \simeq 3.6$ Mpc, Saha et al. 2006) was chosen as a test case for our improved search method. Initially, we identify 15 Class–A objects through PSF-photometry only, 9 additional Class–A objects through aperture-photometry, 15 Class–B objects, and 3 Class–C objects. However, on visual inspection, we rejected 2 Class–A objects and 1 Class–C object, leaving 39 candidates, of which only 1 object is brighter than the NGC 300-2008OT progenitor and redder than the SN 2008S progenitor color limit. For 9 of these objects we could only determine a 2σ color limit (4 Class–A, 4 Class–B, 1 Class–C). Table 2.8 provides a catalog of the 6,021 sources identified in both bands, and Table 2.9 lists the candidate EAGB sources.

2.3.4. NGC 6946

The host of the SN 2008S event, NGC 6946 ($D \simeq 5.6$ Mpc, Sahu et al. 2006) is the most distant of the four galaxies. At this distance, the $M = -10$ absolute magnitude limit is close to the 3σ detection limit at 4.5 μm, leading to reduced completeness. The 4.5 μm SINGS archival image of NGC 6946 contains many artifacts that significantly affect the subtracted image. For example, bright stars show bright "halos" in the 4.5 μm image that appear as rings in the subtracted image. As a result, most of the candidates identified in the second and third stages did not pass the visual inspection because they were clearly associated with artifacts.

Initially, we identify 5 Class–A objects through PSF-photometry only, 5 additional Class–A objects through aperture-photometry, 38 Class–B objects (including the SN 2008S progenitor), and 32 Class–C objects. On visual inspection, we rejected 2 Class–A objects, 21 Class–B objects, and 26 Class–C objects, leaving 30 candidates apart from the SN 2008S progenitor. None of these new sources are redder than this progenitor's color limit and brighter than the NGC 300 transient progenitor. For 13 of these objects we could only determine a 2σ color limit (1 Class–A, 11 Class–B, 1 Class–C). Table 2.10 provides a catalog of the 5,601 sources identified in both bands, and Table 2.11 lists the candidate EAGB sources.

One of the rejected candidates is a slightly shifted duplicate detection of the SN 2008S event progenitor star. We were unable to determine if there might be multiple stellar objects blended together at the image location. This can be further probed in future mid-IR observations of this galaxy using (warm) *Spitzer*. We estimate the SN 2008S progenitor properties to be $M_{3.6} > -9.09$, $M_{4.5} = -11.28$, and $[3.6]-[4.5] > 2.19$ which agrees with the previous measurement of $M_{3.6} > -9.46$, $M_{4.5} = -11.47$, and $[3.6]-[4.5] > 2.01$ (Prieto et al. 2008).

The spatial distribution of AGB and EAGB stars in NGC 6946 is very different from that of the other three galaxies (see Figure 2.15). The absence of these stars near the center of NGC 6946 is real, unlike M81 where we mask the saturated galactic center. The EAGB candidates also lie on the periphery of the galaxy near the R_{25} isophotal radius. Brighter and redder EAGBs are relatively easier to identify through our improved search method even if they were initially missed due to blending, and it is highly unlikely that a significant number of EAGB objects in the inner region of NGC 6946 were missed. This suggests that the spatial pattern of the star formation history of NGC 6946 is quite different from the other three galaxies.

2.4. Discussion

The two supernova-like transient events observed in NGC 300 and NGC 6946 were fairly luminous, and the mid-IR properties of the progenitors of both transients indicate the presence of a dusty, warm, optically thick wind around the progenitors (Prieto et al. 2008; Thompson et al. 2009b; Botticella et al. 2009; Prieto et al. 2009; Wesson et al. 2009). The extremely red $[3.6]-[4.5]$ colors of the progenitors can only be explained by total self-obscuration resulting from a period of circumstellar dust production. Our search for analogs of these progenitors gives us the opportunity to empirically investigate the nature and origin of such objects. In this section, we discuss the implications of our findings. For this discussion, we include the statistics for the LMC and SMC using the catalogs from the full survey of the LMC by Blum et al. (2006) and the partial survey of the SMC by Bolatto et al. (2007). Table 2.4 lists the candidate EAGB sources in the LMC and SMC.

First, we attempt to characterize the detected EAGB population of the target galaxies. Next, we consider how our results may help improve our understanding of the late-stage evolution of massive stars. Finally, we motivate a multi-epoch mid-IR survey of nearby galaxies to produce a complete list of potential progenitors of future supernova like transient events.

2.4.1. The EAGB Population

Although the exact number of analogs of the SN 2008S and NGC 300-2008OT progenitors (N_{EAGB}) in these four galaxies is uncertain due to the absence of absolute quantitative criteria to identify such objects, it is clear that objects as bright and red as these progenitors are extremely rare. Following a conservative selection criteria of requiring the objects to be very red ($[3.6]-[4.5]>1.5$) and bright ($M_{4.5}<-10$) produces a sample size on the order of tens of candidates per galaxy. However, following the strictest criteria of requiring the candidates to be brighter than the NGC 300-2008OT progenitor and redder than the SN 2008S event progenitor color limit, we would select no more than 1 candidate object in LMC, M33 and M81, none is SMC, and none other than the 2008 transient progenitors in NGC 300 and NGC 6946. Taking measurement uncertainties into account can increase the number of objects per galaxy meeting the strictest criteria by at most 1 more in LMC, M33, and NGC 300, 0 more in SMC and M81, and 3 more in NGC 6946.

Simple black-body fits of the EAGB SEDs with an assumed dust emissivity function going as λ^{-1} show that almost all these objects have a bolometric luminosity of $\sim 10^4 L_\odot$ and photospheric temperatures of $\sim 300-600\ K$. This indicates that these are very massive stars embedded in dusty winds, with luminosities and temperatures very similar to those of the 2008 supernova-like transient progenitors.

To examine the contamination of the EAGB region of the CMD by non-EAGB objects, we took a closer look at the LMC objects which satisfy the $[3.6]-[4.5] > 1.5$ and $M_{4.5} < -10$ criteria. The reddest object at $[3.6]-[4.5] \sim 2.5$ is the IRAS source, IRAS 05346-6949 (Elias et al. 1986), which has been classified as an "Extremely Red Object" (ERO) in Gruendl & Chu (2009). It is believed to be an enshrouded supergiant which is not bright in the optical. There are IRS spectra for 13 objects in this (ERO) class, although they are all less luminous ($L \lesssim 10^4 L_\odot$) than the 2008 transient progenitors, and 7 of them are carbon stars (Gruendl et al. 2008). If such contamination is common, then analogs of SN 2008S and NGC 300-2008OT transient progenitors may be even rarer than our conservative estimates.

To determine the fraction of massive stars in these galaxies that are analogous to the SN 2008S and NGC 300 transient progenitors, we first estimate the total number of massive stars in each galaxy by scaling the Thompson et al. (2009b) estimate of the number of RSG stars (N_{RSG}) in M33. We scale the number using the B-band luminosity estimates from Karachentsev et al. (2004), and find that the fraction is always on the order of $N_{EAGB}/N_{RSG} \sim 10^{-4}$. The constancy of this ratio means that our efficiency at finding them is nearly constant over a wide distance range, and that very few of the massive stars in any one galaxy at any moment have mid-IR colors and brightnesses comparable to those of the SN 2008S and NGC 300-2008OT progenitors. Table 2.1 shows the estimated EAGB counts as a fraction of massive stars in the six galaxies that we studied. The lower fractions in M81 and NGC 6946 are likely real rather than a completeness problem. For the SMC we only have a lower bound on N_{EAGB}, N_{EAGB}/N_{RSG}, and the ratio relative to M33 because the S^3MC survey of the SMC covered only part of the galaxy.

Thompson et al. (2009b) proposed that the very red and bright candidates are the most massive AGB stars in a late stage of evolution and thus constitute a natural extension of the AGB branch. Under this assumption, the ratio of the number of EAGB and massive AGB stars in a galaxy at a given time should depend on the star formation history of the galaxy, since the lifetime of $\sim 2-8M_{\odot}$ stars spans $\sim$ 100Myr–1Gyr. Based on the structure of the M33 CMD and the detection limits for the more distant galaxies, we used the criteria of

$$-9.3 < M_{4.5} + 3([3.6] - [4.5]) < -7.3 \tag{2.1}$$

and

$$-10.2 < M_{4.5} - 0.55([3.6] - [4.5]) < -11.6 \tag{2.2}$$

to select the bulk of the AGB sequence while minimizing the effects of incompleteness for the more distant galaxies. We also required that the objects lie within the R_{25} isophotal radius of the galaxies (see Figure 2.15).

Figure 2.14 shows the CMDs zoomed in to highlight the AGB and EAGB stars, and Figure 2.15 shows the sky distribution of the luminous red AGB and EAGB candidate objects. The small number of bright objects in the SMC CMD is largely due to the S^3MC survey (Bolatto et al. 2007) covering only portions of the SMC. While we can clearly see the AGB sequence in M33 and NGC 300, contamination by extragalactic sources is a problem for M81 and NGC 6946. We correct for this contamination using the 10 square degree Spitzer Deep Wide Field Survey (SDWFS, Ashby et al. 2009). While there is no significant extragalactic contamination to the EAGB sources, Table 2.2 shows that the contamination correction to the AGB sample is important. We ignore the possibility of foreground contamination of the

AGB region given the rarity of luminous AGB stars in our galaxy and our small fields of view.

The ratios of the numbers of EAGB to luminous red AGB stars, in the LMC, SMC, and the four galaxies that we studied, are $N_{EAGB}/N_{AGB} = 0.01$, 0.015, 0.02, 0.04, 0.05, and 0.14, respectively. There is worrisome trend in the ratios with increasing distance. It may be partly due to decreasing completeness of the AGB population relative to that for the EAGB population with increasing distance. The AGB candidates are selected from the catalog of mid-IR sources that are detected in both 3.6 μm and 4.5 μm, and for galaxies at greater distances we are losing AGB stars at the bottom of our selection box and potentially overestimating the extragalactic contamination. This can lead us to over-subtract the contamination and underestimate N_{AGB}. On the other hand, the EAGB candidates are detected using our improved methods, and thus include objects detected only at 4.5 μm or in the $[3.6] - [4.5]$ differenced image as well as those detected in both IRAC bands. This allows us to detect EAGB candidates that would otherwise be missed due to crowding and thus makes our EAGB count relatively more complete at greater distances when compared to the completeness of the AGB star count.

Table 2.2 summarizes the EAGB counts as fraction of AGB stars. If all these galaxies had the same relative star formation history, the N_{EAGB}/N_{AGB} ratio should be identical for all galaxies given fixed completeness. Alternatively, the various steps we used for finding the EAGB stars are improving our completeness for EAGB stars at the distance of NGC 6946 by a factor of ~ 7. This may well be the case, since if we only used the DAOPHOT catalog of this galaxy, we would find only 4 EAGB candidates instead of 30. Thus, for NGC 6946 and to a lesser extent M81, our completeness for AGB stars is limited by the shallow depth of the SINGS observations.

Next we investigate whether the numbers of EAGB candidates correlate with the current SFR of these galaxies. We use the $L(H\alpha)$ estimates from Kennicutt et al. (2008) and estimate the SFR using the results from Lee et al. (2009). There may be a weak correlation between N_{EAGB} and SFR (Hα), although the correlation clearly does not hold for NGC 6946. The discrepancy in this case is severe, and corresponds to finding only $\sim 20\%$ of the EAGB stars if viewed as a completeness problem. It seems more likely that the correlation is coincidental.

The EAGB candidate objects are expected to be very faint in the optical even if an optical counterpart exists. As such, we need very deep optical catalogs to search for optical counterparts. Of the four galaxies that we studied, only M33 has a publicly available deep optical catalog. Thompson et al. (2009b) reported that no optical counterparts of the M33 EAGB candidate sources was found. For the three other galaxies, there is no publicly available sufficiently deep optical catalog that can be utilized in a similar manner.

2.4.2. Understanding the Evolution of Massive Stars

As discussed in Thompson et al. (2009b), there are three classes of explanations for the two transient events detected in 2008: explosive white dwarf formation, low-luminosity supernova (normal Fe core or electron capture SN), or a massive star transient. Prieto et al. (2008) and Thompson et al. (2009b) argue for the electron capture SN interpretation, and this is supported by Botticella et al. (2009). Pumo et al. (2009) argue for this scenario using a parametric approach, demonstrating that such supernovae can be explained in terms of electron capture SN from super-AGB progenitors. Prieto et al. (2009) also found that the mid-IR spectra of the outburst resembled that of a proto-planetary nebula rather than a massive star outburst. Kashi et al. (2010) suggest that a mass transfer episode from an extreme asymptotic giant branch star to a main sequence companion powered NGC 3002008-OT. Smith et al. (2009b) and Bond et al. (2009) argue for a massive star outburst because of the optical spectra of the transients, but Prieto et al. (2008) note that such optical spectral characteristics are also found in proto-planetary nebula. Smith et al. (2009a) suggest that the two transient events are possibly linked to LBV eruptions, and are similar to SN 2009ip and the 2009 optical transient in UGC 2773. However, both of these events discovered in 2009 have optically luminous progenitors, unlike the progenitors of SN 2008S and NGC 300-2008OT. Bonanos et al. (2009) suggested that objects similar to the two 2008 transient progenitors are related to supergiant Be stars. However, whether a link between LBVs and sgBe stars exists is not known at this point.

While the nature of the two 2008 transient progenitors remains debated, our search for analogs of such objects has now empirically shown that such extremely red and luminous objects are truly rare. We estimate this number to be on the order of few tens per large galaxy, but it can be as low as ~ 1 if selected by the strictest criteria of requiring the objects to be brighter than the NGC 300 transient progenitor and redder than the SN 2008S progenitor. Thompson et al. (2009b) estimated the duration of the dust obscured phase of EAGB stars to be on the order of $\sim 10^4$ years, a time scale very similar to that of the onset of carbon burning in relatively low mass massive stars.

Late stage evolution of stars in this mass range, around $\sim 6 - 8 M_\odot$, is very difficult to model (e.g., Miyaji et al. 1980; Siess 2007; Poelarends et al. 2008). Pumo et al. (2009) argue that for very rapid mass loss rates, a completely self-obscuring shell can even be produced on the order of ~ 150 years prior to an electron capture SN explosion. Such an ultra-short duration for the dust obscured phase would make it surprising to find any true analogs of the SN 2008S or NGC 3002008OT progenitors in our small sample of galaxies.

We cannot definitively claim that any of our EAGB candidates are truly analogous to the two 2008 transient progenitors. However, we have empirically shown that even using relatively shallow archival data for relatively distant galaxies, we can successfully identify the dusty self-obscured stellar population. Using a combination of conventional PSF and aperture-photometry methods along with innovative use of difference imaging methods, we can overcome crowding issues for galaxies at greater distances as well. If another SN 2008S like transient is to occur in these galaxies, it is likely to be one of the sources we identified here. While the ordering of our search from very conventional (Class–A) to unconventional (Class–C) appears to suggest that the wavelength-differenced approach is of limited use, it is in fact very valuable for confirming candidates and becomes increasingly effective at greater distances. It is important when using it to note the manner in which the resulting changes in image statistics somewhat confuse standard source identification codes.

This study is also a significant expansion of the sample of galaxies with detailed mid-IR stellar catalogs. Previously, full catalogs existed only for the LMC (Blum et al. 2006) and M33 (McQuinn et al. 2007; Thompson et al. 2009b), with partial catalogs for the SMC (Bolatto et al. 2007) and M31 (Mould et al. 2008). Our new catalogs can be used to study various stellar populations in nearby galaxies over a wide range of distances. We have also demonstrated that an innovative application of difference imaging can be used to remove crowding confusion for distant galaxies when searching for objects with significant color excesses. The improved data analysis method used in this study can be applied to study other stellar populations as well.

2.4.3. Motivations for Future Observations

Significant uncertainties regarding the nature of these transient events and their progenitors remain. A simple step is to determine whether the SN 2008S or NGC 300-2008OT progenitors survived their transients. The transient light curves have now likely faded, based on the Botticella et al. (2009) and Bond et al. (2009) light-curves, to the point where the continued existence of a progenitor can be observed, although this will likely require *Spitzer* observations to constrain a return to a self-obscured phase if optical and near-IR searches fail. Another important step is to properly survey the AGB/EAGB populations of all nearby ($D < 10$ Mpc) galaxies. Such a survey would have two goals. First, it would detect and characterize the progenitors of any future, similar events, and generally constrain the fraction of supernovae and massive star transients associated with self-obscured phases of stellar evolution more systematically. Kochanek et al. (2008) and Smartt et al. (2009) point out that there is a deficit of massive SN progenitors. One solution would be to obscure the progenitors and such *Spitzer* searches will greatly help to constrain this possibility, albeit only for self-obscured sources as compared to stars behind dense foreground dust. Second, it would characterize these phases of stellar evolution more generally, particularly since treatments of the AGB phase are an increasingly important problem in models of galaxy evolution (e.g., Marcillac et al. 2006; Santini et al. 2009; Conroy et al. 2010a). Given catalogs of the AGB stars in galaxies with a broad range of physical properties, the scaling of AGB stars and their mid-IR emission due to dust absorption could be empirically calibrated as a function of galaxy star formation rates and metallicity.

For the more distant galaxies, M81 and NGC 6946, we relied on the SINGS observations, which were not designed to characterize individual stars. As a result, they are shallower than desired for this purpose. For example, the observational depth makes it difficult to count the AGB stars in these galaxies reliably and to properly control for contamination by extragalactic sources. We emphasize that source confusion for fully self-obscured stars is not a primary limitation and can be overcome even in the more distant galaxies using our new analysis methods based on difference imaging between the 3.6 μm and 4.5 μm wavelengths.

A particularly attractive approach to obtaining such deeper catalogs is to carry out the observations as part of a sparse variability survey. Little is known about mid-IR variability of such rare, massive stars, and the variability provides another means of identifying AGB stars in the presence of confusion, again through the use of difference imaging. In Thompson et al. (2009b), for example, we found that variability increased along the AGB sequence except for the small population of EAGB stars, but the statistics were so limited that it was hard to draw general conclusions.

2.5. Conclusions

We carried out a systematic mid-IR photometric search for massive, luminous, self-obscured stars in four nearby galaxies combined with existing data for the LMC and SMC. We use a combination of conventional PSF and aperture-photometry techniques along with an innovative application of image subtraction. We investigate the population of SN 2008S-like transient event progenitor analogs in these 6 galaxies. We report catalogs of mid-IR sources in three new galaxies (NGC 300, M81, and NGC 6946) and candidate extreme AGB stars in all 6.

Using our methods, bright and red extreme AGB stars can be inventoried to $D \lesssim 10$ Mpc despite *Spitzer*'s relatively poor angular resolution. The biggest current problem is that the archival data is insufficiently deep: even with our innovative “band-subtraction” technique, we simply need more photons to detect these extremely red stars in the more distant galaxies. A future multi-epoch survey using (warm) *Spitzer* could identify all EAGB candidates in nearby galaxies, characterize their variability, and pin down the contribution of these partly obscured stars to galaxy SEDs as a function of wavelength.

Finally, we again emphasize the point made by Thompson et al. (2009b). Stars analogous to the progenitors of the SN 2008S and the NGC 300 transients are truly rare in all galaxies. At any moment there appears to be only ~ 1 true analog, and up to ~ 10 given a more liberal selection criterion, per galaxy. While completeness problems due to the limited depth of the archival data make it impossible to give exact scalings, they represent roughly 2×10^{-4} of the red super giant population, $\sim 10^{-2}$ of the AGB population, and appear at a rate of order 50 EAGB stars per unit star formation ($M_\odot$ year^{-1}) using the liberal criteria (and an order of magnitude fewer if we use the more conservative one). Clarifying these scalings with stellar mass, SFR and metallicity requires larger and deeper surveys of nearby galaxies than can be accomplished with warm *Spitzer* or eventually with JWST.

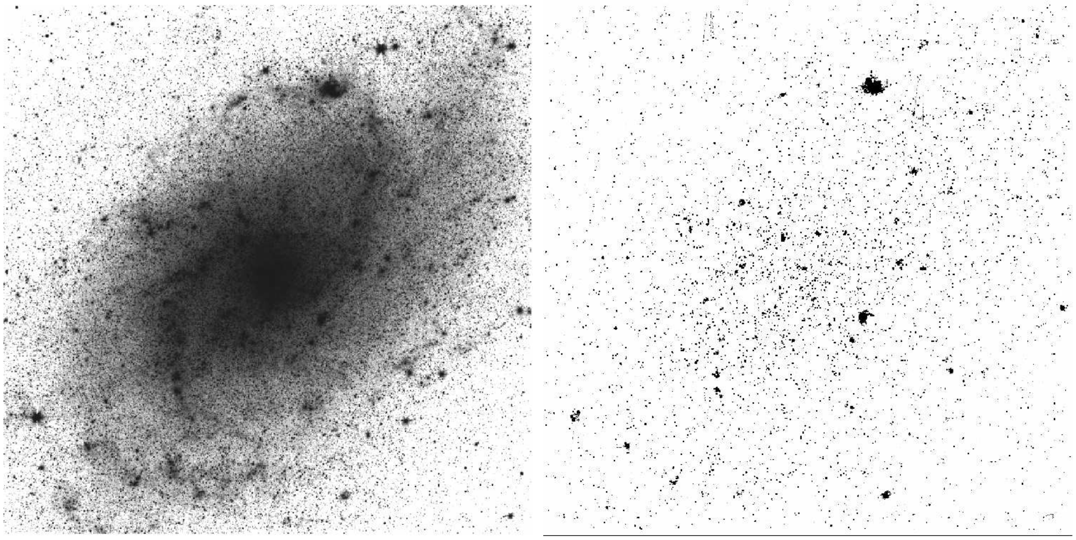

Fig. 2.1.— M33 4.5 μm IRAC image (*left*) and $[3.6] - [4.5]$ image (*right*). The image covers an area of $\approx 33' \times 33'$ (1600×1600 pixels, with $1\overset{''}{.}2$/pixel). This difference image is constructed by using image subtraction to scale and subtract the 3.6 μm image from the 4.5 μm image including the necessary corrections for the PSF differences. All the normal (non-red) stars "vanish" in the [3.6]-[4.5] image leaving the stars with significant dust emission.

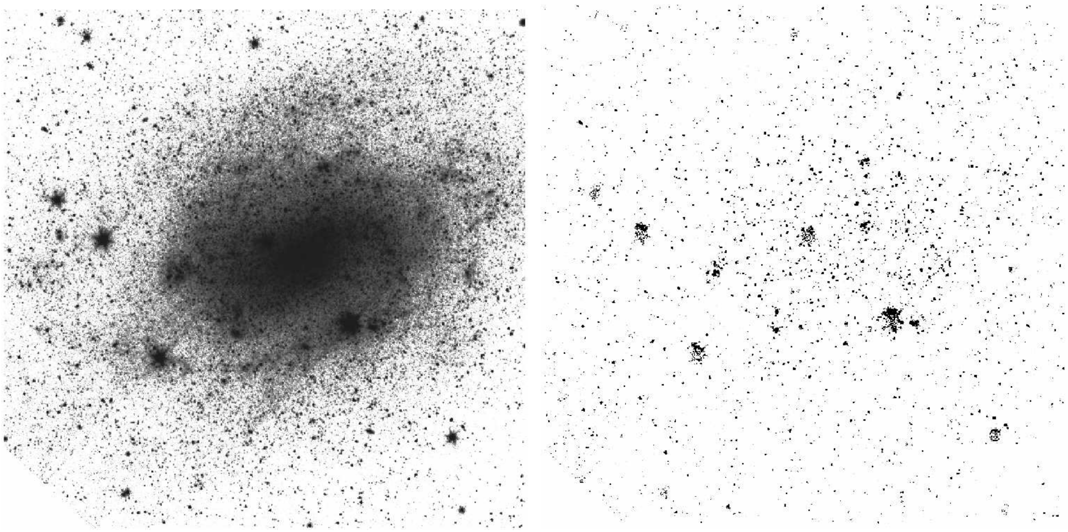

Fig. 2.2.— NGC 300 4.5 μm IRAC image (*left*) and $[3.6]-[4.5]$ image (*right*), as in Figure 2.1. The image covers an area of $\approx 15' \times 15'$ (1250×1250 pixels with $0\farcs75$/pixel).

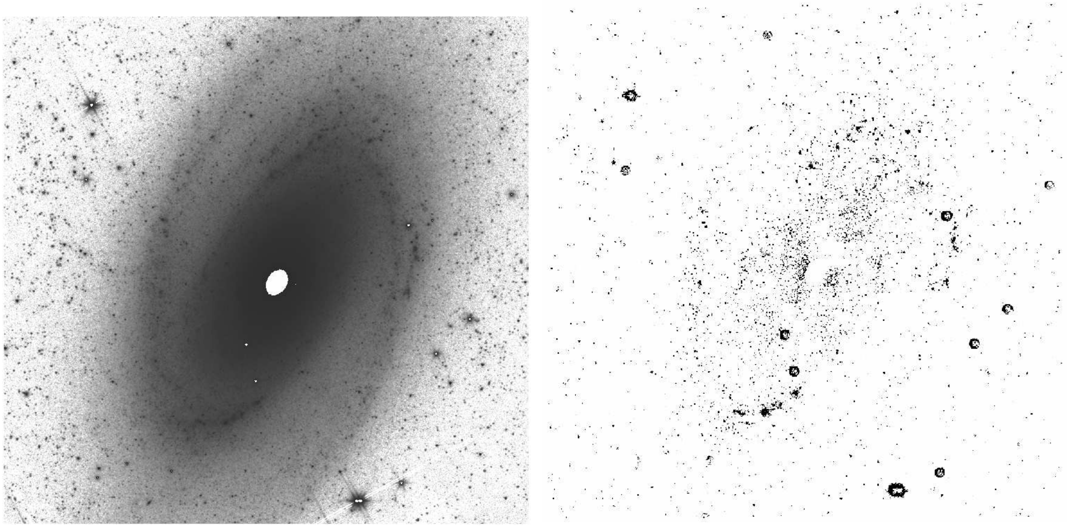

Fig. 2.3.— M81 4.5 μm IRAC image (*left*) and $[3.6]-[4.5]$ image (*right*), as in Figure 2.1. The image covers an area of $\approx 18' \times 18'$ (1450 × 1450 pixels with $0\farcs75$/pixel). The saturated center of M81 has been masked for data reduction purposes.

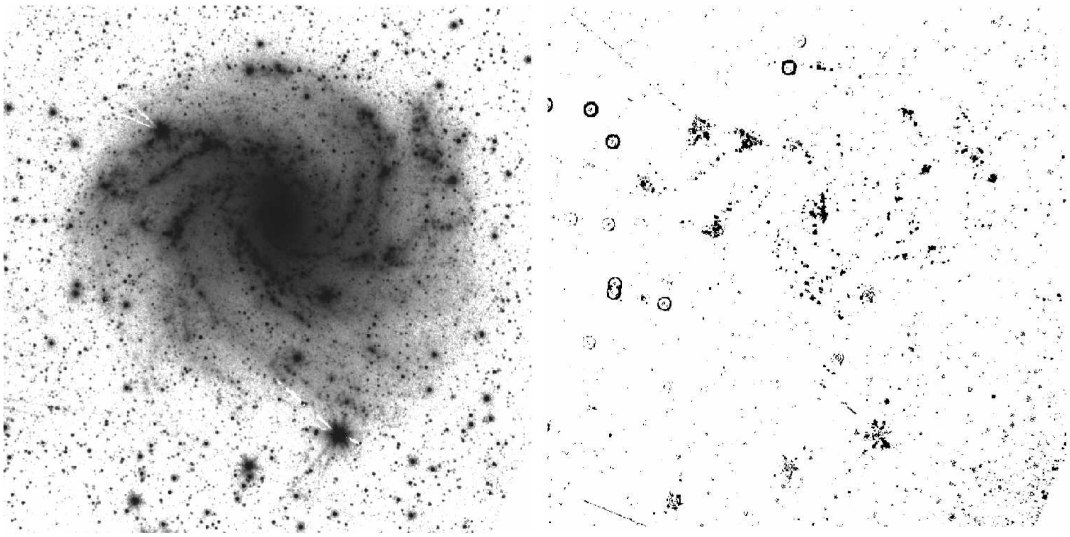

Fig. 2.4.— NGC 6946 4.5 μm IRAC image (*left*) and [3.6] − [4.5] image (*right*), as in Figure 2.1. The image covers an area of $\approx 12' \times 12'$ (1000 × 1000 pixels with $0\farcs75$/pixel). The 4.5 μm SINGS archival image contains many artifacts that significantly affect the subtracted image. For example, bright stars show bright "halos" in the 4.5 μm image that appear as rings in the subtracted image.

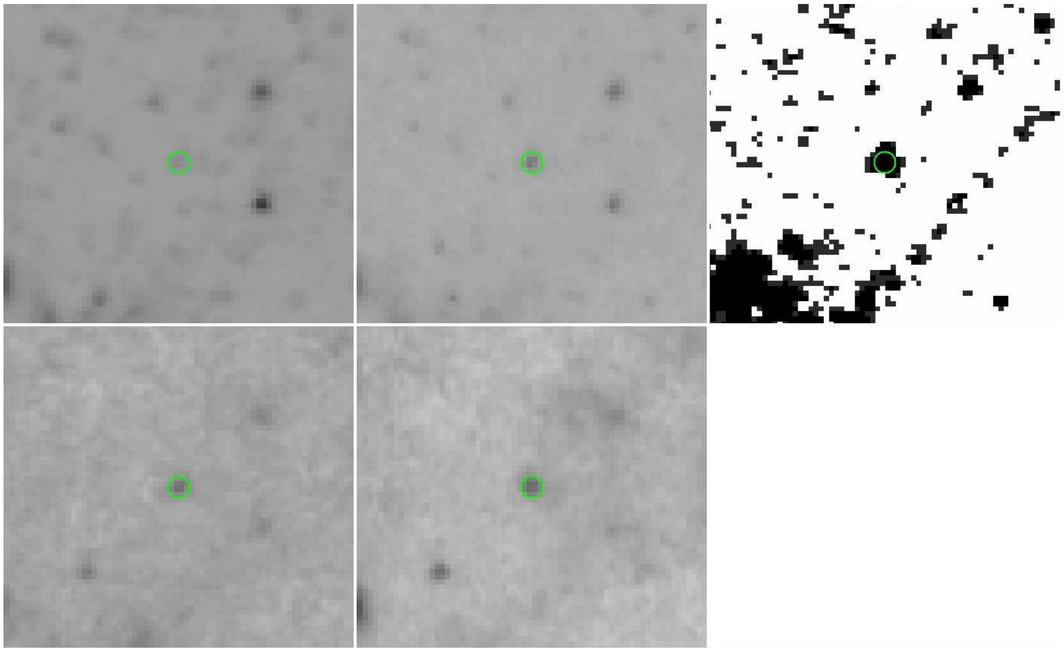

Fig. 2.5.— A Class–A object in NGC 300 visible at both 3.6 μm (*top left*) and 4.5 μm (*top center*). The [3.6] – [4.5] (*top right*), 5.8 μm (*bottom left*), and 8.0 μm (*bottom center*) images are also shown. Each panel is $\sim 52\farcs5$ on its sides.

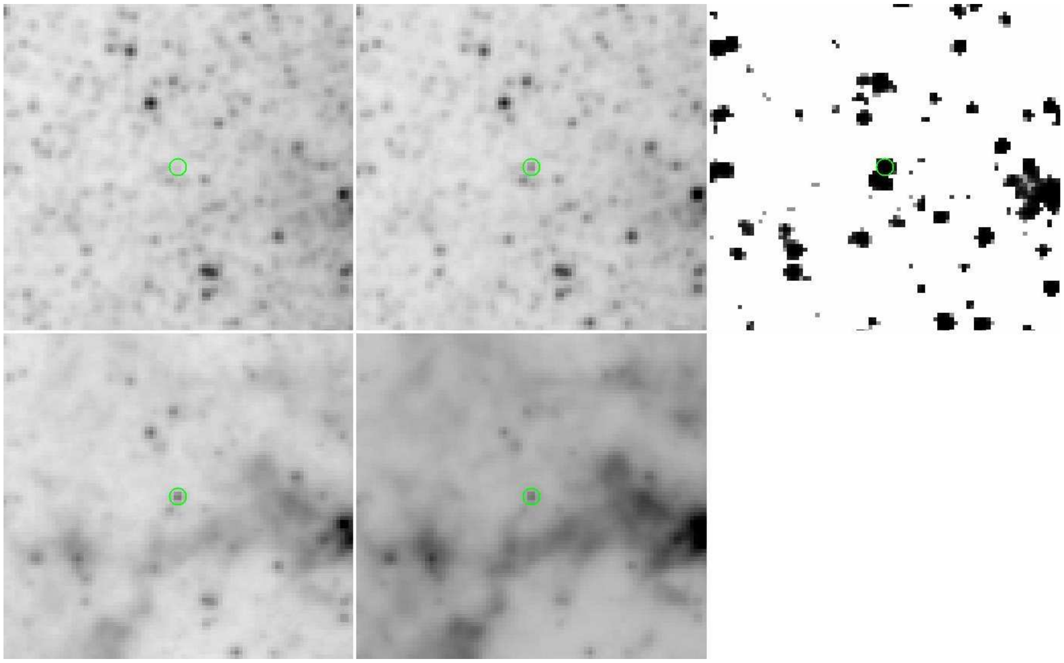

Fig. 2.6.— A Class–B object in M33 visible only at 4.5 μm (*top center*) and not at 3.6 μm (*top left*). The 3.6 μm magnitude is determined at the position of the 4.5 μm source. The $[3.6]-[4.5]$ (*top right*), 5.8 μm (*bottom left*), and 8.0 μm (*bottom center*) images are also shown. Each panel is $\sim 106''\!.4$ on its sides.

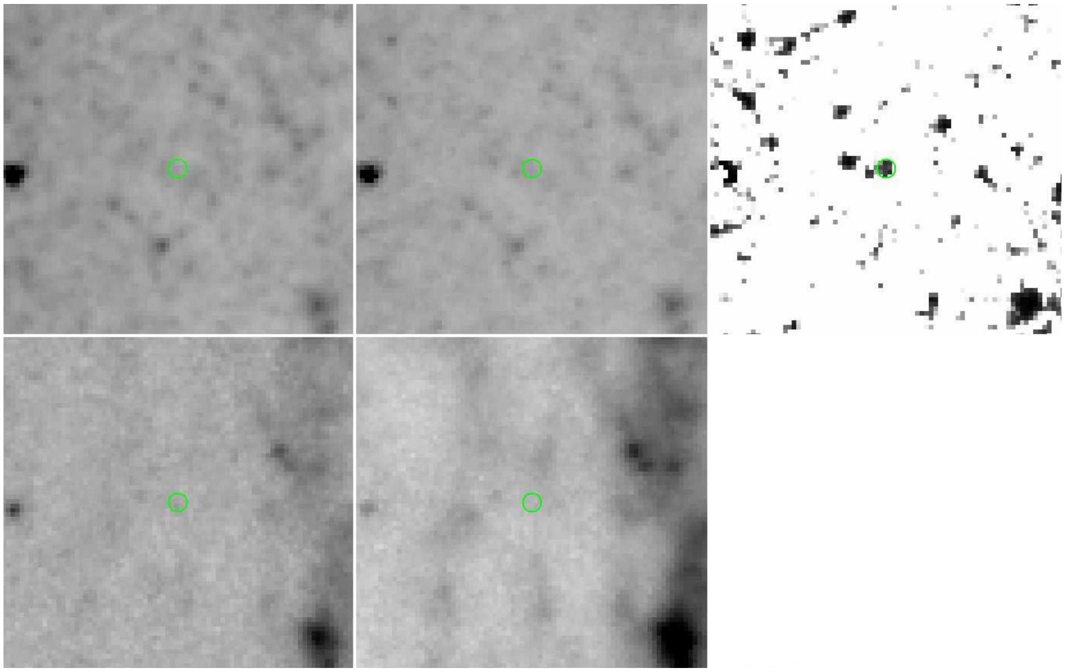

Fig. 2.7.— A Class–C object in M81 found only in the [3.6]−[4.5] image (*top right*) but at neither 3.6 μm (*top left*) nor 4.5 μm (*top center*). The magnitudes are determined through aperture-photometry at the location identified in the differenced image. The 5.8 μm (*bottom left*) and 8.0 μm (*bottom center*) images are also shown. Each panel is $\sim 60''\!.0$ on its sides.

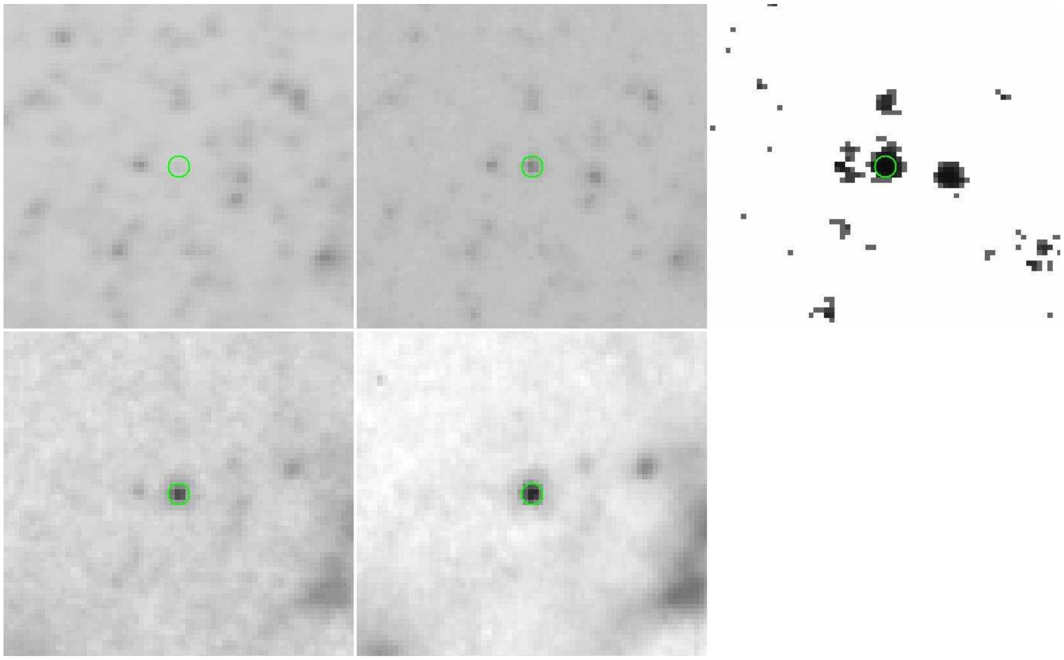

Fig. 2.8.— The NGC 300-2008OT progenitor is identified as a Class–A object detected at both 3.6 μm (*top left*) and 4.5 μm (*top center*). The [3.6] – [4.5] (*top right*), 5.8 μm (*bottom left*), and 8.0 μm (*bottom center*) images are also shown. Each panel is $\sim 60\farcs0$ on its sides.

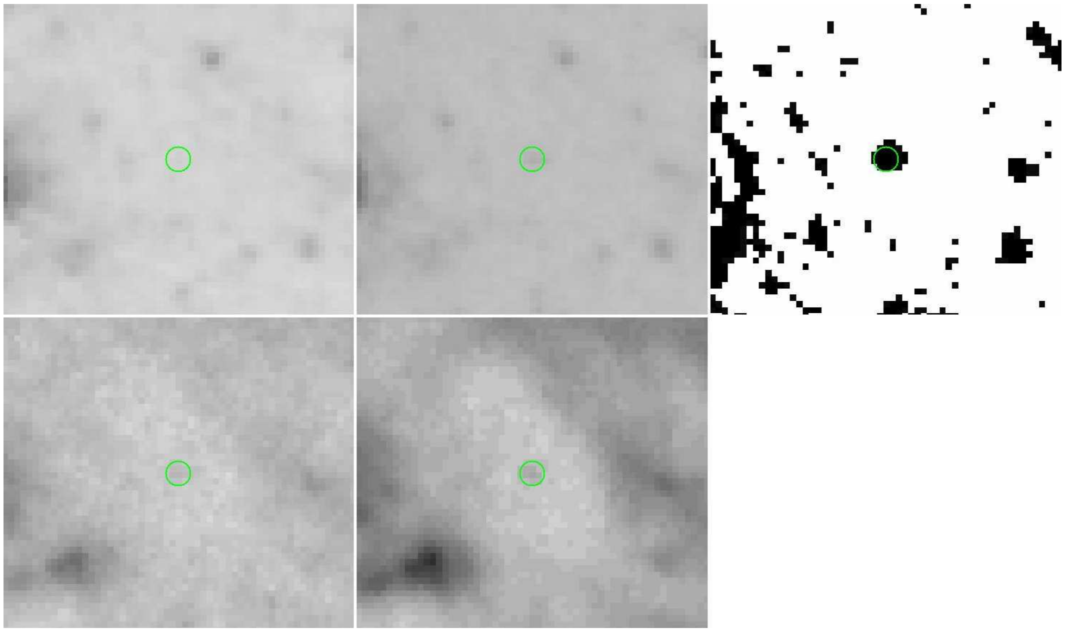

Fig. 2.9.— The SN 2008S progenitor, identified in NGC 6946 as a Class–B object, is detected only at 4.5 μm (*top center*) but not at 3.6 μm (*top left*). The [3.6]-[4.5] image (*top right*) makes it clear that had we missed it at 4.5 μm, it would be detected without any confusion as a Class–C object. The 5.8 μm (*bottom left*), and 8.0 μm (*bottom center*) images are also shown. Each panel is $\sim 41''\!.3$ on its sides.

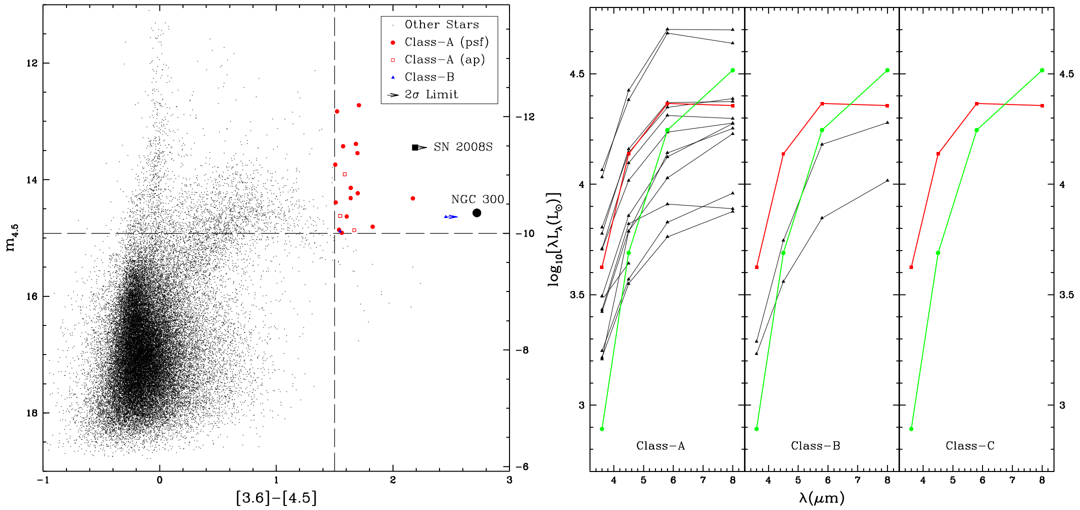

Fig. 2.10.— Mid-infrared CMD (*left*) and EAGB SEDs (*right*) for M33. The apparent magnitude at 4.5 μm is plotted versus $[3.6]-[4.5]$ color for all sources detected in both 3.6 μm and 4.5 μm images through PSF-photometry (black dots). For comparison, the positions of the progenitors of NGC 300-2008OT (black circle) and SN 2008S (black square, lower limit in color) are also shown (Prieto et al. (2008); Prieto (2008)), and the 4.5 μm absolute magnitude scale is shown on the right. The $[3.6]-[4.5] > 1.5$ and $M_{4.5} < -10$ selection for extremely red and bright objects, following the criteria used by Thompson et al. (2009b), is shown by the dashed lines. The EAGB candidates that meet these criteria are shown with different symbols sorted according to the stage of the search at which they were identified. The red circles and open red squares indicate Class–A objects identified through PSF and aperture-photometry, the blue triangles indicate Class–B objects, and the green squares indicate Class–C objects (none in this case).

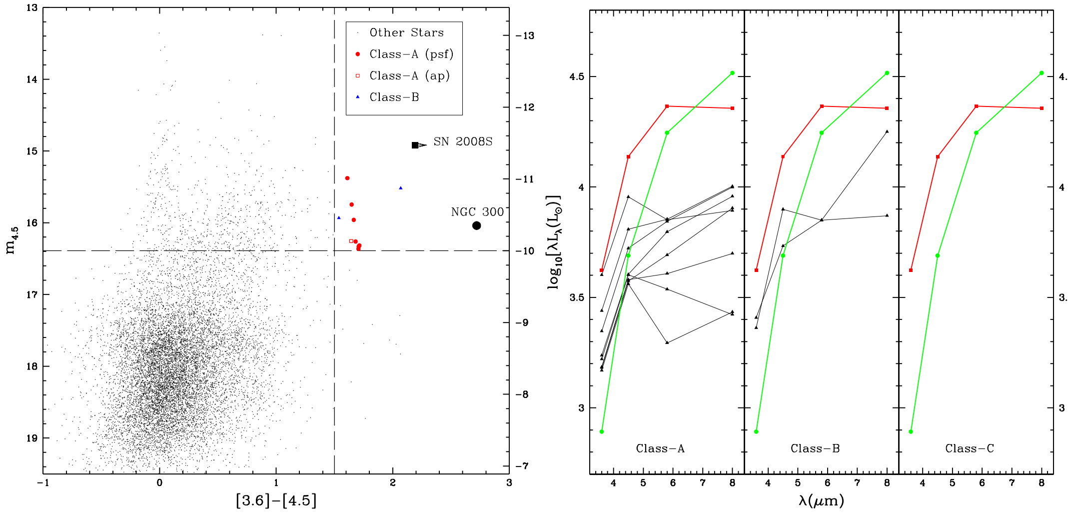

Fig. 2.11.— Mid-infrared CMD (*left*) and EAGB SEDs (*right*) for NGC 300. Symbols and colors used here are the same as in Figure 2.10. The SEDs of some fainter sources show a sharp decline at 5.8 μm before rising again at 8.0 μm due to PAH dominated background contamination.

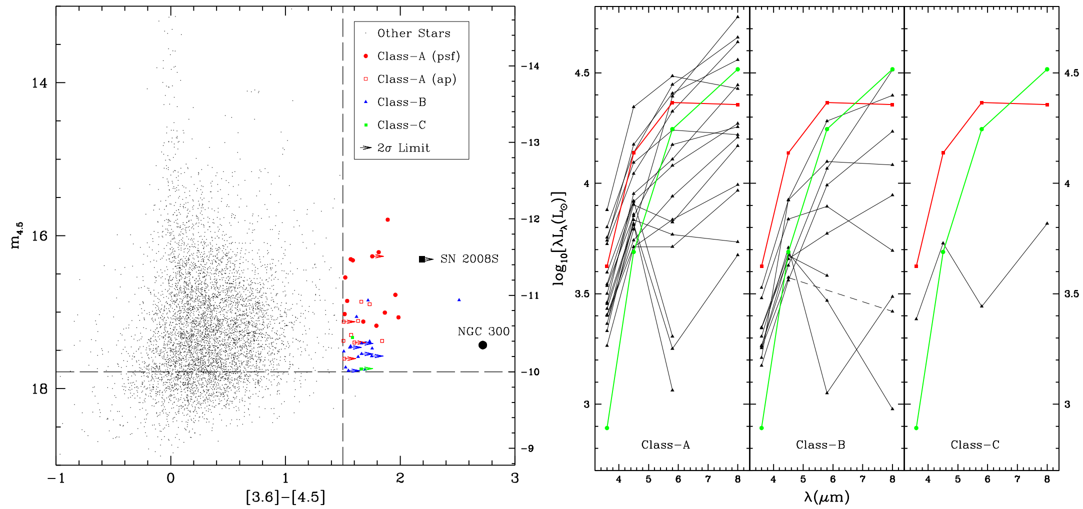

Fig. 2.12.— Mid-infrared CMD (*left*) and EAGB SEDs (*right*) for M81. Symbols and colors used here are the same as in Figure 2.10. The SEDs of some fainter sources show a sharp decline at 5.8 μm before rising again at 8.0 μm due to PAH dominated background contamination. Sources for which 5.8 μm and 8.0 μm measurements could not be obtained at all due to contamination, only the 3.6 μm and 4.5 μm measurements are shown on the SEDs. The dashed line indicates an object for which only the 5.8 μm measurement could not be obtained.

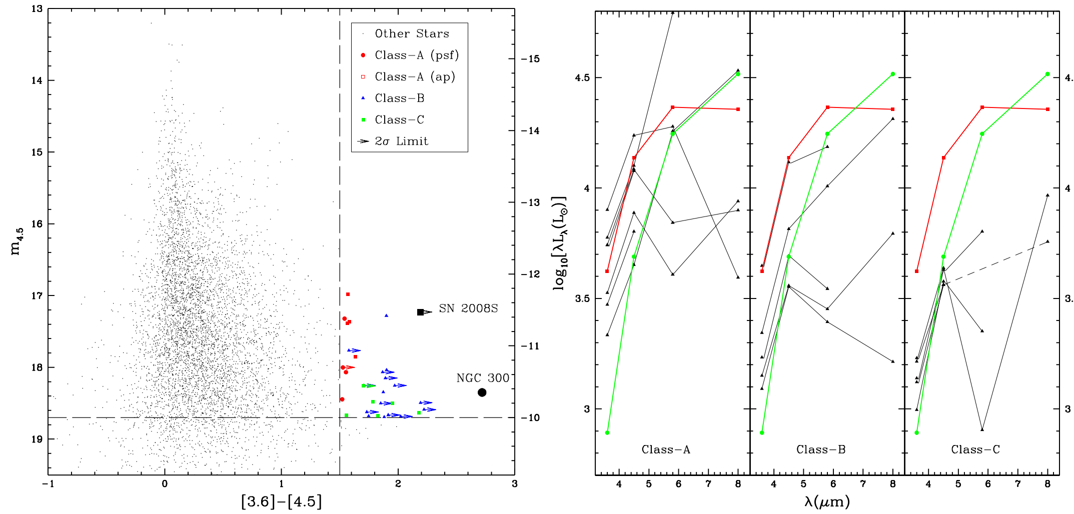

Fig. 2.13.— Mid-infrared CMD (*left*) and EAGB SEDs (*right*) for NGC 6946. Symbols and colors used here are the same as in Figure 2.10. The SEDs of some fainter sources show a sharp decline at 5.8 μm before rising again at 8.0 μm due to PAH dominated background contamination. Sources for which 5.8 μm and 8.0 μm measurements could not be obtained at all due to contamination, only the 3.6 μm and 4.5 μm measurements are shown on the SEDs. The dashed line indicates an object for which only the 5.8 μm measurement could not be obtained.

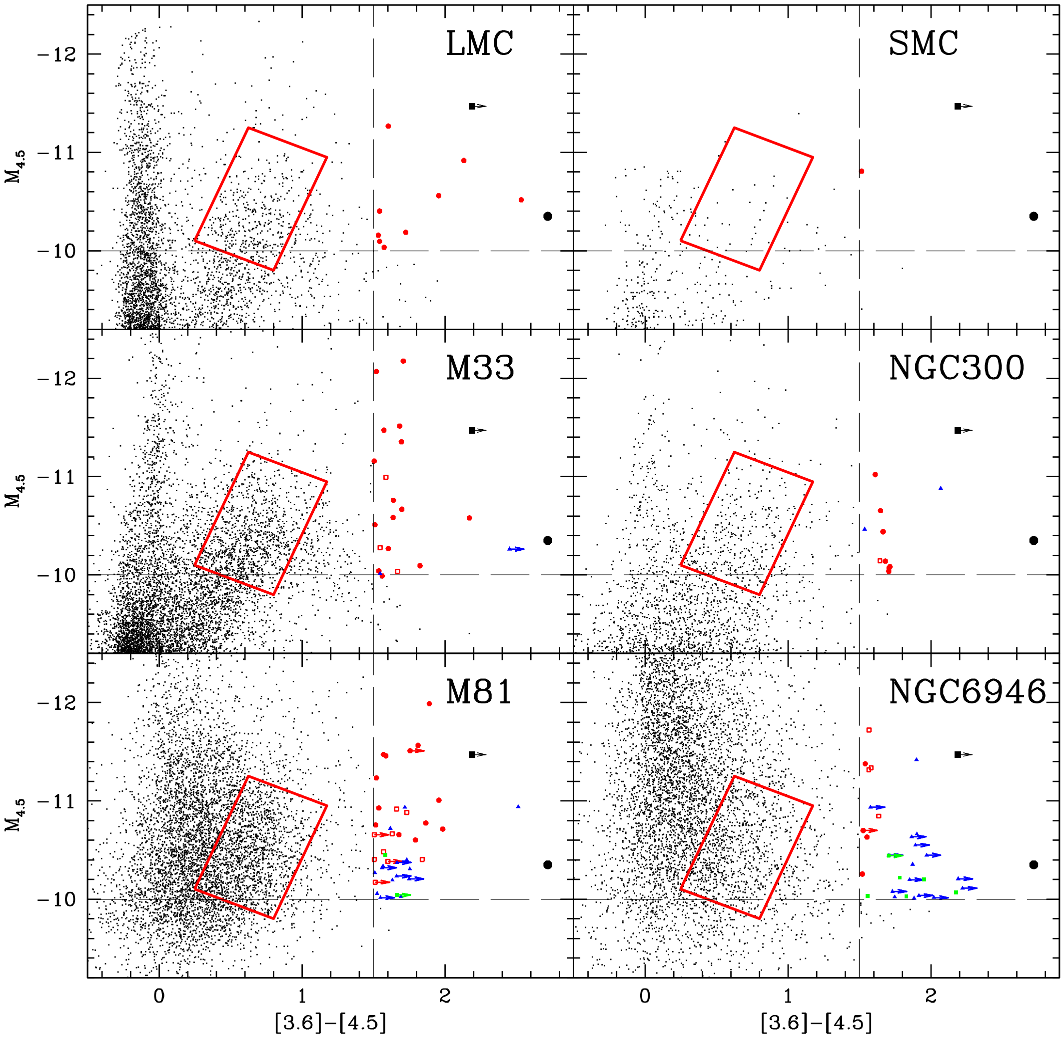

Fig. 2.14.— Mid-infrared CMDs for the six galaxies. Symbols and colors used here are same as in Figure 2.10, and the AGB region is shown in red. The small number of bright objects in the SMC CMD is largely due to the S^3MC survey (Bolatto et al. 2007) covering only portions of the SMC. The AGB regions of the M81 and NGC 6946 CMDs contain significant extragalactic contamination.

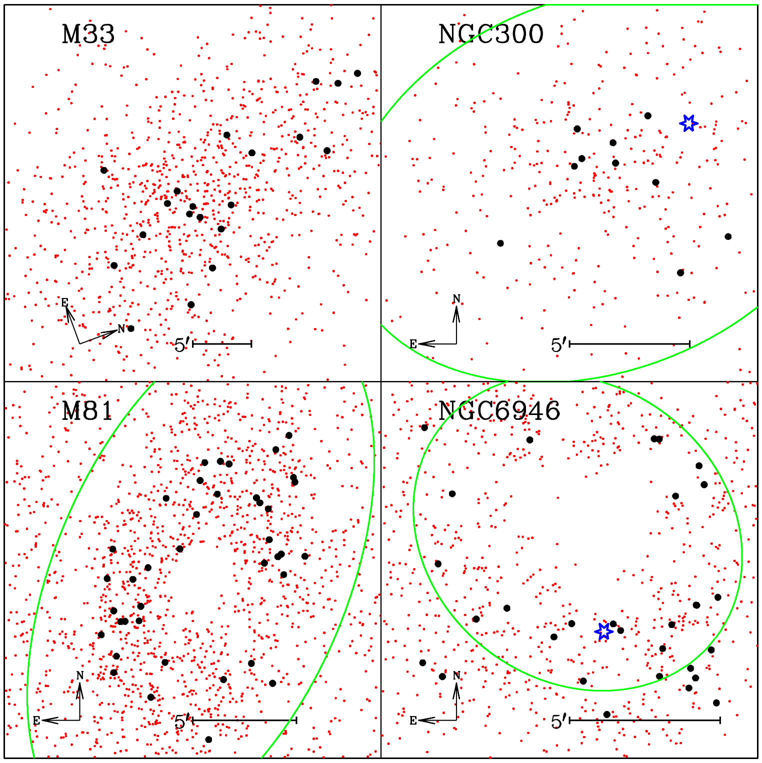

Fig. 2.15.— Distribution of AGB stars (red dots) and EAGB stars (black filled circles), and the two 2008 transient locations (starred blue symbols) in the galaxies. The image scales and directions are indicated in each panel, as well as the R_{25} ellipse (green). For M33, the R_{25} ellipse lies outside of our angular selection region. The empty region at the center of M81 is due to the image mask that we used for the brightest, nearly saturated, central region of the galaxy. However, the notable absence of any AGB and EAGB candidates towards the central region of NGC 6946 is not artificial, as discussed in Section 2.3. We estimate that for NGC 300, M81, and NGC 6946, 90%, 70%, and 50% of our angular selection region is inside the R_{25} ellipse (minus the M81 mask and the "empty" central region of NGC 6946). We use these sky area estimates when scaling the extragalactic contamination from SDWFS.

Table 2.1: EAGB Counts as Fraction of Massive Stars

Galaxy	N_{EAGB}	M_B	Luminosity Ratio to M33	N_{RSG}	N_{EAGB}/N_{RSG}	Ratio to M33
LMC	9	-17.93	0.4	2.2×10^4	4.1×10^{-4}	1.11
SMC	> 1	-16.35	0.1	5.4×10^3	$> 1.8 \times 10^{-4}$	> 0.49
M33	20	-18.87	$\equiv 1.0$	5.4×10^4	3.7×10^{-4}	$\equiv 1.00$
NGC 300	10	-17.92	0.4	2.2×10^4	4.5×10^{-4}	1.24
M81	39	-21.06	7.5	4.1×10^5	1×10^{-4}	0.27
NGC 6946	30	-20.86	6.3	3.4×10^5	0.9×10^{-4}	0.24

Table 2.2: EAGB Counts as Fraction of AGB Stars

Galaxy	N_{EAGB}	N_{AGB} with Contamination	Background Contamination	N_{AGB}	N_{EAGB}/N_{AGB}	Ratio to M33
LMC	9	400	$\equiv 0$	400	0.02	1.0
SMC	> 1	30	$\equiv 0$	30	0.03	1.5
M33	20	1000	30	970	0.02	$\equiv 1.0$
NGC 300	10	330	80	250	0.04	2.0
M81	39	1310	510	800	0.05	2.5
NGC 6946	30	470	260	210	0.14	7.0

Table 2.3: EAGB Counts and SFR

Galaxy	N_{EAGB}	N_{EAGB} Ratio to M33	$\log(L(H\alpha))^{\mathrm{a}}$ (erg/s)	SFR (Hα)$^{\mathrm{b}}$ $M_{\odot}$/yr	SFR (Hα) Ratio to M33
LMC	9	0.5	40.5	0.24	0.7
SMC	> 1	> 0.05	39.7	0.04	0.1
M33	20	$\equiv 1.0$	40.6	0.33	$\equiv 1.0$
NGC 300	10	0.5	40.2	0.13	0.4
M81	39	2.0	40.8	0.46	1.4
NGC 6946	30	1.5	41.4	2.05	6.3

---

[a] Estimates from Kennicutt et al. (2008) scaled for distances used in this chapter.

[b] Estimated using Equation 2 of Lee et al. (2009).

Table 2.4:: Photometry for the EAGBs in LMC[c] and SMC[d]

Galaxy	RA (deg)	Dec (deg)	[3.6] (mag)	[4.5] (mag)	Color	[5.8] (mag)	[8.0] (mag)
LMC	81.694135	−68.813077	8.74	7.13	1.61	5.79	4.37
LMC	83.559766	−69.788996	10.42	7.88	2.21	5.67	3.65
LMC	78.003216	−70.540071	9.94	8.22	1.72	6.82	5.44
LMC	79.801060	−69.152029	9.80	7.84	1.96	6.17	5.01
LMC	80.552349	−67.975638	9.54	8.00	1.54	6.56	5.20
LMC	82.726151	−68.574502	9.78	8.24	1.54	7.10	5.98
LMC	83.332279	−69.695785	9.85	8.31	1.54	7.14	6.05
LMC	84.932592	−69.642732	9.62	7.48	2.14	5.80	4.63

Continued on next page

Table 2.4 – continued from previous page

Galaxy	RA	Dec	[3.6]	[4.5]	Color	[5.8]	[8.0]
	(deg)	(deg)	(mag)	(mag)		(mag)	(mag)
LMC	87.485476	−70.886629	9.94	8.37	1.57	7.08	5.81
SMC	16.246012	−72.147362	9.61	8.09	1.52	…	7.88

Table 2.5:: Photometry for the 20 EAGBs in M33

RA (deg)	Dec (deg)	[3.6] (mag)	[4.5] (mag)	Color	[5.8] (mag)	[8.0] (mag)
23.55626	30.55206	14.43	12.72	1.71	11.27	10.29
23.55223	30.90565	15.07	13.39	1.68	12.10	11.11
23.34230	30.64595	15.00	13.43	1.57	12.15	11.07
23.45476	30.85700	16.49	14.32	2.17	12.67	11.41
23.40428	30.51731	15.24	13.55	1.69	12.25	11.03
23.29855	30.59900	16.47	14.91	1.56	13.62	12.35
23.56806	30.87753	16.63	14.81	1.82	13.77	12.80
23.55592	30.93663	16.40	14.86	1.54	13.45	12.14

Continued on next page

Table 2.5 – continued from previous page

RA (deg)	Dec (deg)	[3.6] (mag)	[4.5] (mag)	Color	[5.8] (mag)	[8.0] (mag)
23.39692	30.67733	15.25	13.74	1.51	12.44	11.35
23.53805	30.73258	15.78	14.14	1.64	12.72	11.36
23.44840	30.65119	14.35	12.83	1.52	11.32	10.45
23.43436	30.57101	15.93	14.23	1.70	13.25	12.32
23.46795	30.61916	15.95	14.32	1.63	12.95	11.47
23.49594	30.75659	16.24	14.63	1.61	13.82	12.90
23.43886	30.64303	15.90	14.39	1.51	13.41	12.49
23.29759	30.50737	15.50	13.91	1.59	12.55	11.27
23.42809	30.70271	16.17	14.62	1.55	13.06	11.26

Continued on next page

Table 2.5 – continued from previous page

RA (deg)	Dec (deg)	[3.6] (mag)	[4.5] (mag)	Color	[5.8] (mag)	[8.0] (mag)
23.42741	30.65543	16.54	14.87	1.67	. . .	. . .
23.48104	30.63851	>17.09	14.64	>2.45	12.92	11.83
23.49179	30.82798	16.43	14.89	1.54	13.41	12.00

Table 2.6: MIR Catalog for 11,241 Point Sources in NGC 300

RA (deg)	Dec (deg)	[3.6] (mag)	$\sigma_{3.6}$	[4.5] (mag)	$\sigma_{4.5}$	Color
13.85991	−37.57455	11.50	0.02	11.50	0.03	0.01
13.62310	−37.81105	12.04	0.02	12.03	0.02	0.01
13.87644	−37.56594	12.04	0.02	12.05	0.01	−0.00
13.71941	−37.81866	12.73	0.01	12.68	0.02	0.04
13.83688	−37.80313	12.93	0.02	12.88	0.03	0.05
...	...	...	...	...	...	...

---

[c] From the catalog published in Blum et al. (2006).

[d] From the catalog published in Bolatto et al. (2007).

Table 2.7:: Photometry for the 10 EAGBs in NGC 300

RA (deg)	Dec (deg)	[3.6] (mag)	[4.5] (mag)	Color	[5.8] (mag)	[8.0] (mag)
13.60942	−37.72041	18.03	16.32	1.71	15.49	14.28
13.80838	−37.72509	18.04	16.33	1.71	15.28	13.76
13.74378	−37.67188	18.07	16.36	1.71	16.27	14.94
13.65096	−37.74543	17.94	16.26	1.68	15.66	14.97
13.71002	−37.65558	17.63	15.96	1.67	14.90	13.53
13.73724	−37.66650	17.39	15.75	1.64	14.87	13.52
13.74127	−37.64604	16.99	15.38	1.61	14.88	13.79
13.67270	−37.68299	17.90	16.26	1.64	15.02	13.63

Continued on next page

Table 2.7 – continued from previous page

RA (deg)	Dec (deg)	[3.6] (mag)	[4.5] (mag)	Color	[5.8] (mag)	[8.0] (mag)
13.70787	−37.66964	17.59	15.52	2.07	14.88	12.90
13.67960	−37.63695	17.47	15.93	1.54	14.88	13.85

Table 2.8: MIR Catalog for 6,021 Point Sources in M81

RA (deg)	Dec (deg)	[3.6] (mag)	$\sigma_{3.6}$	[4.5] (mag)	$\sigma_{4.5}$	Color
149.19633	69.12408	11.26	0.05	11.30	0.04	−0.04
149.32484	69.02681	12.74	0.05	12.80	0.04	−0.06
149.30643	69.05417	12.86	0.03	12.85	0.03	0.02
148.72163	69.06341	12.93	0.04	12.88	0.04	0.05
149.21478	69.12849	13.96	0.02	12.96	0.04	1.00
...	...	...	...	...	...	...

Table 2.9:: Photometry for the 39 EAGBs in M81

RA (deg)	Dec (deg)	[3.6] (mag)	[4.5] (mag)	Color	[5.8] (mag)	[8.0] (mag)
148.67606	69.14224	18.03	16.22	1.81	14.88	13.51
148.65425	69.08266	18.97	17.18	1.79	14.91	13.03
148.89754	69.11637	17.68	15.79	1.89	14.68	13.84
148.72737	68.98086	18.54	17.02	1.52	15.46	14.27
148.83730	68.98399	19.05	17.07	1.98	16.47	15.58
149.06765	69.03034	17.88	16.31	1.57	14.78	13.26
149.00651	69.07363	18.87	17.01	1.86	14.22	12.23
148.74550	69.07730	17.91	16.32	1.59	14.98	13.63

Continued on next page

Table 2.9 – continued from previous page

RA (deg)	Dec (deg)	[3.6] (mag)	[4.5] (mag)	Color	[5.8] (mag)	[8.0] (mag)
149.02259	69.04263	18.39	16.85	1.54	17.63	...
148.88968	69.14354	18.73	16.77	1.96	15.62	13.80
148.93513	69.08881	18.80	17.12	1.68	18.24	...
149.09832	69.06480	18.07	16.55	1.52	15.08	13.31
149.02652	69.03100	>18.03	16.27	>1.76	15.54	14.57
148.84383	69.15902	18.52	16.86	1.66	15.69	14.24
149.07671	69.00262	18.63	16.90	1.73	16.33	14.49
148.71896	69.16830	19.22	17.38	1.84	16.31	14.92
148.75517	69.12566	18.74	17.11	1.63	17.77	15.72

Continued on next page

Table 2.9 – continued from previous page

RA (deg)	Dec (deg)	[3.6] (mag)	[4.5] (mag)	Color	[5.8] (mag)	[8.0] (mag)
148.76269	69.12973	18.87	17.30	1.57	16.04	14.39
148.96612	69.12932	18.88	17.37	1.51	16.61	14.99
148.99972	68.96981	>19.00	17.40	>1.60	16.89	. . .
148.96812	68.99771	>19.12	17.61	>1.51	16.09	14.55
148.73406	69.09608	>18.63	17.12	>1.51	16.34	15.44
149.04063	69.06424	>19.31	17.76	>1.55	18.52	16.15
148.77491	68.99690	19.44	17.75	1.69	15.92	14.33
148.87053	68.93584	19.25	17.72	1.53	. . .	16.36
148.87911	69.15796	19.22	17.59	1.63	15.73	13.63

Continued on next page

Table 2.9 – continued from previous page

RA (deg)	Dec (deg)	[3.6] (mag)	[4.5] (mag)	Color	[5.8] (mag)	[8.0] (mag)
149.08604	69.08849	>19.21	17.55	>1.66	16.00	14.52
148.70745	69.08449	19.02	17.51	1.51	16.46	15.05
148.82431	69.15687	19.23	17.47	1.76	16.94	. . .
148.73618	69.12076	>19.02	17.46	>1.56	. . .	. . .
148.68902	69.17968	19.01	17.44	1.57	17.22	17.46
149.11110	69.01974	>19.07	17.41	>1.66	16.73	15.42
149.05787	69.03054	19.11	17.38	1.73	18.27	16.20
149.08270	68.98944	18.68	17.06	1.62	16.16	15.67
148.85093	69.13267	18.56	16.84	1.72	15.65	14.70

Continued on next page

Table 2.9 – continued from previous page

RA (deg)	Dec (deg)	[3.6] (mag)	[4.5] (mag)	Color	[5.8] (mag)	[8.0] (mag)
148.67919	69.14593	19.36	16.84	2.52	15.19	13.92
148.70187	69.06804	>19.32	17.57	>1.75	16.04	14.21
148.71479	69.08243	>19.40	17.74	>1.66	17.31	16.86
149.08331	69.03896	18.92	17.33	1.59	17.29	15.36

Table 2.10: MIR Catalog for 5,601 Point Sources in NGC 6946

RA (deg)	Dec (deg)	[3.6] (mag)	$\sigma_{3.6}$	[4.5] (mag)	$\sigma_{4.5}$	Color
308.77542	60.06477	12.94	0.03	12.78	0.03	0.16
308.72086	60.17000	13.09	0.03	13.20	0.03	−0.12
308.80408	60.04553	13.53	0.03	13.50	0.03	0.04
308.69391	60.11113	13.57	0.03	13.51	0.03	0.06
308.77582	60.09848	13.66	0.03	13.51	0.03	0.15
...	...	...	...	...	...	...

Table 2.11:: Photometry for the 30 EAGBs in NGC 6946

RA (deg)	Dec (deg)	[3.6] (mag)	[4.5] (mag)	Color	[5.8] (mag)	[8.0] (mag)
308.74430	60.09641	>19.53	18.00	>1.53	17.22	16.32
308.68564	60.05348	19.62	18.07	1.55	...	...
308.57731	60.18055	18.86	17.32	1.54	14.83	12.83
308.85752	60.17550	19.97	18.45	1.52	16.17	14.50
308.58661	60.11402	19.49	17.86	1.63	17.80	15.98
308.58305	60.19101	18.94	17.36	1.58	17.21	16.08
308.60922	60.17430	18.55	16.98	1.57	16.12	16.84
308.79663	60.11229	18.95	17.38	1.57	...	...

Continued on next page

Table 2.11 – continued from previous page

RA (deg)	Dec (deg)	[3.6] (mag)	[4.5] (mag)	Color	[5.8] (mag)	[8.0] (mag)
308.62378	60.08993	>19.96	18.25	>1.71	17.22	15.98
308.88858	60.21206	>20.71	18.69	>2.02	...	15.49
308.58582	60.11384	>20.04	18.15	>1.89	17.51	16.51
308.62727	60.07459	>20.35	18.50	>1.85	17.27	16.87
308.87304	60.13669	>20.22	18.25	>1.97	17.75	20.10
308.67866	60.10364	>19.94	18.07	>1.87	17.36	14.64
308.83064	60.10620	>20.68	18.49	>2.19	...	...
308.62745	60.20580	>20.58	18.66	>1.92	...	...
308.77135	60.20534	19.94	18.04	1.90	16.79	15.05

Continued on next page

Table 2.11 – continued from previous page

RA (deg)	Dec (deg)	[3.6] (mag)	[4.5] (mag)	Color	[5.8] (mag)	[8.0] (mag)
308.72470	60.10376	19.18	17.28	1.90	16.35	. . .
308.56433	60.05990	20.57	18.69	1.88	18.33	17.80
308.63279	60.20597	20.22	18.35	1.87	17.96	. . .
308.71184	60.07200	20.43	18.68	1.75	18.18	16.35
308.67038	60.09997	>19.35	17.77	>1.58	16.71	16.09
308.56994	60.08913	>20.81	18.59	>2.22	17.32	17.35
308.59289	60.07903	>20.35	18.62	>1.73	16.87	18.58
308.61373	60.10318	>19.96	18.26	>1.70	. . .	18.88
308.56247	60.11828	20.81	18.63	2.18	18.44	. . .

Continued on next page

Table 2.11 – continued from previous page

RA (deg)	Dec (deg)	[3.6] (mag)	[4.5] (mag)	Color	[5.8] (mag)	[8.0] (mag)
308.88990	60.08202	20.45	18.50	1.95	17.31	19.94
308.86798	60.07440	20.50	18.67	1.83	...	16.44
308.59478	60.06813	20.26	18.48	1.78	19.55	15.92
308.58739	60.07366	20.23	18.67	1.56	20.11	...

Chapter 3: *Object-X*: The Brightest Mid-IR Point Source in M33

Note: This chapter is based on the paper "Object-X: The Brightest Mid-IR Point Source in M33", by R. Khan, K. Z. Stanek, C. S. Kochanek, and A. Z. Bonanos, published in the Astrophysical Journal, 732:43, in May 2011 (Khan et al. 2011).

3.1. Introduction

Explaining mass loss from massive stars, especially episodic mass loss in evolved massive stars, is one of the outstanding problems in stellar evolution theory. Systematic studies of rare, luminous, dusty massive stars in nearby galaxies were carried out in parallel by Bonanos et al. (2009, 2010) for the Large and Small Magellanic Clouds (LMC and SMC), and Thompson et al. (2009a) and Khan et al. (2010a) for M33, NGC 300, M81, and NGC 6946. Luminous blue variables (LBVs), supergiant B[e] (sgB[e]), some Wolf-Rayet stars (WRs) and red supergiants (RSGs) contribute to this class of objects, and their rarity implies they are a very short but perhaps critical stage in the evolution of massive stars. Given that the LBV mass loss mechanism is poorly understood (Humphreys & Davidson 1994; Smith & Owocki 2006) and that there is mounting evidence for some core collapse supernovae with dust enshrouded progenitors (Prieto et al. 2008; Thompson et al. 2009a) or very recent mass loss episodes (Gal-Yam et al. 2007; Smith 2008, and references therein), a census of these stars in nearby galaxies is vital for understanding the mass loss mechanisms and final stages of evolution of massive stars.

Bonanos et al. (2009, 2010) cross-matched massive stars with known spectral types with the SAGE and SAGE-SMC photometric databases, which resulted in a multi-band photometric catalog from 0.3 to 24μm providing spectral energy distributions (SEDs) for most classes of hot and cool stars. These works showed that in the LMC and the SMC, the LBVs, RSGs, and sgB[e] stars are some of the most-luminous mid-IR sources, due to the combination of high actual luminosities with surrounding dust from recent episodic mass ejections. However, these studies required the presence of a bright optical, spectroscopically classified source. The opposite approach, focusing on bright mid-IR sources, was undertaken by Thompson et al. (2009a) and Khan et al. (2010a).

The Thompson et al. (2009a) re-analysis of the McQuinn et al. (2007) mid-IR images of M33 focused on detecting extremely red (optically thick even at 3.6μm) analogs of the progenitors of SN 2008S and the NGC 300 optical transient, finding that such analogs are extremely rare. Less red, but more luminous, stars are still rare, and only in some cases do they correspond to LBVs and other spectroscopically classified evolved stars. In Khan et al. (2010a), we carried out a systematic mid-IR photometric search for self-obscured stars in four galaxies: M33, NGC 300, M81, and NGC 6946. In particular, we confirmed the conclusion of Thompson et al. (2009a) that stars analogous to the progenitors of SN 2008S and NGC 300 transients are truly rare—there may be as few as ~ 1 per galaxy at any given moment. This result empirically supports the idea that the dust-enshrouded phase is a very short-lived phenomenon in the lives of some massive stars.

At this point, we set out to examine the most luminous mid-IR sources in M33 that had not been considered by either Thompson et al. (2009a) or Khan et al. (2010a). In this chapter, we discuss the nature of the brightest mid-IR star in M33. We started by examining the brightest objects off the primary stellar locus in the mid-IR CMD of M33 (Figure 3.1, adopted from Thompson et al. 2009a, also see Figure 3.2). The brightest source is a known compact, young star cluster IC133. It is spatially unresolved by *Spitzer*, but immediately recognizable as a star cluster. It is both too luminous to be a single star ($L_\star > 10^7 L_\odot$) and its mid-IR SED peaks at a temperature ($\sim$ 30K) that is too cold for dust associated with material ejected by a single star (because the required mass $\propto L_\star T_d^{-4}$). The second brightest source, the brightest mid-IR star in all of M33, is the subject of this chapter. We call this star, located at R.A.=$1^h33^m24\overset{s}{.}1$ and Dec.=$+30°25'34\overset{''}{.}8$ (J2000.0), "Object X".

Figure 3.3 shows its location in M33, and Figure 3.4 shows the V-band through 24 μm band images of its surrounding region based on the data we describe in Section 3.2. Section 3.3 presents the SED and simple models of it. Section 3.4 discusses the possible explanations of the physical nature of Object X and its implications for understanding the late-stage evolution of the most massive stars.

3.2. Data

The optical photometry ($UBVRI$ and Hα) was measured from the Local Group Galaxies Survey images (Massey et al. 2006). The catalog of M33 point sources published by Massey et al. (2006) does not include Object X as a point source because it did not satisfy their criterion that it is >4 sigma above the background. We used DAOPHOT/ALLSTAR (Stetson 1992) to identify point sources in the $UBVRI$ bands. Object X is identified as a relatively faint and red point source in the VRI bands with a $> 3\sigma$ detection. However, it is not detected in the U

and B bands. We estimated 3σ upper limits on its luminosity in these bands using the APPHOT/PHOT package. The measured magnitudes and the limits were transformed to the Vega-calibrated system using zero-point offsets determined from the bright stars in the Massey et al. (2006) catalog of M33 point sources.

The near-IR (JHK_s) images were taken from the 2MASS survey (Skrutskie et al. 2006) and the calibrated JHK_s magnitudes were obtained from the 2MASS All-Sky Catalog of Point Sources (Cutri et al. 2003).

For the mid-IR photometry, we used the six co-added epochs of data from McQuinn et al. (2007) as processed and used by Thompson et al. (2009a) and Khan et al. (2010a). For the MIPS 24 μm band, we downloaded the Post-Basic Calibrated Data (PBCD) from the *Spitzer* archive (Program 5, PI: Gehrz). Although we examined the MIPS 70 μm and 160 μm images for the target region as well, we were unable to obtain reliable flux measurements due to the nearby H II region being extremely luminous in these two bands. We measured the magnitudes using DAOPHOT/ALLSTAR (Stetson 1992). The PSF-magnitudes obtained with ALLSTAR were transformed to Vega-calibrated magnitudes using aperture corrections derived from bright stars using the APPHOT/PHOT package. Figures 3.1 and 3.2 show the mid-IR CMDs of M33.

The measured fluxes are reported in Table 1, and V-band through 24 μm band images of Object X are shown in Figure 3.4.

We also examined the photographic plates from the 48 inch Oschin Schmidt Telescope used in the STScI Digitized Sky Survey. The first image (epoch 1949) was a POSS-I Red Plate, while the second (epoch 1991) was a POSS-II RG610 filter. Both of these are roughly comparable to the modern standard R-band. Neither image shows an optical source at the location of Object X. These images are much shallower than the Local Group Survey (Massey et al. 2006). Based on the faintest *R*-band USNO stars in this region and calibrating them by their counterparts in Massey et al. (2006), we estimate an upper limit of R$\gtrsim$ 20.0 magnitude for Object X in 1949. This is consistent with our detection of Object X at R$\simeq$ 21.6 (epoch 2001). The epoch 1991 image also does not show a source, but we were unable to converge on a self-consistent calibration for the region, and so will not discuss this image further. Figure 3.5 shows these historical images of this region.

Object X is identified as an optically variable point source in the Canada-France-Hawaii Telescope (CFHT) photometric survey of M33 (Hartman et al. 2006). Figure 3.6 shows the r' and i' band lightcurves of Object X from this survey. The correlated short-term variability of $\sim$ 0.4 magnitude (fractional variability of $\sim$45%), definitively indicates that it is a single stellar object rather than multiple objects blended together. If we were to dilute the source with additional non-variable sources of comparable total luminosity, the observed $\sim$ 0.4 magnitude variability would be unphysical. This is significant given the lack of archival HST images for this location.

McQuinn et al. (2007) collected six epochs over two years and identified Object X as a variable source in the mid-IR, although for this chapter, we use the mid-IR lightcurves generated by Thompson et al. (2009a). Figure 3.7 shows the 3.6 μm and 4.5 μm band lightcurves. Object X shows correlated variability of about $\sim$0.15 magnitude in both bands (fractional variability of $\sim$15%). This suggests that the dust opacity and geometry surrounding Object X are not undergoing any rapid evolution.

3.3. Analysis

Figure 3.8 shows the spectral energy distribution (SED) of Object X. The low optical luminosity means that Object X is unlikely to be a YSO embedded in a dusty disk, and if we model the SED using the YSO models of Robitaille et al. (2006), we find no good, or even plausible fits[1]. In essence, $\lesssim$1% of the luminosity is emitted in the optical, while even edge-on YSO disk models tend to scatter more optical light into the observer's line of sight.

The alternate is that we are examining a self-obscured star. For this case, we fit the SED of the source using DUSTY (Ivezic & Elitzur 1997; Ivezic et al. 1999; Elitzur & Ivezić 2001) to model the radiation transfer through a spherical dusty medium surrounding a star. We considered models using either the graphitic or silicate dust models of Draine & Lee (1984). We distributed the dust either as a shell, with ratios of outer to inner radii of either 2:1 or 4:1, or with the standard DUSTY wind model. The density distributions inside the shells were assumed to be $\rho \propto 1/r^2$. The models are defined by the stellar luminosity, L_*, stellar temperature, T_*, the V-band optical depth τ_V, and the dust temperature at the inner edge of the dust distribution, T_d. The stellar luminosity and the dust temperature together determine the radius of the inner edge of the dust distribution. To fit the data we tabulated the DUSTY models on a grid of stellar temperatures, optical depths and dust temperatures.

We find that two dust types that can fit the SED equally well but with very different preferred stellar temperatures. The graphitic models prefer cool stars, $T_* \simeq 5000$ K, while the silicate models prefer hot stars, $T_* \simeq 20000$ K. The stellar

---

[1] We fit the SED using the online tool (Robitaille et al. 2007) at `http://caravan.astro.wisc.edu/protostars/sedfitter.php`.

luminosity is $L_* \simeq 10^{5.6} L_\odot$ to $10^{5.8} L_\odot$ with the silicate models favoring the somewhat higher luminosities (see Figure 3.9). The three different dust geometries produce similarly good statistical fits. For the fits we assumed minimum flux uncertainties of 20% and included the optical upper limits as constraints, leading to $\chi^2 \simeq 43$ for $N_{dof} = 9$ for the best fits. Each model was a modestly poor match to some part of the SED, but this is not very surprising given our use of a simple spherical model and a discrete sampling of its parameter space. A clear detection (or not) of the silicate dust feature near 10 μm would determine the dust composition. The typical optical depths and inner/outer dust temperatures were $\tau_V \simeq 8.5$ and $T_d \simeq 500/150$ K for the graphitic models, and $\tau_V \simeq 11.5$ and $T_D \simeq 1200/300$ K for the silicate models. Much of this difference is created by the higher scattering opacities of the silicate dust. The inner edge of the dust lies at $R_{in} \simeq 10^{16.3}$ cm for the graphitic models and $R_{in} \simeq 10^{15.8}$ cm from the silicate models.

Based on the CO and H I data from (Gratier et al. 2010), the estimated column density at the location of Object X is $\sim 7 \times 10^{21}$ atoms/cm^2 (P. Gratier, private communication), where the higher number comes from using the CO to estimate the amount of H_2. For a standard Galactic dust to gas ratio of $E(B-V) = 1.7 \times 10^{-22}$ mag cm^2/atom (Bohlin et al. 1978), this implies a maximum foreground extinction in M33 of roughly $E(B-V) \simeq 1.2$ magnitude. Adding this to the Galactic extinction changes the DUSTY models very little, modestly reducing the optical depths ($\Delta\tau \sim 3-4$) and slightly raising the stellar luminosity (by $\sim$20%).

If we search the Padova stellar models (Marigo et al. 2008) for stars with such luminosities, there are examples with both the high and low stellar temperatures, although the higher temperature stars of the silicate models are preferred. The stellar masses are always $\gtrsim 30 M_\odot$, but without an independent constraint on the stellar temperature it is difficult to say more. In many, but not all cases, the stars have lost significant fractions of their initial masses.

We also note that while stars ordinarily do not have significant Hα emission, Object X is a strong Hα source. We determine this by using difference imaging methods to match the Hα image to the flux scale and PSF structure of the R-band image and then subtract. All the normal stars disappear to leave us only with the stars having significant Hα emission. In practice, we use the ISIS image subtraction software package (Alard & Lupton 1998; Alard 2000) following the procedures of Khan et al. (2010a). Figure 3.10 shows the result of this procedure for the region around Object X. It is clear from the subtracted image that Object X is a strong Hα emission source.

3.4. Discussion

An evolved star can cloak itself in dust through two broad mechanisms, winds and mass ejection. The classic examples of wind obscured stars are the AGB stars. In the most extreme cases, such as the progenitors of SN 2008S and the 2008 NGC 300 transient, the wind can be optically thick even in the mid-IR (Prieto et al. 2008). Shells formed by impulsive mass ejections are seen around many evolved massive stars (e.g., Humphreys & Davidson 1994; Humphreys et al. 1997; Smith & Frew 2010; Gvaramadze et al. 2010; Wachter et al. 2010), and they are distinguished by the frequency of the ejections, their mass, and their velocities. The most famous example is the "Great Eruption" of η Carina in the 19th century, which ejected $\sim 10 M_\odot$ of material at velocity ~ 600 kms^{-1} (Humphreys & Davidson 1994). At the other end of the velocity spectrum are the OH/IR stars such as IRC+10420, where the ejection velocities are closer to ~ 50 kms^{-1} (Tiffany et al. 2010).

Our best constraint on these possibilities comes from the time variability of the source. The absence of the source in 1949 means that the star has been obscured for at least 60 years, but the SED models require fairly hot dust close to the star. If we assume that the material obscuring the star today is the same as that obscuring the star in 1949, we get characteristic velocities of the order of ~ 114 kms^{-1} and ~ 36 kms^{-1} for the graphitic and silicate models, respectively. The outer edge then requires a velocity twice as large for a shell with a 2:1 ratio between the inner and outer edges. These velocity scales favor the slower ejections of the OH/IR stars over the higher velocities of the giant LBV eruptions like η Carina. The significant optical and mid-IR variability then favors a patchy evolving ejecta over a steady wind. The extended period of the obscuration comes close to requiring multiple ejections, approaching the limit of an unsteady wind. It would be interesting to determine if the source was visible in still older archival plates, if any exist, since it would be a relatively bright R $\simeq 16$ mag source without the dust.

Overall, Object X seems to most closely resemble the cool, hypergiant, stars such as IRC+10420 and Var A. The three sources have comparable bolometric luminosities of $\sim 10^{5.7} L_{\odot}$, although their SEDs, shown in Figure 3.8, differ because Object X is more obscured. In the case of IRC+10420, the star is surrounded by a series of shells and seems to have undergone a period of high mass loss for the last ~ 600 years (Humphreys et al. 1997) that ended 50-100 years ago leading to its current optical brightening (Blöcker et al. 1999). Var A, on the other hand, seems to have had a brief period of high mass loss rates over the last ~ 50 years and is now re-emerging in the optical (Humphreys et al. 2006). Object X would seem to be intermediate, requiring a longer period of heavy mass loss than Var A, but perhaps less than IRC+10420. If Object X is a true analog to IRC+10420 or Var A, then it may conceivably emerge from its current self-obscured state over the next few decades since the optical depth of an expanding shell drops as $\tau \propto t^{-2}$. We cannot make this statement with any degree of certainty, as each of these objects are going through tumultuous evolutionary phases that are both unique and poorly understood. Follow-up observations of this source at all wavelengths should begin to reveal its long term evolution and may provide us with unexpected surprises. Deep optical and IR spectra of Object X will enable to us to determine the spectral type of the central star and place it on an H-R diagram.

Stars like Object X are extremely rare. As a unique star in a brief yet eventful evolutionary state, we encourage further study of this interesting object. Furthermore, there is mounting evidence that mass loss from massive stars may be dominated by impulsive transients rather than steady winds (e.g., Smith & Owocki 2006), particularly with the downward revision of mass-loss rates in recent years (e.g., Fullerton et al. 2006). If so, the period in which mass loss is most important will also tend to be the period when the star is most obscured. Surveys of massive stars such as those by Massey et al. (2006) and Bonanos et al. (2009, 2010), which focus on bright optical sources, will miss Object X and similar sources that may best probe the frequency and duration of these mass loss episodes as well as the amount of ejected mass. Characterizing these stars and the amount of mass loss by massive stars clearly requires systematic surveys in the mid-IR as well as the optical.

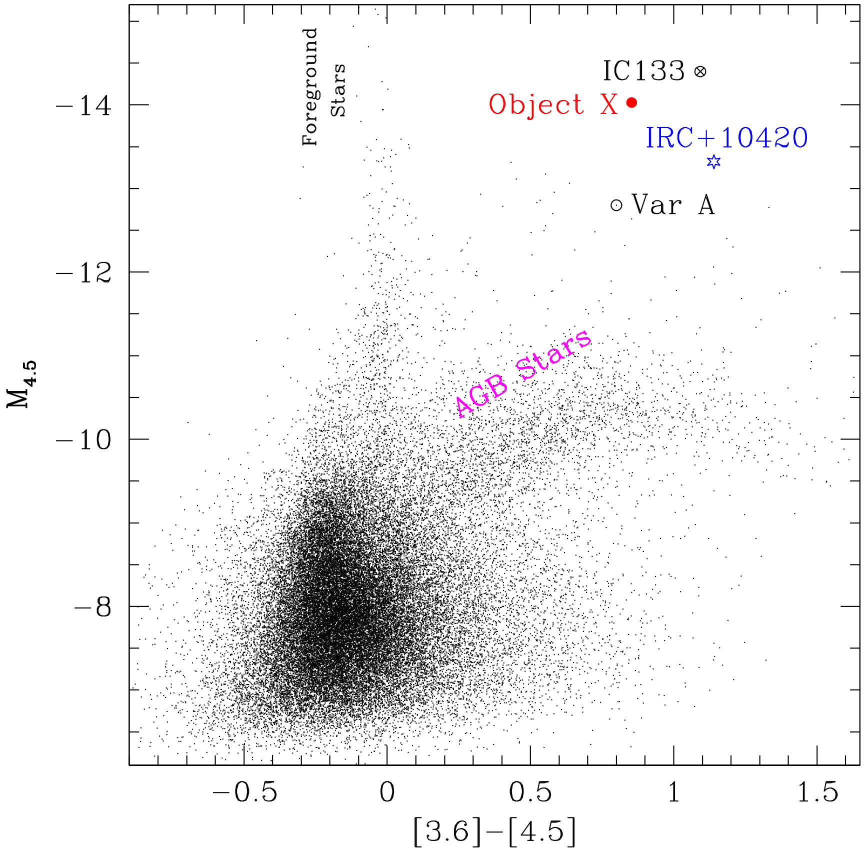

Fig. 3.1.— The 4.5 μm absolute magnitude vs. the [3.6] − [4.5] color mid-IR CMD of M33 adopted from Thompson et al. (2009a). Object X (red circle), the star cluster IC133 (cross and circle) and Var A (open circle around dots) are marked. For comparison, we also show the position of IRC+10420 (blue starred symbol) for a 5 kpc distance (Jones et al. 1993). The extremely bright stars near color ~ 0 are the foreground stars and the stars on the red branch at $M_{4.5} \simeq -10.5$ are M33 AGB stars. There are no other stars in M33 that are even remotely similar to Object X in these bands.

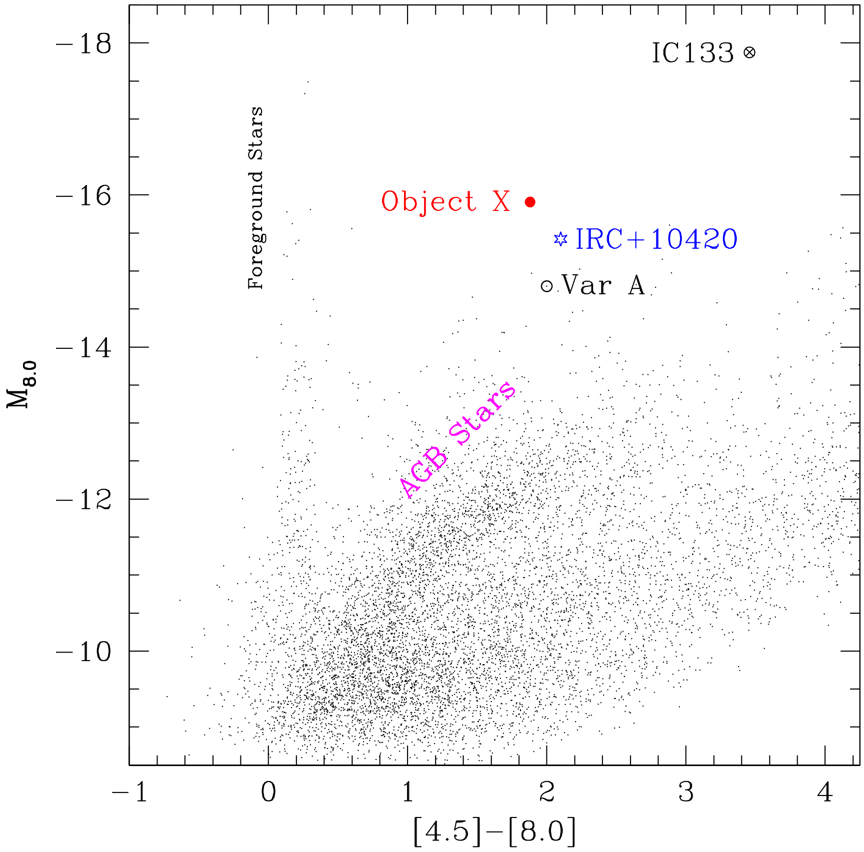

Fig. 3.2.— Same as Figure 3.1 but for 8.0 μm absolute magnitude vs. the $[4.5] - [8.0]$ color. Object X stands out in this combination of mid-IR bands as well.

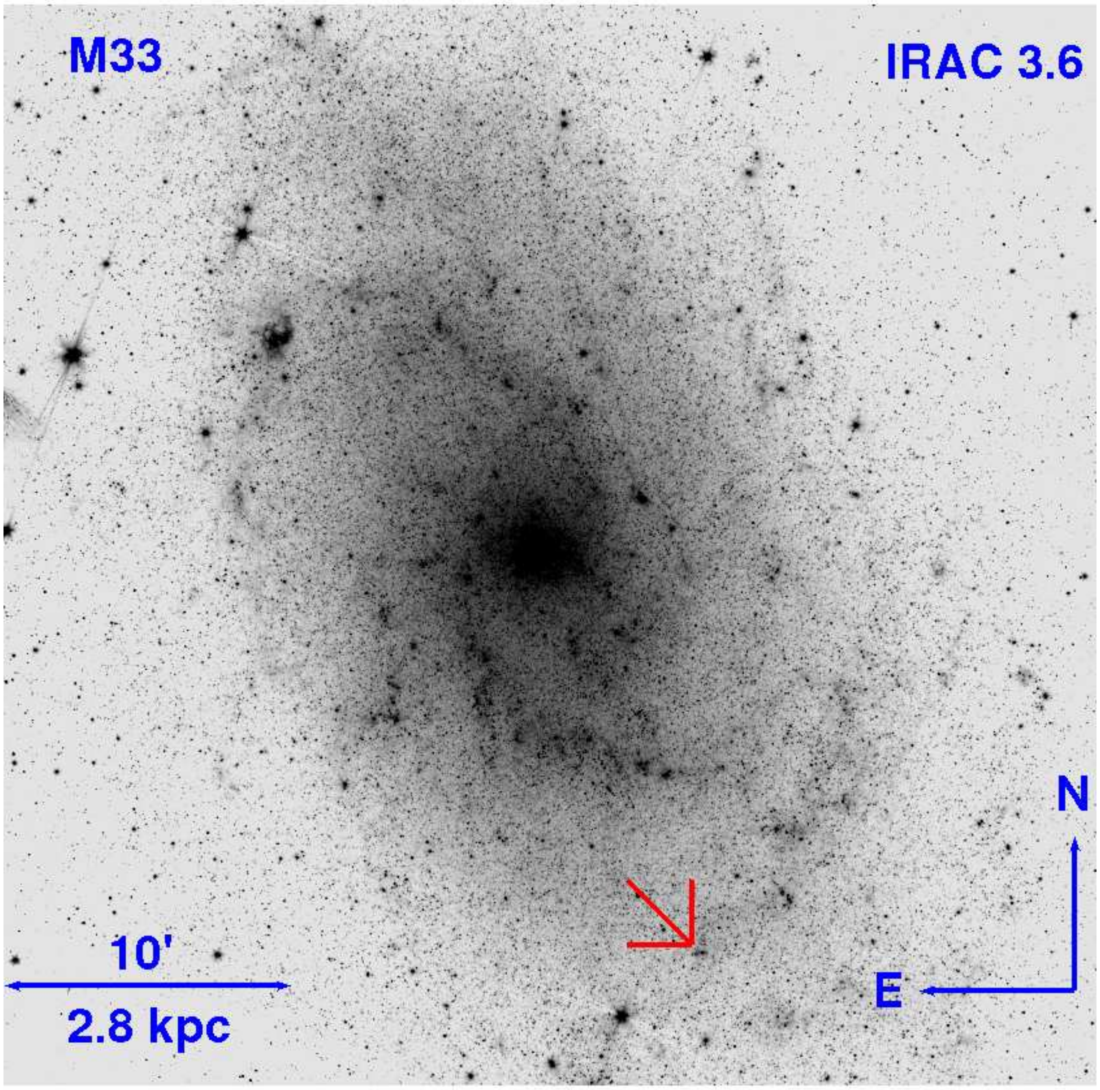

Fig. 3.3.— The IRAC 3.6 μm image of M33 showing the location of Object X (R.A. $= 1^h33^m24\overset{s}{.}1$, Dec. $= +30°25'34\overset{''}{.}8$; J2000.0) with an arrow.

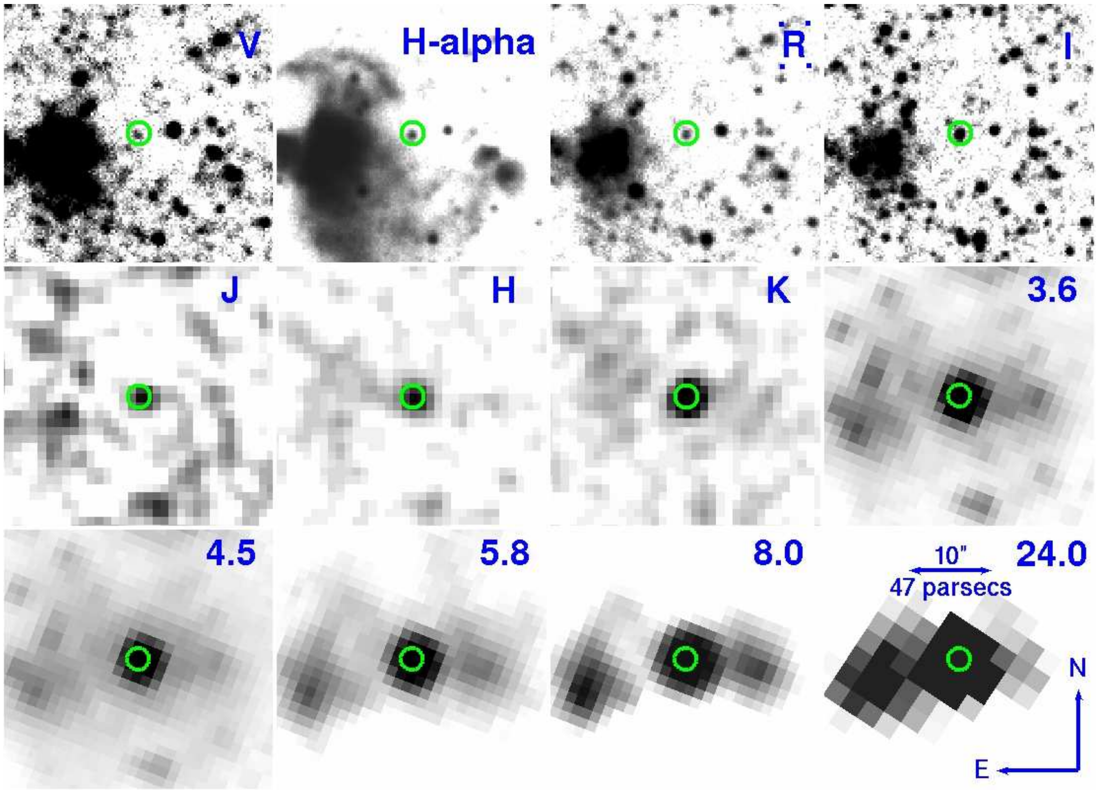

Fig. 3.4.— Multi-band images of the region around Object X (marked by the circles). The optical images were taken from the Local Group Survey (Massey et al. 2006), the near-IR images were taken from 2MASS (Skrutskie et al. 2006), the mid-IR images are from six co-added epochs of the data from McQuinn et al. (2007) as processed by Thompson et al. (2009a), and the MIPS 24 μm band image is from the *Spitzer* archive.

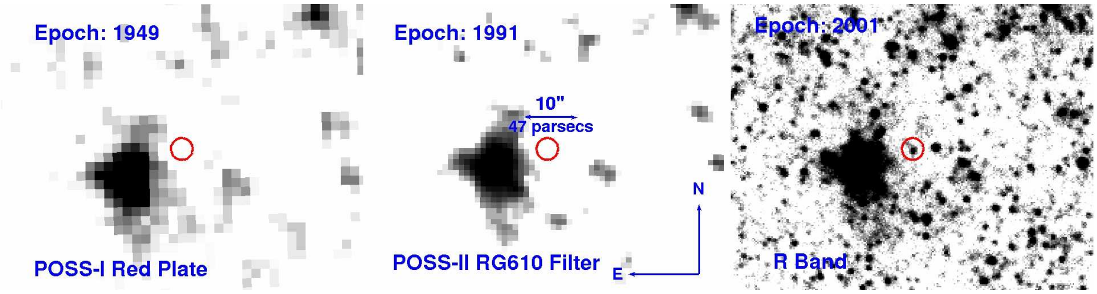

Fig. 3.5.— Historical images of the region near the location of Object X (marked by the circles) over the last ~ 60 years implying that Object X has remained obscured at least over this period of time.

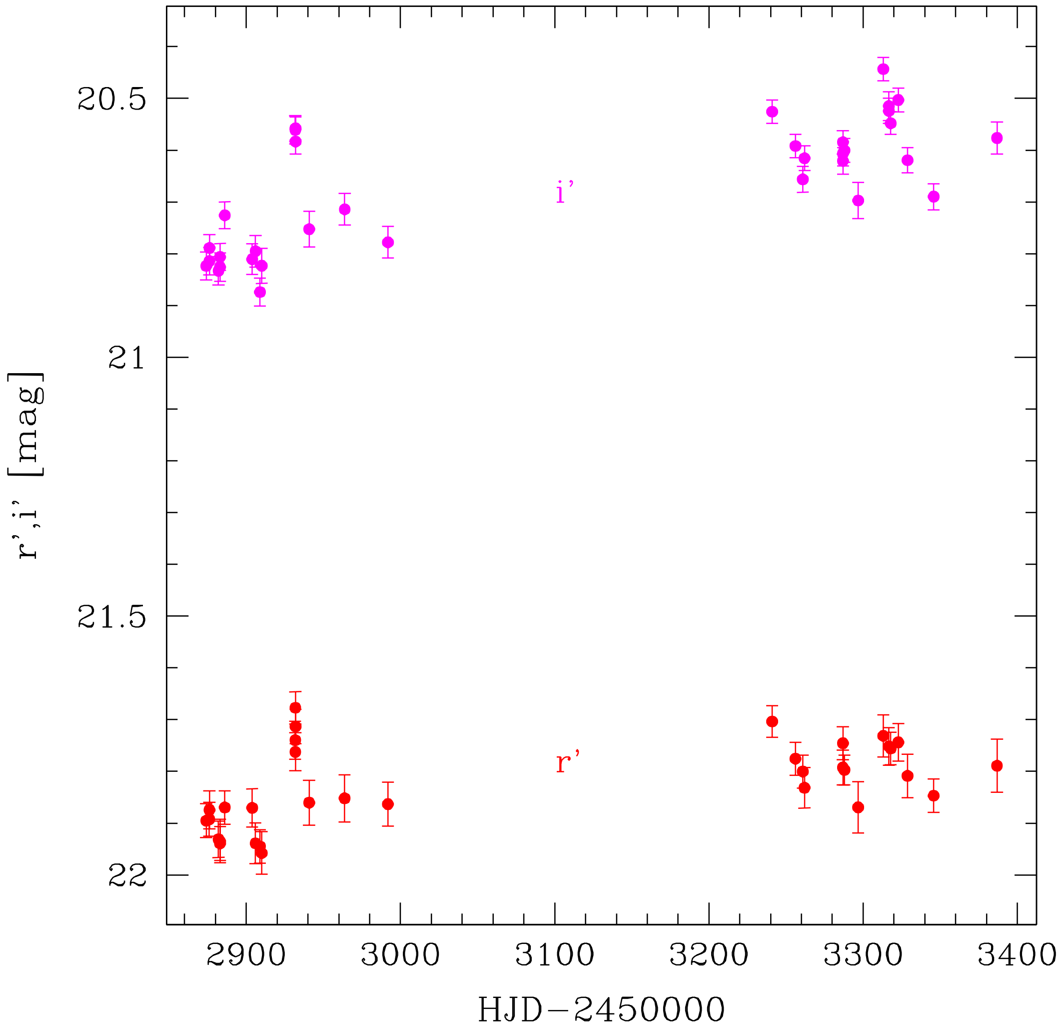

Fig. 3.6.— Optical variability of Object X in the *r'* and *i'* bands from Hartman et al. (2006). Object X shows correlated variability of about ∼0.4 magnitude (fractional variability of ∼45%) in both bands.

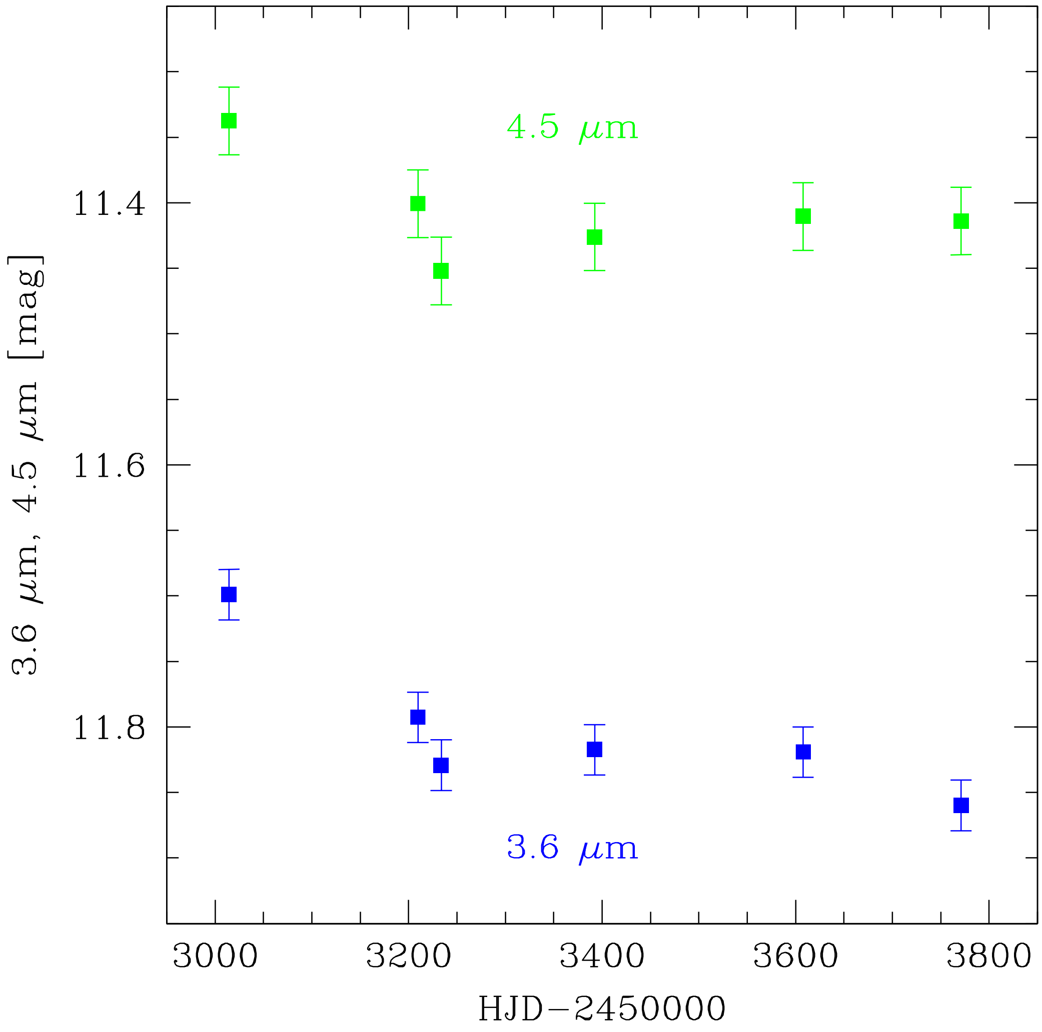

Fig. 3.7.— Mid-IR variability of Object X in the 3.6 μm and 4.5 μm IRAC bands. It shows correlated variability of about ∼0.15 magnitude (fractional variability of ∼15%) in both bands.

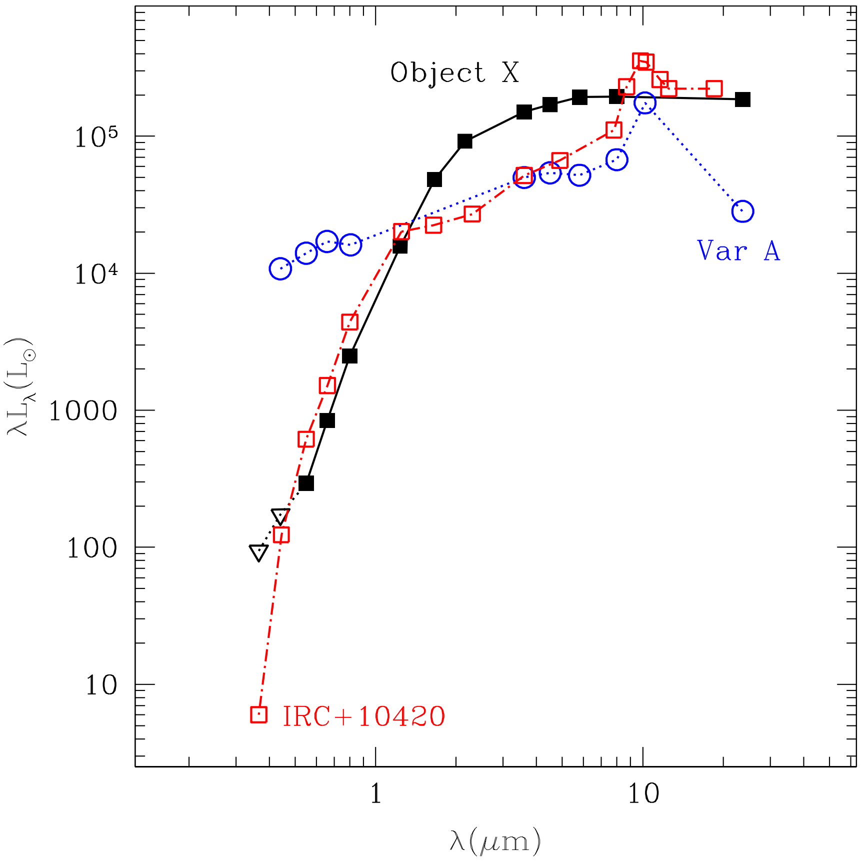

Fig. 3.8.— The SED of Object X as compared to that of IRC+10420 (Jones et al. 1993; Humphreys et al. 1997) and Var A (Humphreys et al. 2006). Both comparison SEDs have been constructed using data from multiple epochs (IRC+10420: *UB* from 1972, *VRI* from 1992, the rest from 1996; Var A: optical from 2000-01, near-IR from 1997, the rest from 2004-05) and these sources are known to be variable. We also note the large amount of extinction toward IRC+10420 ($A_V \simeq 6$, Jones et al. 1993). correcting for this extinction would make it more similar to Var A than Object X. However, it is uncertain how much of the extinguishing material is associated with that star rather than simply being along the line of sight, and therefore we do not correct for the extinction here.

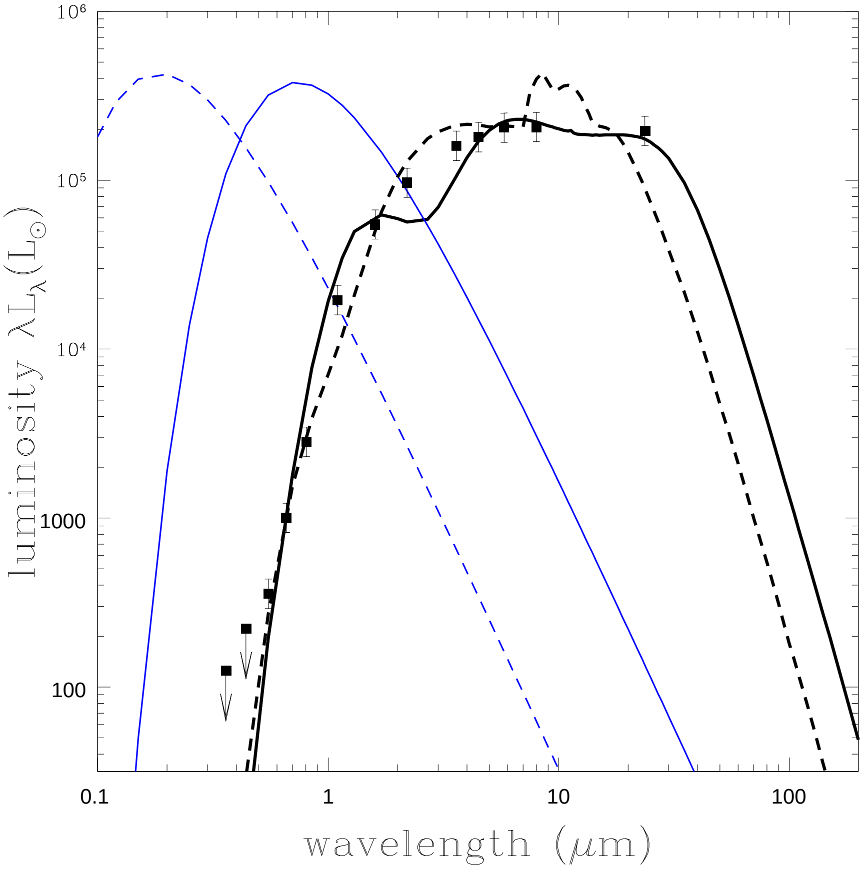

Fig. 3.9.— The results of DUSTY fits to Object X SED (black points). The heavier solid (dashed) lines show the model DUSTY SEDs for the source for graphitic (silicate) dusts. The lighter solid (dashed) lines show the black-body stellar SEDs. The graphitic model has $T_* = 5000$ K and $L_* = 10^{5.7} L_\odot$ with $\tau_V = 8.5$ and an inner edge dust temperature of 500 K corresponding to an inner shell radius of 2.6×10^{16} cm. The silicate model has $T_* = 20000$ K and $L_* = 10^{5.8} L_\odot$ with $\tau_V = 11.5$ and an inner edge dust temperature of 1200 K corresponding to an inner shell radius of 6.4×10^{15} cm. These models have a 2:1 ratio between their inner and outer radii, but the 4:1 and wind models (not shown) look very similar.

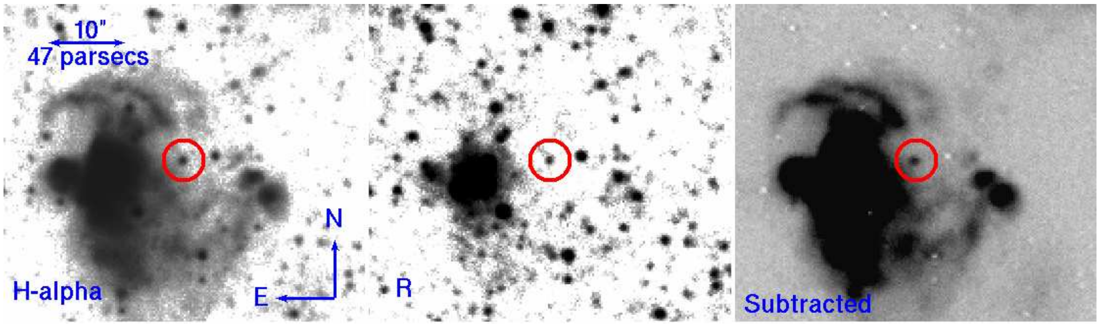

Fig. 3.10.— The Hα, R-band, and H$\alpha-$R subtracted images of the region near Object X. In the subtracted image, almost all the objects vanish, leaving behind the nearby H II region, Object X, and a small number of additional, mostly extended, Hα sources.

Band	Magnitude	Flux (mJy)	Luminosity ($\log(\lambda L_\lambda/L_\odot)$)	Year
U	$\gtrsim 24.1$	$\lesssim 4.20 \times 10^{-4}$	$\lesssim$1.98	2001
B	$\gtrsim 24.2$	$\lesssim 9.39 \times 10^{-4}$	$\lesssim$2.24	2001
V	23.15 ± 0.13	1.97×10^{-3}	2.467	2001
R	21.61 ± 0.04	6.83×10^{-3}	2.927	2001
I	19.99 ± 0.02	2.43×10^{-2}	3.395	2001
J	17.07 ± 0.17	2.37×10^{-1}	4.197	2001
H	15.04 ± 0.09	9.83×10^{-1}	4.684	2001
K_s	13.60 ± 0.04	2.42	4.963	2001
3.6 μm	11.57 ± 0.05	6.62	5.177	2004
4.5 μm	10.71 ± 0.05	9.34	5.230	2004
5.8 μm	9.81 ± 0.02	13.7	5.286	2004
8.0 μm	8.83 ± 0.01	19.1	5.290	2004
24.0 μm	$5.31 \pm \sim 0.1$	53.7	5.268	2005

Table 3.1: Photometry of Object X. For computing the luminosity we used a distance of 0.96 Mpc (Bonanos et al. 2006) and corrected for Galactic extinction of $E(B-V) = 0.049$ (Schlegel et al. 1998). The $UBVRI$ images are from Massey et al. (2006), the JHK_s photometry is from Cutri et al. (2003), the IRAC bands photometry is from Thompson et al. (2009a), and the MIPS 24 μm band image from the *Spitzer* archive (Program 5, PI:Gehrz).

Chapter 4: Finding η Car Analogs in Nearby Galaxies Using *Spitzer*

Note: This chapter is based on the paper "Finding η Car Analogs in Nearby Galaxies Using Spitzer: I. Candidate Selection", by R. Khan, K. Z. Stanek, and C. S. Kochanek, published in the Astrophysical Journal, 767:52, in April 2013 (Khan et al. 2013).

4.1. Introduction

Despite being very rare, massive stars such as luminous blue variable (LBVs), red super giants (RSGs), and Wolf-Rayet stars (WRs) play a pivotal role in enriching the interstellar medium (ISM) through mass loss (e.g., Maeder 1981). Understanding the evolution of these massive ($M \gtrsim 30\,M_\odot$) stars is challenging even when mass loss is restricted to continuous winds (e.g., Fullerton et al. 2006), but poorly understood impulsive mass ejections are probably an equally important, if not dominant mass loss mechanism (Humphreys & Davidson 1984; Smith & Owocki 2006; Kochanek 2011b). Mass loss also determines the structure of the star at death and hence the observed properties of the final core-collapse supernova (ccSN). In addition, there is also evidence that some supernova (SN) progenitors undergo major mass ejection events shortly before exploding (e.g., Gal-Yam et al. 2007; Smith 2008), further altering the properties of the explosion and implying a connection between some eruptive mass-loss events and death (Gal-Yam et al. 2007; Smith & McCray 2007; Kochanek 2011a; Chevalier & Irwin 2012). In two cases, eruptions were observed shortly before the ccSN: Type Ib SN 2006jc was spatially coincident with a bright optical transient that occurred in 2004 (Pastorello et al. 2007), and SN 2009ip underwent a series of outbursts in 2009, 2010, and 2011 before probably exploding as a Type IIn SN (see Mauerhan et al. 2013; Prieto et al. 2013; Pastorello et al. 2012). It is generally agreed that the effects of winds are metallicity dependent (Meynet et al. 1994; Heger et al. 2003) and the SNe requiring a dense circumstellar medium (the hyperluminous Type IIn) predominantly occur in lower metallicity galaxies (e.g., Stoll et al. 2011; Neill et al. 2011). This strongly suggests that the nature and distribution of stars undergoing impulsive mass loss will also be metallicity dependent and a full understanding requires exploring galaxies beyond the Milky Way.

Traditional studies of these massive stars search for them optically and then characterize them spectroscopically (e.g., Bonanos et al. 2009, 2010; Clark et al. 2012). This approach is not ideal for probing the episodes of major mass-loss because of dust formation in the ejecta. Dense winds tend to form dust, although for hot stars the wind must be dense enough to form a pseudo-photosphere in the wind (Davidson 1987) that shields the dust formation region from the UV emission of the star (Kochanek 2011b). The star will then be heavily obscured by dust for an extended period after the eruption (see, e.g., Humphreys & Davidson 1994). The Great Eruption of η Car between 1840 and 1860 is the most famous case of a stellar outburst. After the transient peak, the star faded optically and, aside from a brief brightening in $\sim$ 1890, remained fainter until $\sim$ 1950 when it began to optically brighten (see, e.g., Humphreys et al. 2012). The $\sim 10 M_{\odot}$ ejecta are now seen as a dusty nebula around the star absorbing and then reradiating $\sim$ 90% of the light in the mid-IR. This means that dusty ejecta are a powerful and long-lived signature of eruption. The emission from these dusty envelopes peaks in the mid-IR with a characteristic red color and a rising or flat spectral energy distribution (SED) in the *Spitzer* IRAC (Fazio et al. 2004) bands.

In the Galaxy, stars with resolved shells of dust emission are easily found at $24\,\mu$m (Wachter et al. 2010; Gvaramadze et al. 2010). The advantage of the $24\,\mu$m band is that it can be used to identify dusty ejecta up to $10^3 - 10^4$ years after formation. A minority of these objects are very luminous stars ($L \gtrsim 10^{5.5}$ $L_\odot$) with massive ($\sim 0.1 - 10$ $M_\odot$) shells (see summaries by Humphreys & Davidson 1994; Humphreys et al. 1999; Smith & Owocki 2006; Smith et al. 2009b; Vink 2012). These include AG Car (Voors et al. 2000), the Pistol Star (Figer et al. 1999), G79.29+0.46 (Higgs et al. 1994), Wray 17−96 (Egan et al. 2002), and IRAS 18576+0341 (Ueta et al. 2001). These systems are far older ($10^3 - 10^4$ years) than η Car, which makes it difficult to use the ejecta to probe the rate or mechanism of mass-loss. Still, the abundance of Galactic shells implies that the rate of η Car-like eruptions is on the order of a modest fraction of the ccSN rate (Kochanek 2011b). Their emission peaks in the shorter IRAC bands when they are relatively young ($\sim 10 - 100$ years) because, as the ejected material expands, the dust becomes cooler and the emission shifts to longer wavelengths (Kochanek et al. 2012a). It is difficult to quantify searches for such objects in our Galaxy as it is difficult to determine the distances to the sources and the survey volume because we have to look through the crowded and dusty disk of the Galaxy. Surveys of nearby galaxies are both better defined and build larger samples of younger systems whose evolution can be studied to better understand the mechanism.

With *Spitzer* it is difficult to use the $24\,\mu$m observations that have proved so successful in the Galaxy because of the poor angular resolution. However, we have shown that such surveys can be done with IRAC (3.6–8.0 μm). In Thompson et al. (2009a) and Khan et al. (2010b), we characterized the extreme AGB star populations that appear to be the progenitors of the SN 2008S-like transients (Prieto et al. 2008; Prieto 2008) using archival IRAC images of nearby galaxies. Gerke & Kochanek (2013) characterized the integrated contribution of these populations to explore their effeccts on integrated SEDs given the issues raised by Maraston et al. (2006), Conroy et al. (2009, 2010b), and Conroy & Gunn (2010). These studies empirically confirmed that these $\sim 10^{4.5}\,\mathrm{L}_\odot$ dusty stars are rare but are also relatively easy to identify in IRAC images despite the modest angular resolution. Next, we examined all the other bright, red mid-IR sources in M 33, and in Khan et al. (2011) we discovered Object X, the brightest mid-IR star in M 33. Object X is a $\mathrm{L}_{bol} \sim 5 \times 10^5\,\mathrm{L}_\odot$, $\mathrm{M} \gtrsim 30 M_\odot$ evolved star obscured by dust formed during mass loss events over the last ∼ century. Its properties are similar to those of the Galactic OH/IR star IRC+10420 (Humphreys et al. 1997; Blöcker et al. 1999; Humphreys et al. 2002), which has a complex dusty circumstellar structure resulting from episodic, low-velocity mass ejections. We proposed that Object X may emerge from its current ultra-short evolutionary phase as a hotter post-RSG star analogous to M 33 Var A (Hubble & Sandage 1953; Humphreys et al. 1987, 2006).

While Object X is intriguing, it likely underwent a period of enhanced, but relatively steady, mass loss from the parent star rather than the short transient episode of mass loss usually associated with so called "supernova impostors" (Van Dyk et al. 2000; van Dyk & Matheson 2012). It is also an order of magnitude less luminous and several times less massive than η Car, one of the most luminous ($L_{bol} \sim 5 \times 10^6\,\mathrm{L}_\odot$) and massive ($M \simeq 100 - 150 M_\odot$) stars known (Humphreys & Davidson 1994). No true analog of η Car in mass, luminosity, energetics, mass lost and age has been found (see Smith et al. 2011; Kochanek et al. 2012a). Quantifying the population of η Car analogs, or their rarity, in the local universe will allow us to investigate the rate of giant eruptions of the most massive stars. It may also help us answer open questions about the evolution of massive stars such as: (1) the frequency of major mass ejection events, (2) the number of events per star, (3) whether the frequency depends on the metallicity or other stellar properties, and (4) whether there is really any relation between mass ejections and the so called "supernova impostors" (see Smith et al. 2011; Kochanek et al. 2012a).

Here we carry out a pilot study of 7 nearby galaxies within ($\lesssim 4\,$Mpc) to search for analogs of $\eta\,$Car. We concentrate on galaxies with recent star formation, as only these will have large numbers of the short-lived, very massive stars that we want to study, but we also include one small, low-mass galaxy (NGC 6822) as a test case (see Table 4.1). Section 4.2 describes our methodology for identifying potential $\eta\,$Car analogs in nearby galaxies using archival *Spitzer* data and sources of contamination. Section 4.3 discusses the nature of the candidates, although a detailed study is deferred to Chapter 5. Section 4.4 shows how our search method allows us to quantify the selection criteria and to set an interesting limit on the rate of events similar to the Great Eruption of $\eta\,$Car in the local universe even before we have enter Chapter 5. Finally, in Section 4.5 we outline the future of our approach.

4.2. A Search for $\eta\,$Car Analogs

In this section, we present the methodology of our search for $\eta\,$Car analogs. First we discuss our data sources and the properties of the targeted galaxies. Next we describe the photometry and candidate selection procedures. Then we consider contamination due to non-stellar sources. Finally we consider whether an $\eta\,$Car analog in a nearby galaxy could be hidden in a compact stellar cluster.

4.2.1. Targeted Galaxies

There are a number of sources of archival *Spitzer* data for nearby galaxies. In the Local Group, SAGE (Surveying the Agents of a Galaxy's Evolution) and SAGE-SMC (Meixner et al. 2006; Gordon et al. 2007) surveyed the LMC and SMC. Barmby et al. (2006) surveyed M 31 with first results for massive stars discussed by Mould et al. (2008). M 33 was observed at several epochs which allowed for mid-IR variability studies of M 33 stars (McQuinn et al. 2007; Thompson et al. 2009a). The *Spitzer* Infrared Nearby Galaxies Survey (SINGS, Kennicutt et al. 2003) made a comprehensive mid-IR imaging and spectroscopic survey of 75 galaxies, many of them within 10 Mpc. The Local Volume Legacy Survey (LVL, Dale et al. 2009) surveyed a total of 256 nearby galaxies, including all known galaxies inside a sub-volume bounded by 3.5 Mpc and an unbiased sample of S-Irr galaxies within a larger, and more representative, 11 Mpc sphere. The ongoing Spitzer Survey of Stellar Structure in Galaxies (S^4G, Sheth et al. 2008) is collecting data for ~ 2300 galaxies within 40 Mpc using the warm *Spitzer* (3.6 and 4.5μm) bands.

For this chapter, we selected 7 galaxies spanning a range of mass, morphology, distance, and star formation history. Since this is a pilot study, the sample is deliberately eclectic rather than focused on a sample maximizing the star formation rate per galaxy. Ultimately we would like to examine all nearby galaxies rather than just a few. Table 4.1 summarizes the properties of the targeted galaxies. The absolute magnitude M_B and Hα luminosity L(Hα) are from Kennicutt et al. (2008), and L(Hα) is converted to star formation rate (SFR) following Equation 2 of Kennicutt (1998). The foreground Galactic extinctions are from Schlafly & Finkbeiner (2011). The targeted galaxies have an integrated SFR of ~ 2 M$_\odot$ year^{-1}. For the assumed Salpeter IMF of Kennicutt (1998), we can convert this into a massive ($M > 8$ M$_\odot$) star formation rate of $\sim 0.014\,\text{year}^{-1}$. The observed ccSN rate over that 20 years is

$\sim 0.15\,\mathrm{year}^{-1}$ ($0.05 < R_{SN} < 0.35\,\mathrm{year}^{-1}$, at 90% confidence). Since the ccSN rate should agree with the massive-star formation rate, this is a significant discrepancy for which we have no obvious explanation, and such mismatches are also found in other contexts (e.g., Horiuchi et al. 2011).

The nearest of our targeted galaxies, NGC 6822 ($\mathrm{D} \simeq 0.46$ Mpc, Gieren et al. 2006), is a barred irregular galaxy (de Vaucouleurs et al. 1991). We included this small galaxy in our sample as an interesting nearby test case for examining large numbers of smaller, lower metallicity systems. M 33 ($\mathrm{D} \simeq 0.96$ Mpc, Bonanos et al. 2006) was previously studied by both Thompson et al. (2009a) and Khan et al. (2010b) to search for dusty stars that are much redder but less luminous than the stars we are searching for in this chapter. NGC 300 ($\mathrm{D} \simeq 1.9$ Mpc, Gieren et al. 2005) and M 81 ($\mathrm{D} \simeq 3.6$ Mpc, Gerke et al. 2011) were also studied by Khan et al. (2010b). NGC 2403 ($\mathrm{D} \simeq 3.1$ Mpc, Saha et al. 2006) contains two sources sometimes classified as SN impostors, SN 1954J and SN 2002kg (see the review by van Dyk & Matheson 2012), but any star associated with SN 1954J must be relatively low mass ($\sim 20\,\mathrm{M}_\odot$ rather than $\gtrsim 50\,\mathrm{M}_\odot$) and shows no strong evidence for mid-IR emission (Kochanek et al. 2012a), while SN 2002kg is an LBV/S Dor variable star in NGC 2403 (V37, van Dyk 2005; Weis & Bomans 2005) with little mass loss (Kochanek et al. 2012a). Unlike the other large galaxies we studied, NGC 247 ($\mathrm{D} \simeq 3.6$ Mpc, Madore et al. 2009) is highly inclined. NGC 7793 ($\mathrm{D} \simeq 4.1$ Mpc, Tully et al. 2009) is the most distant galaxy studied.

For M 33, we used the six co-added epochs of IRAC data from McQuinn et al. (2007) that were used by Thompson et al. (2009a) and Khan et al. (2010b), and the MIPS data retrieved from the *Spitzer Heritage Archive*. For NGC 300 and NGC 247, we used the data from the LVL survey (Dale et al. 2009). For NGC 6822, NGC 2403, M 81, and NGC 7793, we used the data from the SINGS survey (Kennicutt et al.

2003). We utilize the full mosaics available for each galaxy. Table 4.2 shows the different pixel scales of the images retrieved from the *Spitzer* archive for M 33, and those provided by the SINGS and LVL surveys for the other six galaxies.

4.2.2. Candidate Selection

The SED of a hot dust-obscured star will generally have two peaks — a dust obscured optical peak, which could be absent altogether given enough absorption, and a mid-IR peak whose location in wavelength depends on the radius of the dust shell around the star. In the IRAC bands, the SED will be flat or rising towards longer wavelengths. For example, η Car has a steeply rising SED towards longer mid-IR wavelengths (e.g., Robinson et al. 1973) and the luminosity of the star exceeds 10^5 $L_\odot$ in each IRAC band (see Figure 4.1). At extra-Galactic distances, an η Car analog would appear as a bright, red point source in IRAC images with a relatively fainter optical counterpart due to the self-obscuration.

We used the Daophot/Allstar PSF-fitting and photometry package (Stetson 1992) to identify point sources in all four IRAC bands and then performed photometry at the source location using both aperture and PSF photometry. We used the IRAF[1] ApPhot/Phot tool for the aperture photometry. The aperture fluxes were transformed to Vega-calibrated magnitudes following the procedures described in the *Spitzer* Data Analysis Cookbook[2] and aperture corrections of 1.213, 1.234, 1.379, and 1.584 for the four IRAC bands. The choice of extraction aperture (R_{ap}) as well as the inner (R_{in}) and outer (R_{out}) radii of the local background annulus are reported in Table 4.2. We estimate the local background using a 2σ outlier

---

[1] IRAF is distributed by the National Optical Astronomy Observatory, which is operated by the Association of Universities for Research in Astronomy (AURA) under cooperative agreement with the National Science Foundation.

[2] http://irsa.ipac.caltech.edu/data/SPITZER/docs/dataanalysistools/

rejection procedure in order to exclude sources located in the local sky annulus, and correct for the excluded pixels assuming a Gaussian background distribution. Using a background annulus immediately next to the signal aperture minimizes the effects of background variation in the crowded fields of the galaxies. We used the Daophot/Allstar package for PSF photometry. The PSF photometry fluxes were transformed to Vega-calibrated magnitudes by applying zero point offsets determined from the difference between the calibrated aperture magnitudes and the initial PSF magnitude estimates of the bright stars in each galaxy.

For the 3.6 and 4.5μm bands, after verifying consistency with the aperture magnitudes, we only use the Vega-calibrated PSF magnitudes. For $5.8\,\mu$m, we switch to aperture magnitudes when Allstar fails to fit the PSF to a point source at the location identified by Daophot due to the decreasing resolution. PSF photometry performs very poorly at $8.0\,\mu$m, leading to both inaccurate photometry and many false sources because Daophot frequently splits up extended regions of PAH emission into spurious point sources. Thus, at $8.0\,\mu$m we only use aperture photometry at positions determined for sources identified in the other three bands. We do not use this band for building our initial source list.

We define our initial source list as all point sources that have $\lambda L_\lambda > 10^4\,\mathrm{L}_\odot$ in any one of the 3.6, 4.5, and $5.8\,\mu$m bands, excluding regions near saturated stars and, in the case of M 81, the high surface brightness core of the galaxy. We identify sources in each of these three bands, and cross-match the catalogs using a 1 pixel matching radius. We then adopt the position determined at the shortest wavelength (highest resolution) with a $> 3\sigma$ detection, and we use this position for the $8.0\,\mu$m aperture photometry. We fit the mid-IR SED of each object as a power law in wavelength

$$\log_{10}(\lambda L_\lambda) = a \times \log_{10}(\lambda) + b \tag{4.1}$$

to determine the slope (a, $\lambda L_\lambda \propto \lambda^a$) and intercept ($b$). We can crudely relate the slope (a) to a dust temperature as

$$a = -4 + \frac{\log_{10}\left(\frac{e^{\frac{hc}{\lambda_1 kT}}-1}{e^{\frac{hc}{\lambda_4 kT}}-1}\right)}{\log_{10}\left(\frac{\lambda_4}{\lambda_1}\right)}, \tag{4.2}$$

where λ_1 and λ_4 are the shortest and longest band-centers assuming a blackbody spectrum and ignoring Planck factors. We define the total mid-IR luminosity (L_{mIR}) as the trapezoid rule integral of L_λ across the band centers

$$L_{mIR} = \sum_{i=1}^{3} \frac{1}{2}\left(\lambda_{i+1} - \lambda_i\right)\left(L_{\lambda_i} + L_{\lambda_{i+1}}\right), \tag{4.3}$$

where λ_i = 3.6, 4.5, 5.8, and 8.0 μm. We also calculate the fraction f of L_{mIR} that is emitted in the first three IRAC bands. We define f as the ratio of the energy emitted between 3.6 and 5.8 μm (first two terms of the integral), to L_{mIR} (all three terms of the integral). The approximate values of L_{mIR}, a, and f for η Car are $10^{5.65}$ $L_\odot$, 2.56, and 0.32, and those for Object X are $10^{5.17}$ $L_\odot$, 0.22, 0.57.

We defined candidates as sources with mid-IR luminosity $L_{mIR} > 10^5$ $L_\odot$, a mid-IR SED slope $a > 0$, and $f > 0.3$. Figures 4.2 and 4.3 show the distribution of point sources in M 81 with $\lambda L_\lambda > 10^4\,L_\odot$ in at least one of the 3.6, 4.5, and 5.8 μm IRAC bands as a function of L_{mIR}, a, and f. The open red triangles in these figures correspond to candidates that are known to be non-stellar in nature (see

Section 4.2.3), and the solid red triangles represent the surviving candidates. While a few hundred sources in M 81 are bright enough in the mid-IR to be included in these figures, only a handful of these even remotely resemble η Car, and not a single one of them is as luminous and as red (cold) as η Car. The other targeted galaxies show similar distributions of sources. These distributions illustrate that our selection criteria for identifying potential η Car analogs are robust and allows for selecting objects that are significantly less luminous in the mid-IR and have much warmer circumstellar dust than η Car. Table 4.5 reports the survey area and the number of candidates found for each galaxy.

We used aperture photometry to estimate the MIPS 24, 70, and 160 μm band luminosities of the objects that meet our selection criteria. For point sources that do not have a flux that is $\gtrsim 3\sigma$ above the local sky, we determine the 3σ detection limit for each aperture location using the local background estimate. Due to the poor spatial resolution of these bands, which forces us to choose increasingly large apertures at longer wavelengths (see Table 4.2), these measurements have limited utility. Figure 4.5 shows the mid-IR SEDs of the candidates we identified in M 33 along with normal stars in the M 33 image selected from top left region of Figure 4.5. At 24 μm, the SEDs of the normal stars show the expected slope for the Rayleigh-Jeans tail of their SEDs, followed by an unphysical rise at 70 and 160 μm. Essentially, due to the poor resolution, the apertures used for these two bands include many objects other than the intended target, and even normal stars appear to have rising far-IR SEDs. This means that we can generally use the 24 μm fluxes while the 70 and 160 μm measurements should be treated as upper limits regardless of their origin. Nevertheless, the MIPS bands are useful as a qualitative constraint on an object's physical nature (i.e. if it is a galaxy, QSO, star, cluster etc.).

4.2.3. Sources of Contamination

While our selection criteria are designed to identify dust obscured individual stars, there are several classes of contaminating sources as well. QSOs have red mid-IR SEDs compared to stars (e.g., Stern et al. 2005), as do star forming galaxies with strong PAH emission at 8.0 μm (e.g. the SED models in Assef et al. 2010). Sources in the galaxies such as dusty star clusters and H II regions can also appear as candidates. We used the SIMBAD[3] and VizieR[4] services to search for previous classifications and near-IR counterparts from the 2MASS point source catalog (Cutri et al. 2003). We also noted other significant pieces of information, such as a candidate location coinciding with known radio and X-ray sources. For example, many of the candidates in M 33 are associated with known supernova remnants (SNRs). We reject a source as "non-stellar" if it is a galaxy or QSO with a measured redshift or if archival images clearly show that it is a galaxy. The rejected sources that meet our selection criteria are described in Section 4.3.1.

We estimate the expected number of extragalactic contaminants for each galaxy using the SDWFS survey (Ashby et al. 2009) where the nature of the sources, particularly AGNs, is also well understood from the AGES redshift survey (Kochanek et al. 2012c). We transform the apparent magnitudes of all sources in a 6 $\deg^2$ region of SDWFS to luminosity using each target galaxy's distance modulus, determine how many of them would meet our selection criteria, and correct that count for our survey area around each galaxy. Table 4.3 reports the expected surface density of extragalactic contaminants and the number expected given the survey area around each galaxy. We expect a total of ~ 41 extragalactic sources to pass our selection criteria across the targeted galaxies, as compared to 46 initial candidates. Figure 4.4,

---

[3] http://simbad.u-strasbg.fr/

[4] http://vizier.u-strasbg.fr/

which has the same format as Figure 4.2, illustrates this for M 81's distance. In the $6\,\mathrm{deg}^2$ SDWFS area, 449 ($\sim 75\,\mathrm{deg}^{-2}$) sources pass our selection criteria, indicating that we should expect ~ 13 background sources meeting our selection criteria given our $0.17\,\mathrm{deg}^2$ survey region around M 81, as compared to the 14 initial candidates selected. Indeed, as we discuss in Section 2.4, we can already identify 11 of the 46 initial candidates as extragalactic. Statistically, this means that only 6 ± 6 of our initial candidates are likely associated with the galaxies. Also note in Figure 4.4 that none of the contaminating background sources have properties directly comparable to η Car. The expected numbers of contaminating sources are generally consistent with the observed numbers with the exception of NGC 247, which we investigated but appears to be a statistical fluke. The angular distribution of the candidates relative to the galaxies is also strongly suggestive of a dominant contribution for background sources.

Many of the candidate SEDs show a "dip" from $3.6\,\mu$m to $4.5\,\mu$m before rising again at $5.8\,\mu$m (see Figure 4.5). This is a common feature of massive star-forming regions and star clusters (e.g., Churchwell et al. 2006) created by strong stochastic emission from polycyclic aromatic hydrocarbon (PAH) molecules (Whelan et al. 2011) excited by UV radiation from O and B stars (see Wood et al. 2008 for a detailed treatment of this topic). In total galaxy spectra, this is a weaker effect and the dominant PAH emission feature is at 8μm and comes more from the diffuse ISM rather than individual stars or clusters. The SEDs of η Car and Object X do not show this dip at $4.5\,\mu$m. We treat the presence of this dip as a qualitative indicator that the source may be a cluster or lie in a cluster. Deep *Hubble Space Telescope* (*HST*) images of these regions, where available, can help us distinguish single bright red stars from clusters of fainter stars that may be merged into a single bright source in the lower resolution *Spitzer* images. Whether these clusters can potentially hide η Car analogs is discussed in Section 4.2.4.

In Figure 4.7, we present SEDs of four different types of objects that met our selection criteria — a likely dusty star in NGC 2403, a star-cluster in M 33, a QSO behind M 81, and a galaxy behind NGC 7793. Although all four objects met our selection criteria, the detailed shapes of their SEDs are very different from each other. The likely stellar source, N 2403-3, has a very steeply rising mid-IR SED that peaks between 8 μm and 24 μm. While the compact cluster (M 33-8) SED looks quite similar to that of η Car in the IRAC bands, it continues to rise steeply up to 24 μm, and the MIPS 70 μm and 160 μm upper limits show that it peaked between 24 μm and 70 μm. The SED of the QSO (M 81-4) remains relatively flat from 3.6 μm to 24 μm. The MIPS 70 μm and 160 μm upper limits for N 7793-2 (a galaxy) are quite stringent, because the source is far from the center of the galaxy, and would rule out an η Car analog model. For some cases, such as N 7793-2, HST images clearly determine the nature of the source (Figure 4.10, bottom panel).

4.2.4. Star Clusters

One concern with star clusters as a source of contamination is the possibility of “hiding” a luminous dusty star in a dusty star cluster. To explore this problem we estimated what the SED of the star cluster containing η Car would look like if it were located in one of the targeted galaxies. We combined the SED of η Car from Humphreys & Davidson (1994) with the SED of the Carina nebula from Smith & Brooks (2007) to produce an SED of the entire complex (Figure 4.6). The combined SED is clearly a multi-component SED, which is not typical of our candidates. Moreover, the Carina nebula is roughly $\sim 2.5^\circ$ in extent (Smith & Brooks 2007), which at the distance of M 33 becomes $\sim 20.''$ and would be easily resolved by IRAC.

Even at the distance of NGC 7793 it would still subtend $\sim 5''$ and be resolved. At all these distances it would be very easily resolved by HST or JWST (Gardner et al. 2006).

In Figures 4.2 and 4.3, we show the mid-IR luminosity L_{mIR}, SED slope a, and fraction f of η Car ("η"), the Carina nebula excluding η Car ("$\eta-$"), and the entire complex including η Car ("$\eta+$"). It is apparent from these figures that even if the Carina nebula was not resolved: (1) we would select analogs of η Car and unresolved dusty stellar complexes hosting such analogs, (2) while it is close, we would not select a stellar complex that is identical to the Carina nebula excluding η Car, and (3) there are no sources with L_{mIR}, a, and f comparable to η Car in M 81. Indeed, this last point is true for each galaxy we studied.

There are, however, far more compact star clusters among the candidates such as M 33-5, M 33-8 and M 81-10 (see Section 4.3) where HST images are required to recognize their spatial extent. Even in these cases it is unlikely we would lose a candidate. First, it would require a "conspiracy" of a sort, namely that the SED of the hotter circumstellar dust around the star (with characteristic $T \sim 400\,\mathrm{K}$ and $L_{bol} \sim few \times 10^6\,L_\odot$) seamlessly merges with the colder SED of the interstellar dust (with characteristic $T \sim 100\,\mathrm{K}$ and $L_{bol} \sim 10^7\,L_\odot$) in the cluster. Typically we find that this leads to SEDs with "bumps" which we do not observe.

Possibly more constraining is the requirement that for a compact cluster to hide an η Car analog it must still contain large amounts of interstellar gas and dust several million years after the cluster formed to allow for the time that even the most massive stars require to evolve away from the main sequence. However, a cluster sufficiently luminous to hide an η Car analog must host many luminous stars with strong UV radiation fields and winds, which will likely clear the cluster of gas and dust needed to produce strong mid-IR emission. For example, 30 Dor, which harbors stars possibly as massive as $300\,M_\odot$ and is about 1.5×10^6 years old (e.g., Crowther et al. 2010), is a weak source of $8\,\mu$m emission (see, e.g., Figure 1 of Zhang & Stanek 2012).

4.3. Inventory of Candidates

In this section we discuss the initial results of our search for η Car analogs. A total of 46 sources passed our basic mid-IR selection criteria ($L_{mIR} > 10^5$ L$_\odot$, $a > 0$, $f > 0.3$). First we discuss the eleven candidates that can be rejected as known non-stellar sources. Their properties are reported in Table 4.4. Then we list the remaining 35 candidates, including Object X, in Table 4.5. Table 4.6 presents the near-IR photometry for the 9 sources with counterparts in the 2MASS point-source catalog (Cutri et al. 2003).

4.3.1. Rejected Candidates

Of the 11 rejected candidates, six are AGNs or galaxies with a redshift measurement. Four have been photometrically classified as galaxies by the SDSS survey (Abazajian et al. 2009) and visual inspections of the SDSS images find diffuse extended sources consistent with this classification. One of these sources is also $0\farcs4$ away from a radio and X-ray source and is likely a low redshift AGN. One candidate is a well-resolved galaxy in HST images. The SEDs of the rejected candidates are shown in Figure 4.8 and their luminosities, SED slope, and f are listed in Table 4.4. In detail, we find that:

- *M 81-1* is an AGN. It is $0\farcs36$ from a quasar at $z = 0.605$ (Richards et al. 2009).

- *M81-2* is an AGN. It lies 0.″4 from a radio and X-ray source (Flesch 2010) and is classified as a galaxy by SDSS (Abazajian et al. 2009). Visual inspection of the SDSS image also shows an extended source consistent with this classification.

- *M81-3* is an AGN. It is 0.″38 from a quasar at $z = 1.29683$ (Schneider et al. 2010).

- *M81-4* is an AGN. It is 0.″65 from a quasar at $z = 1.97519$ (Schneider et al. 2010).

- *M81-8*, *M81-9*, and *M81-13* are classified as galaxies by SDSS (Abazajian et al. 2009) and visual inspections of the SDSS images finds extended sources consistent with these classifications.

- *N247-2* is a galaxy at $z = 0.02089$ (Jones et al. 2009).

- *N7793-2* is unambiguously a galaxy in HST images (Figure 4.10, bottom panel).

- *N7793-5* is a galaxy at $z = 0.0614$ (Jones et al. 2009).

- *N7793-7* is an AGN. It is 1.″5 from a QSO at $z = 0.071$ (Véron-Cetty & Véron 2010).

While the astrometric matches are sometimes imperfect, we are dealing with objects with such low surface densities that a mismatch is extraordinarily unlikely. Essentially, this search recapitulates aspects of the Kozłowski et al. (2010) search for quasars behind the Magellanic clouds as red mid-IR sources following the extragalactic mid-IR search criteria of Stern et al. (2005). The red mid-IR colors created by the power-law SEDs of quasars mimic aspects of the red SEDs of dusty stars.

4.3.2. Remaining Candidates

The mid-IR luminosities, slopes, and the fractions f of the 35 remaining candidates, including Object X, are presented in Table 4.5. Of these, 9 also have 2MASS photometry and their near-IR magnitudes are presented in Table 4.6 along with the $UBVRI$ magnitudes of the closest optical counterparts for the three candidates in M 33 for which there is a publicly available catalog (Massey et al. 2007). We select Object X (Khan et al. 2011) as a candidate (M 33-1) but not M 33 Var A (Hubble & Sandage 1953; Humphreys et al. 2006). Although both are dust obscured stars with comparable bolometric luminosities and exist in our initial source list, it is apparent from Figure 4.1 that in the IRAC bands Object X is much more luminous ($\sim 1.5 \times 10^5\,\mathrm{L}_\odot$) than M 33 Var A ($\sim 0.5 \times 10^5\,\mathrm{L}_\odot$). M 33 Var A appears to be entering a phase of reduced mass loss rate and lower dust optical depths (Humphreys et al. 2006) causing it to drop out of our selection criteria. Based on the SEDs shown in Humphreys et al. (2006), it likely would have met out selection criteria in previous decades, illustrating the time dependent nature of this search method. While we could broaden our search criteria to include it, we presently want to both focus on more luminous stars and avoid a large increase in the number of candidates for follow-up studies.

It is apparent from the SEDs of the candidates (Figure 4.9) that few have mid-IR luminosities comparable to η Car. Moreover, the SEDs of many sources, such as N 2403-2, N 247-3 and N 7793-10, appear so dissimilar from the SEDs of η Car and Object X that they seem unlikely to be stellar sources. The MIPS band luminosity limits are also useful here. For example, the relatively low MIPS 70 and 160 μm luminosity limits indicate that N 247-1 must have a very flat or falling SED at these redder wavelengths and is probably an AGN, which is also suggested by its distance from the galaxy.

On the other hand, the SEDs of M 33-5, M 33-8 and M 81-10 are similar to η Car while N 300-1, M 81-5, M 81-6 and M 81-7 are similar to Object X (M 33-1). HST images show that M 33-5, M 33-8, and M 81-10 are compact star clusters (Figure 4.10, top three panels). M 81-5 is $0\farcs56$ from a variable X-ray source with maximum luminosity of $2 \times 10^{38}\,\mathrm{ergs\,s^{-1}}$, which is consistent with the source being an X-ray binary (Remillard & McClintock 2006). M 81-7 has been classified as a galaxy by the SDSS survey, but with a photometric redshift $z = 0.00049$ comparable to that of M 81 (Abazajian et al. 2009). HST images show a region of enhanced star formation consisting of at least two components. Ancillary data also shows that N 7793-3 is probably a high-mass X-ray binary (Mineo et al. 2012) with a maximum X-ray luminosity of $3.9 \times 10^{37}\,\mathrm{ergs\,s^{-1}}$ (Liu 2011). Although we do not currently have an explanation, 5 of the candidates in M 33 (M 33-3 through M 33-7) are within $\lesssim 2\farcs0$ of radio-selected supernova remnants (Gordon et al. 1999).

4.4. Rate Limits

One advantage of searching for eruptions in the dust obscured phase is that the process is relatively easy to simulate. We use DUSTY (Elitzur & Ivezić 2001) to simulate the evolution of the mid-IR luminosities and determine the time t_d during which the source would satisfy our selection criteria. We eject M_e of material from a star of luminosity L_* and temperature T_* at velocity v_e over time period t_e and assume it forms dust with total (absorption plus scattering) visual opacity κ_V once it is sufficiently distant from the star. Here we use $\kappa_V = 84$ cm^2 g^{-1}, roughly appropriate for silicate dust, but this is important only to the extent that the ejecta mass can be rescaled as $M_e \propto \kappa_V^{-1}$. The key variable for estimating rates is the expansion velocity v_e, because the detection period scales as $t_d \propto v_e^{-1}$.

The debris around η Car show a broad range of velocities, radii, and temperature (Cox et al. 1995; Smith 2006). The ejecta from the Great Eruption are seen with peak velocities near 600 km/s along the long axis of the Homunculus nebula down to 100 km/s as you approach the lower latitudes. There are also dusty ejecta such as the disky "skirt" around the lower latitudes of the Homunculus nebula that have low to intermediate velocities and were probably ejected at later times. This means that the appropriate velocity to use to estimate the detectability of η Car in a spherical model depends on the epoch — at early phases, the hot dust emission that triggers our selection criteria is likely dominated by the fastest material ($v_e \simeq 600$ km/s) because the slower material can be optically thick in the mid-IR. At late times, like the present day, the appropriate velocity is the slowest velocity ($v_e \simeq 100$ km/s) because the fast moving dusty material is too cool even while retaining a substantial visual optical depth. Most other massive dusty shells in the Galaxy, which are believed to be older examples (10^3 to 10^4 years) of similar eruptions, are dominated by dusty ejecta with relatively slow velocities ($v_e \simeq 100$ km/s). Supernova impostors show velocity FWHM of order $500 - 1000$ km/s at peak (Smith et al. 2011), although some of these line widths could be created by Thomson scattering (see, e.g. Humphreys et al. 2012). Thus, a detailed model should consider a range of velocities, but for our present purposes, the late time detectability of such systems is determined by the slowest ($v_e \simeq 100$ km/s) rather than the fastest ($v_e \simeq 600$ km/s) ejecta velocities because this is the material producing the late time hot dust emission. Since η Car shows such material and is detected by our criteria at its present age, we scale the results by this slow velocity appropriate for late times. We include the velocity scalings in the expressions so that the role of the velocity is kept explicit.

Detection of a shell at late times ($t_d \gg t_e$) is limited by its optical depth and temperature. The shell has total visual optical depth greater than τ_V for

$$t(\tau_V) = \left(\frac{M_e \kappa_V}{4\pi v_e^2 \tau_V}\right)^{1/2} \simeq 400\tau_V^{-1/2} \left(\frac{M_e}{M_\odot} \frac{\kappa_V}{100\ \mathrm{cm}^2/\mathrm{g}}\right)^{1/2} \left(\frac{100\ \mathrm{km\,s}^{-1}}{v_e}\right) \ \text{years}, \tag{4.4}$$

and once $\tau_V < 1$ it begins to rapidly fade in the mid-IR. For $M_e \simeq 10\,\mathrm{M}_\odot$ like $\eta\,$Car and $\kappa_V = 84\ \mathrm{cm}^2\ \mathrm{g}^{-1}$, τ_V falls below 1 between ~ 200 years (for $v_e \simeq 600\ \mathrm{km\,s}^{-1}$) and ~ 1000 years (for $v_e \simeq 100\ \mathrm{km\,s}^{-1}$). Ignoring Planck factors, the spectral energy (λL_λ) peaks at

$$\lambda = \frac{hc}{4kT_d} \simeq 2\left(\frac{L_*}{10^6 L_\odot}\right)^{-1/4} \left(\frac{t}{\mathrm{year}} \frac{v_e}{100\ \mathrm{km\,s}^{-1}}\right)^{1/2} \ \mu\mathrm{m}, \tag{4.5}$$

so the emission peak shifts out of the IRAC bands after several decades, and our survey is primarily limited by the shift of the emission to longer wavelengths rather than the declining optical depth. It would be better to search for these sources at $24\,\mu$m as has been done in the galaxy (Wachter et al. 2010; Gvaramadze et al. 2010), but that would require the resolution of JWST (Gardner et al. 2006). A reasonable power-law fit to the results ($-1 \leq \log M_e/M_\odot < 1$, $5.5 < \log(L_*/L_\odot) < 6.5$) of the DUSTY models of eruptions lasting t_e years is that the detection period is

$$t_d \simeq t_e + 66\left(\frac{100\ \mathrm{km}s^{-1}}{v_e}\right)\left(\frac{L_*}{10^6 L_\odot}\right)^{0.82}\left(\frac{M_e}{M_\odot}\right)^{0.043} \ \text{years}. \tag{4.6}$$

For $M_e \simeq 10\,\mathrm{M}_\odot$ and $\mathrm{L}_* \simeq 10^{6.5}\,\mathrm{L}_\odot$ like $\eta\,$Car, $t_d \simeq t_e + 190(100\ \mathrm{km}s^{-1}/v_w)$ years where t_e may also be 50 years or more (see the discussion in Kochanek et al. 2012a). For present purposes, we adopt $t_d = 200$ years as the period over which our selection criteria would identify an analogue of $\eta\,$Car, given that our selection criteria indeed identify $\eta\,$Car.

We can normalize the rate of eruptions to the ccSN rate as

$$R_{erupt} \simeq 0.1 \left(\frac{40M_\odot}{M_{erupt}}\right)^{1.35} N_{erupt} R_{SN} = f_\eta R_{SN}, \tag{4.7}$$

where R_{SN} is the supernova rate and all stars more massive than M_{erupt} undergo N_{erupt} eruptions. Following the rate arguments in Kochanek (2011a), we can estimate the number of eruptions per massive star needed to explain the massive Galactic shells. If there are $N_{shell} \simeq 10$ massive Galactic shells associated with massive stars ($M > M_{erupt}$), then

$$N_{erupt} \simeq 2 \left(\frac{N_{shell}}{10}\right) \left(\frac{\tau_V}{0.01}\right)^{1/2} \left(\frac{\text{century}^{-1}}{R_{SN,MW}}\right) \left(\frac{M_{erupt}}{40M_\odot}\right)^{1.35} \left(\frac{10M_\odot}{M_e}\right)^{1/2} \left(\frac{v_e}{100\ \text{km}s^{-1}}\right), \tag{4.8}$$

where $\tau_V = 0.01$ is the minimum optical depth needed to detect a shell surrounding the star and $R_{SN,MW} \sim 1$/century is the Galaxy's supernova rate. Since the Galactic shells are identified as shells primarily at 24μm, they are easier to find at low optical depths and temperatures than in our extragalactic survey. Thus, the massive Galactic shells imply an eruption rate relative to the supernova rate of $f_\eta \gtrsim 0.2$ since it is unclear whether we possess a complete inventory. Note that with this normalization the rate estimate does not depend on the mass scale M_{erupt}.

4.5. Conclusions

This work empirically demonstrates that true analogs of η Car — massive stars that have undergone eruptive mass ejection in the recent past (centuries) — are rare. Based on the discussion in Section 2.4, our survey can detect close analogs of η Car for roughly $t_d \simeq 200$ years, consistent with η Car meeting our selection criteria. The statistics of our present sample gives us a maximum of $N_{cand} = 6 \pm 6$ candidate systems after correcting for the estimated extragalactic contamination. Aside from the three very compact, luminous star clusters, the candidates generally do not have SEDs that closely resemble the SED of η Car. Although we keep those three compact clusters in our candidate list for now, it is highly unlikely that they could hide luminous dusty stars similar to η Car. We anticipate that further analysis and follow-up observations, using HST astrometry and photometry, ground based spectroscopy and Herschel 70 μm photometry, will show that most, if not all, of the remaining candidates are either non-stellar or are not truly analogous to η Car. Of the true stellar systems, they are clearly going to be a mixture of "eruptions" such as η Car and sources with longer lived, relatively steady dusty winds such as Object X.

We will carry out the detailed consideration of the candidates in Chapter 5, but suppose we scale conclusions about the rates to $N_{cand} = 3$, which would also correspond to the 95% confidence upper limit we would use for estimating rate limits if we were to eliminate all the remaining candidates. This implies that we are probing eruption rates of order

$$R_{erupt} = \frac{N_{cand}}{t_d} = 0.015 \left(\frac{N_{cand}}{3}\right) \left(\frac{200 \text{ year}}{t_d}\right) \text{ year}^{-1} \tag{4.9}$$

for this sample of galaxies (roughly 1 per 200 years per galaxy), and fractional rates compared to the ccSN rate of order

$$f_\eta = 0.15 \left(\frac{N_{cand}}{3}\right) \left(\frac{200 \text{ year}}{t_d}\right) \left(\frac{0.1 \text{ year}^{-1}}{R_{SN}}\right) \tag{4.10}$$

that are in the appropriate regime. In fact, it seems likely that we should not find $N_{cand} = 0$ at the end of Chapter 5, and in some senses we already have that $N_{cand} \gtrsim 1$ since our present sample contains Object X.

Alternatively, we could estimate the expected number of candidates from ccSN rate and the statistics of Galactic shells as discussed in Section 2.4. For the galaxies in our pilot study, we have two rather inconsistent estimates of the ccSN rate. Empirically, there were three ccSN over the last 20 years, which implies a rate of $R_{SN} = 0.15\,\text{year}^{-1}$ ($0.05 < R_{SN} < 0.35\,\text{year}^{-1}$, at 90% confidence). On the other hand, the integrated star formation rate of the targeted galaxies implies a massive star formation rate, which is equivalent to the ccSN rate, of roughly $R_{SN} = 0.014\,\text{year}^{-1}$. $R_{SN} = 0.15\,\text{year}^{-1}$ implies that the expected number of candidates in the targeted galaxies should be $\simeq 6$ ($R_{SN} \times f_\eta \times t_d$ for $f_\eta \gtrsim 0.2$ and $t_d = 200\,\text{years}$) with a $> 3\sigma$ chance of finding at least 1. On the other hand, $R_{SN} = 0.014\,\text{year}^{-1}$ reduces the probability to only about 40% and implies that we need to study galaxies with an integrated star formation rate of $20\,M_\odot\,\text{year}^{-1}$ (10 times greater than what we have now) to have a $> 3\sigma$ chance of finding at least 1 massive dust obscured star.

In either case, our survey can be easily expanded to at least 10 times as many galaxies (and integrated star formation rate) simply using archival data from the SINGS, LVL, and S^4G surveys, which then probes rates far below those necessary to explain the Galactic sources. In such an expanded survey, additional means of suppressing contamination are important. The simplest method is to use the time variability of the mid-IR emission, since expanding shells of ejecta will also show a well defined pattern of fading (see Kochanek et al. 2012a) in the warm *Spitzer* bands (3.6 and 4.5 μm) and new *Spitzer* observations would provide a time baseline of 5–10 years to search for such changes. Since the principle background in our present survey appears to be extragalactic, time variability is a powerful means of suppressing it. Galaxies are not variable, and the mid-IR variability of quasars is both relatively weak and stochastic, with a structure function of roughly $0.1(t/4\text{ year})^{1/2}$ mag (Kozłowski et al. 2010). Two epochs separated by 6–12 months would further help to separate source classes by constraining variability on shorter time scales.

Table 4.1: Properties of Targeted Galaxies

Galaxy	Distance (Mpc)	M_B	$E(B-V)$	$\log_{10} L(H\alpha)$ (erg/s)	SFR (Hα) (M$_\odot$/yr)	Known ccSN ($<$ 20 years)
NGC 6822	0.46	-14.9	0.24	39.1	0.01	...
M 33	0.96	-18.8	0.04	40.6	0.33	...
NGC 300	1.9	-17.7	0.01	40.1	0.11	...
NGC 2403	3.1	-18.7	0.04	40.8	0.44	SN 2004dj (IIP)
M 81	3.6	-20.1	0.08	40.8	0.46	SN 1993J (IIb)
NGC 247	3.6	-18.2	0.02	40.3	0.17	...
NGC 7793	4.1	-18.5	0.02	40.6	0.33	SN 2008bk (IIP)

Table 4.2: Aperture Definitions

Band	Pixel Scale		R_{ap}	R_{in}	R_{out}
(μm)	(Archive)	(Survey)			
3.6-8.0	1″.2	0″.75	2″.4	2″.4	7″.2
24	2″.45	1″.5	3″.5	6″.0	8″.0
70	4″.0	4″.5	16″.0	18″.0	39″.0
160	8″.0	9″.0	16″.0	64″.0	128″.0

Table 4.3: Candidate Statistics

	NGC 6822	M 33	NGC 300	NGC 2403	M 81	NGC 247	NGC 7793
Survey Area A (deg^2)	0.1	0.73	0.17	0.12	0.17	0.2	0.044
Candidates	0	9	1	5	14	3	14
Expected Background Σ (deg^{-2})	0.17	1.67	11	47	75	75	110
Expected Contamination $A\Sigma$	0	1	2	6	13	15	5
Rejected Candidates	0	0	0	0	7	1	3
Remaining Candidates	0	9	1	5	7	2	11

Table 4.4: Rejected Candidates

ID	RA	Dec	Slope	$\log_{10}\frac{L_{mIR}}{L_\odot}$	f	Spectral Energy Distribution $[\log_{10}(\lambda L_\lambda/\mathrm{L}_\odot)]$						
			(a)			[3.6]	[4.5]	[5.8]	[8.0]	[24]	[70]	[160]
M 81-1	149.21474	69.12843	0.56	5.50	0.55	5.46	5.55	5.61	5.66	5.46	<5.28	<5.81
M 81-2	148.91331	69.29649	0.22	5.06	0.54	5.21	5.15	4.95	5.33	5.13	<5.53	<5.97
M 81-3	149.25626	68.91674	0.66	5.43	0.53	5.37	5.45	5.57	5.59	5.58	<5.50	<5.60
M 81-4	149.15222	69.00780	0.61	5.08	0.53	5.08	5.09	5.19	5.28	5.30	<5.63	<6.58
M 81-8	149.17365	68.80576	1.14	5.42	0.47	5.30	5.32	5.57	5.66	5.60	<5.51	<5.60
M 81-9	148.85034	69.24746	1.76	5.45	0.40	5.18	5.38	5.45	5.83	5.52	<6.46	<6.27
M 81-13	148.99657	69.26839	1.74	5.03	0.31	4.90	4.85	4.78	5.54	5.10	<6.14	<5.99
N 247-2	11.90806	−20.51950	1.35	5.10	0.36	5.13	4.85	5.01	5.55	5.46	<6.89	...
N 7793-2	359.47302	−32.47820	0.62	5.37	0.51	5.39	5.33	5.49	5.57	5.84	<5.99	<6.00
N 7793-5	359.34467	−32.62253	0.76	5.15	0.42	5.33	4.96	5.05	5.54	5.24	<6.13	<6.47
N 7793-7	359.46878	−32.63801	1.17	5.04	0.37	5.09	4.87	4.87	5.49	5.59	<6.08	<6.80

Table 4.5:: Remaining Candidates

ID	RA	Dec	Slope	$\log_{10} \frac{L_{mIR}}{L_\odot}$	f	Spectral Energy Distribution $[\log_{10}(\lambda L_\lambda/\mathrm{L}_\odot)]$						
			(a)			[3.6]	[4.5]	[5.8]	[8.0]	[24]	[70]	[160]
M 33-1[a,b]	23.35015	30.42626	0.24	5.11	0.57	5.14	5.17	5.25	5.21	5.13	<5.78	<6.09
M 33-2[a]	23.39209	30.69071	1.06	5.10	0.46	5.06	4.91	5.27	5.34	6.10	<6.90	<6.76
M 33-3	23.43939	30.61357	1.98	5.10	0.39	4.87	4.69	5.31	5.42	5.51	<6.15	<6.13
M 33-4	23.55650	30.56175	2.17	5.01	0.36	4.77	4.52	5.21	5.36	5.64	<6.44	<6.58
M 33-5	23.31891	30.88054	2.32	5.57	0.36	5.19	5.33	5.67	5.96	6.86	<6.90	<6.54
M 33-6	23.36988	30.67363	1.79	5.05	0.36	4.90	4.81	5.08	5.47	6.20	<6.57	<6.33
M 33-7	23.39793	30.65805	2.33	5.08	0.36	4.76	4.63	5.28	5.43	5.73	<6.33	<5.99
M 33-8[a]	23.50089	30.67987	2.40	5.56	0.35	5.22	5.13	5.72	5.94	6.46	<6.72	<6.50
M 33-9	23.37096	30.67276	2.34	5.02	0.32	4.73	4.61	5.10	5.45	6.12	<6.56	<6.34
N 300-1	13.71123	-37.67159	0.96	5.27	0.50	5.17	5.27	5.37	5.50	5.28	<6.23	<6.30
N 2403-1[a]	114.32964	65.59473	1.37	5.22	0.38	5.20	5.03	5.20	5.63	5.96	<6.96	<7.37
N 2403-2	114.20582	65.60922	2.00	5.11	0.36	4.93	4.68	5.25	5.49	5.31	<7.03	<7.57
N 2403-3	114.09702	65.61411	2.56	5.16	0.33	4.75	4.83	5.24	5.59	5.53	<6.77	<7.33

Continued on next page

Table 4.5 – continued from previous page

ID	RA	Dec	Slope	$\log_{10}\frac{L_{mIR}}{L_\odot}$	f	Spectral Energy Distribution $[\log_{10}(\lambda L_\lambda/\mathrm{L}_\odot)]$						
			(a)			[3.6]	[4.5]	[5.8]	[8.0]	[24]	[70]	[160]
N 2403-4[a]	114.22210	65.59257	2.20	5.17	0.32	4.98	4.71	5.24	5.61	5.24	<6.71	<7.45
N 2403-5	114.22632	65.59669	2.14	5.20	0.30	4.98	4.89	5.15	5.69	5.44	<6.90	<7.50
M 81-5	148.75421	69.12405	0.61	5.01	0.52	5.01	4.99	5.13	5.20	5.22	<6.06	<7.12
M 81-6	148.83128	68.95947	0.89	5.01	0.52	4.88	5.02	5.15	5.19	5.08	<5.50	<6.56
M 81-7	148.72035	69.14713	0.73	5.05	0.51	5.03	5.07	5.11	5.29	5.31	<6.74	<7.07
M 81-10	148.97075	68.98440	1.72	5.57	0.37	5.39	5.43	5.54	5.99	6.25	<7.20	<7.43
M 81-11	149.00545	68.98351	1.71	5.10	0.37	4.95	4.89	5.12	5.51	5.20	<6.70	<7.46
M 81-12	149.01479	68.98553	2.46	5.05	0.32	4.71	4.65	5.15	5.47	5.45	<6.70	<7.46
M 81-14	148.66461	69.08003	2.63	5.08	0.30	4.74	4.57	5.19	5.53	5.65	<6.92	<7.28
N 247-1	11.51449	−20.72367	1.12	5.14	0.50	4.97	5.15	5.25	5.38	5.28	…	<5.36
N 247-3[a]	11.91676	−20.90363	1.45	5.14	0.31	5.07	5.02	4.64	5.68	5.32	<5.95	<6.33
N 7793-1	359.39191	−32.54715	0.31	5.13	0.55	5.20	5.28	4.95	5.40	5.21	<5.45	<6.47
N 7793-3	359.43268	−32.60958	0.77	5.06	0.47	5.13	4.94	5.13	5.35	5.21	<6.06	<7.43
N 7793-4[a]	359.38553	−32.66690	0.91	5.34	0.46	5.34	5.32	5.31	5.67	5.53	<5.98	<6.36

Continued on next page

Table 4.5 – continued from previous page

ID	RA	Dec	Slope	$\log_{10}\frac{L_{mIR}}{L_\odot}$	f	Spectral Energy Distribution $[\log_{10}(\lambda L_\lambda/\mathrm{L}_\odot)]$						
			(a)			[3.6]	[4.5]	[5.8]	[8.0]	[24]	[70]	[160]
N 7793-6[a]	359.47568	−32.60091	1.58	5.14	0.38	5.05	4.85	5.22	5.51	5.43	<6.38	<7.51
N 7793-8[a]	359.42096	−32.65040	1.65	5.21	0.33	5.20	4.83	5.19	5.67	5.24	<6.09	<6.68
N 7793-9	359.46133	−32.58006	2.16	5.05	0.33	4.83	4.65	5.14	5.47	5.22	<6.94	<7.46
N 7793-10	359.41776	−32.61156	2.23	5.19	0.32	4.99	4.68	5.30	5.61	5.54	<6.67	<7.43
N 7793-11	359.41071	−32.60335	2.48	5.19	0.31	4.89	4.72	5.30	5.62	5.79	<6.96	<7.50
N 7793-12	359.48233	−32.60726	2.34	5.02	0.31	4.73	4.65	5.06	5.47	5.54	<6.46	<7.65
N 7793-13	359.42245	−32.59289	3.08	5.23	0.31	4.72	4.64	5.41	5.64	5.77	<6.93	<7.60
N 7793-14	359.47440	−32.57985	2.73	5.16	0.30	4.78	4.61	5.29	5.59	5.48	<6.59	<7.32

Table 4.6: Optical/NIR Luminosities of Stellar Candidates with 2MASS Counterparts

ID	RA	Dec	U	B	V	R	I	J	H	K
M 33-1	23.35015	30.42626	$\gtrsim 24.1$	$\gtrsim 24.2$	23.15	21.61	19.99	17.07	15.04	13.6
M 33-2	23.39209	30.69071	20.61	21.84	21.14	20.13	20.48	15.96	14.68	14.02
M 33-8	23.39026	30.69038	18.89	19.85	18.81	17.94	17.68	16.15	15.49	14.25
N 2403-1	114.32964	65.59473	...	...	...	...	...	14.89	14.42	14.21
N 2403-4	114.22210	65.59257	...	...	...	...	...	17.21	16.05	14.45
N 247-3	11.91676	−20.90363	...	...	...	...	...	15.73	14.79	14.58
N 7793-4	359.38553	−32.66690	...	...	...	...	...	16.30	15.59	15.17
N 7793-6	359.47568	−32.60091	...	...	...	...	...	16.45	15.98	15.58
N 7793-8	359.42096	−32.65040	...	...	...	...	...	16.07	15.56	14.14

---

[a] Identified as point sources in the 2MASS catalog (Cutri et al. 2003). See Table 4.6 for near-IR magnitudes.

[b] M 33-1 is Object X from Khan et al. (2011).

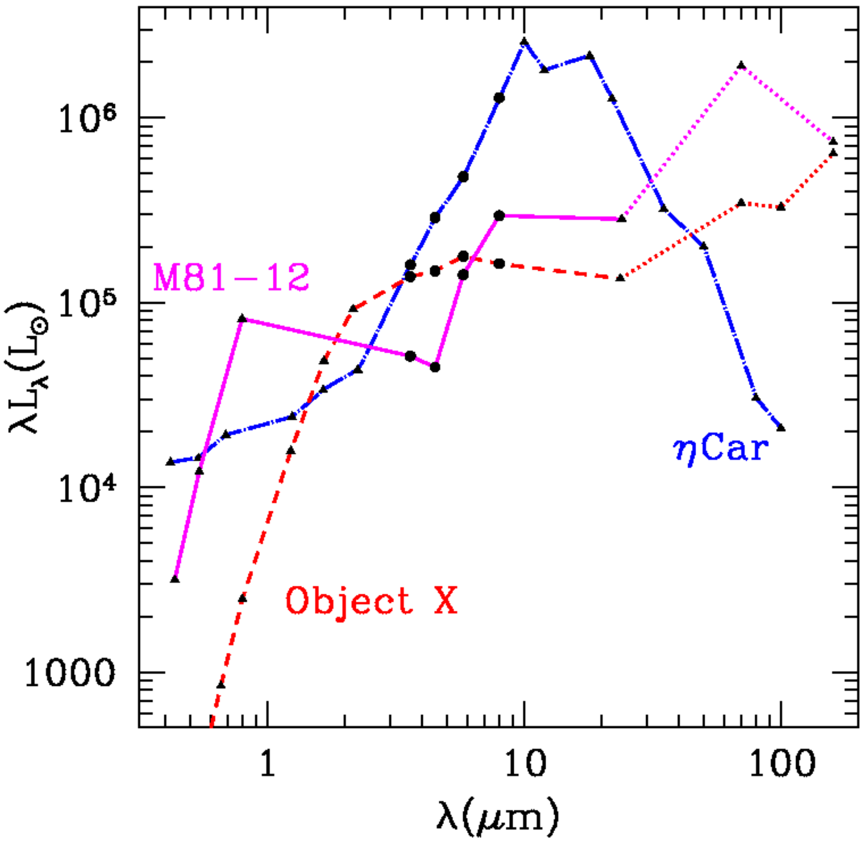

Fig. 4.1.— The Spectral Energy Distributions (SED) of η Car now (blue solid line, Humphreys & Davidson 1994), Object X (black solid line, Khan et al. 2011), and M 33 Var A (black dashed line, Humphreys et al. 2006). The black triangles mark luminosity at the IRAC band centers. Although η Car and Object X have similar luminosities up to 3.6 μm, the SED of η Car is steeply rising in the IRAC bands ($a \simeq$ 2.6; Eqn. 4.1) while Object X is almost flat ($a \simeq$ 0.2; Eqn. 4.1). Object X, and M 33 Var A (Hubble & Sandage 1953; Humphreys et al. 2006) are both dust obscured stars with comparable bolometric luminosities (Khan et al. 2011), but in the IRAC bands, Object X is much more luminous ($\sim 1.5 \times 10^5 L_\odot$) than M 33 Var A ($\sim 0.5 \times 10^5 L_\odot$).

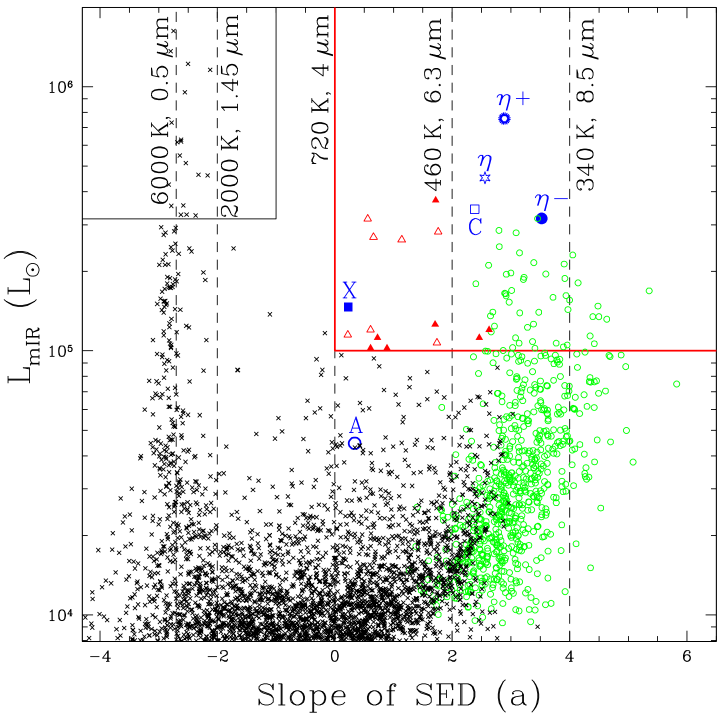

Fig. 4.2.— Integrated mid-IR luminosity L_{mIR} as a function of the slope a (Equation 4.1) for bright sources in M 81. The vertical dashed lines show the slopes of blackbodies with the indicated temperatures and peak wavelengths (Equation 4.2). The top-right (thick red) box shows the candidate selection region ($L_{mIR} > 10^5\,\mathrm{L}_\odot$ and $a > 0$). The red triangles show the sources that also satisfy the third selection criteria, that at least 30% of the integrated mid-IR luminosity is emitted between 3.6 and 5.8 μm ($f > 0.3$). Of these, the open red triangles correspond to candidates that are known to be non-stellar in nature (see Sections 4.2.3 and 4.3.1), and the solid red triangles represent the surviving candidates. The green open circles show sources with $f < 0.3$ and the black cross marks represent all the other sources. The narrow clump of points at $a \simeq -2.75$ correspond to normal stars with steeply falling mid-IR SEDs, while the wider clump of points to the right correspond to sources dominated by 8 μm PAH emission. The top-left box shows the region $L_{mIR} > 10^{5.5}\,\mathrm{L}_\odot$ and $a < -1$ that was used to select normal stars in the M 33 image (see Figure 4.5).

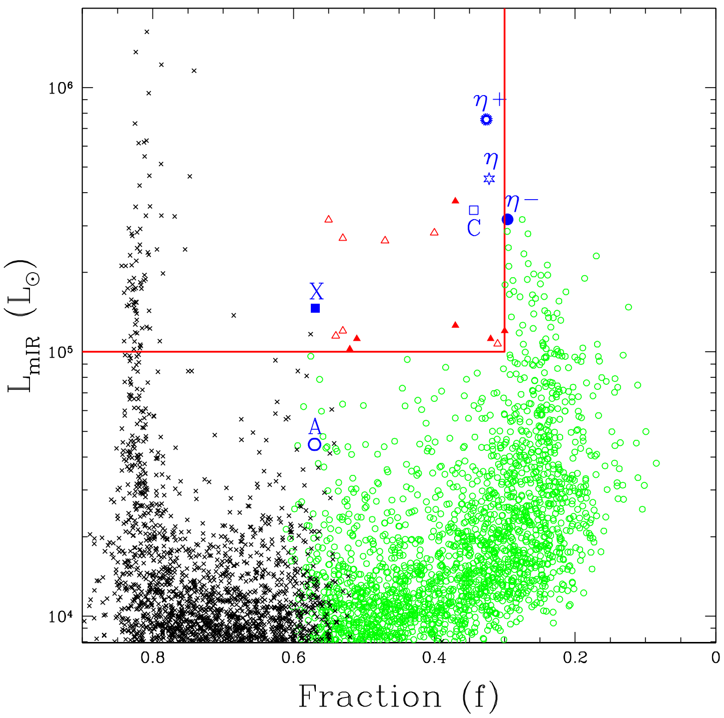

Fig. 4.3.— Integrated mid-IR luminosity L_{mIR} as a function of the fraction f of L_{mIR} that is emitted between 3.6 and 5.8 μm for bright sources in M 81. The box shows the candidate selection region ($L_{mIR} > 10^5\,L_\odot$ and $f > 0.3$). The red triangles show the sources that also satisfy the third selection criteria that the mid-IR SED slope (Equations 4.1) is either flat or rising ($a > 0$). Of these, the open red triangles correspond to candidates that are known to be non-stellar in nature (see Sections 4.2.3 and 4.3.1), and the solid red triangles represent the surviving candidates. The green open circles show sources with $a < 0$ and the black cross marks represent all the other sources. The narrow clump of points at $f \simeq 0.8$ correspond to normal stars with steeply falling (negative slope) mid-IR SEDs, while the wider clump of points at $f \simeq 0.25$ correspond to sources dominated by 8 μm PAH emission.

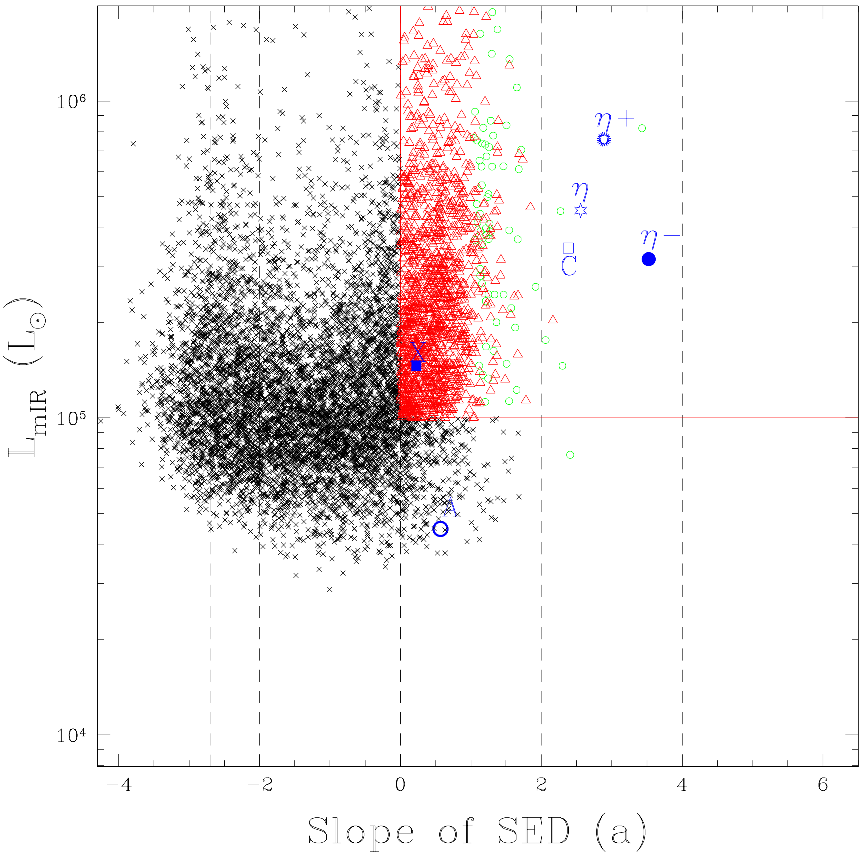

Fig. 4.4.— Extragalactic contamination for M 81. Here we show all sources from a 6 $\deg^2$ region of the SDWFS survey transformed to the distance of M 81. The symbols, lines, and axis-limits are the same as in Figure 4.2. In this SDWFS region, 449 ($\sim 75 \deg^{-2}$) sources pass our selection criteria, indicating that we should expect $\sim$ 13 background sources meeting our selection criteria given our 0.17 $\deg^2$ survey region around M 81. Note that very few of the contaminating background sources have properties comparable to η Car.

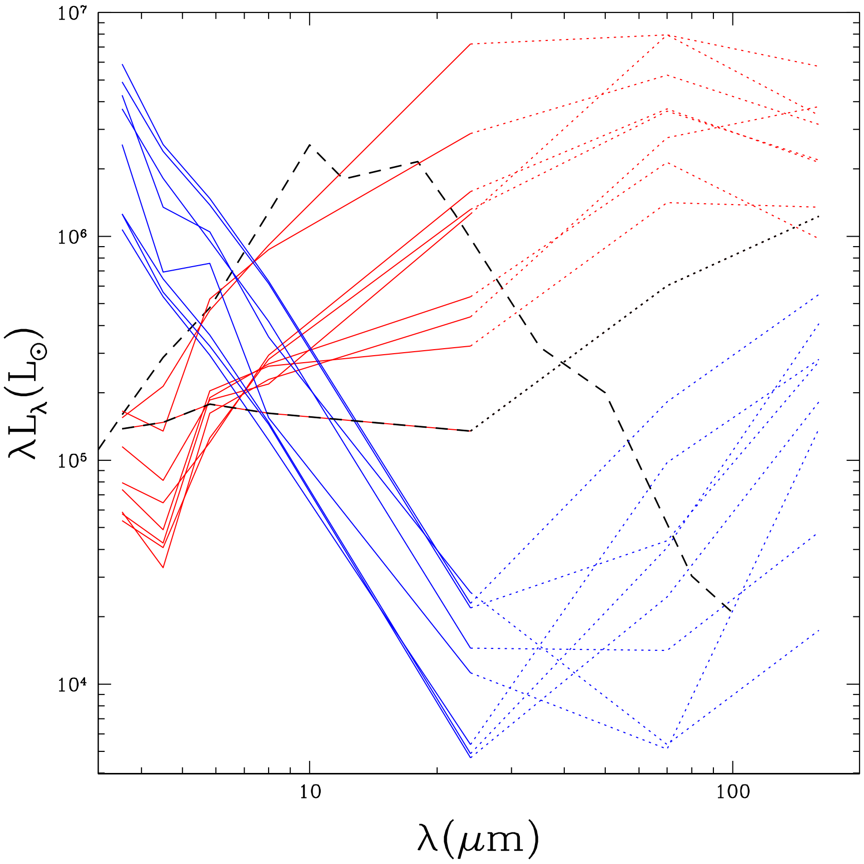

Fig. 4.5.— Mid and far-IR SEDs of the candidates in M 33 (red lines) compared to the SEDs of normal stars with $L_{mIR} > 10^{5.5}\,L_\odot$, which steeply *falling* SEDs (mid-IR slope $a < -1$, top left box of the Figure 4.2). The dotted portions of the SEDs correspond to the MIPS 70 and 160 μm flux upper limits. The SED of Object X is highlighted (red-black lighter dashed line) and η Car (black heavier dashed line) is shown for comparison.

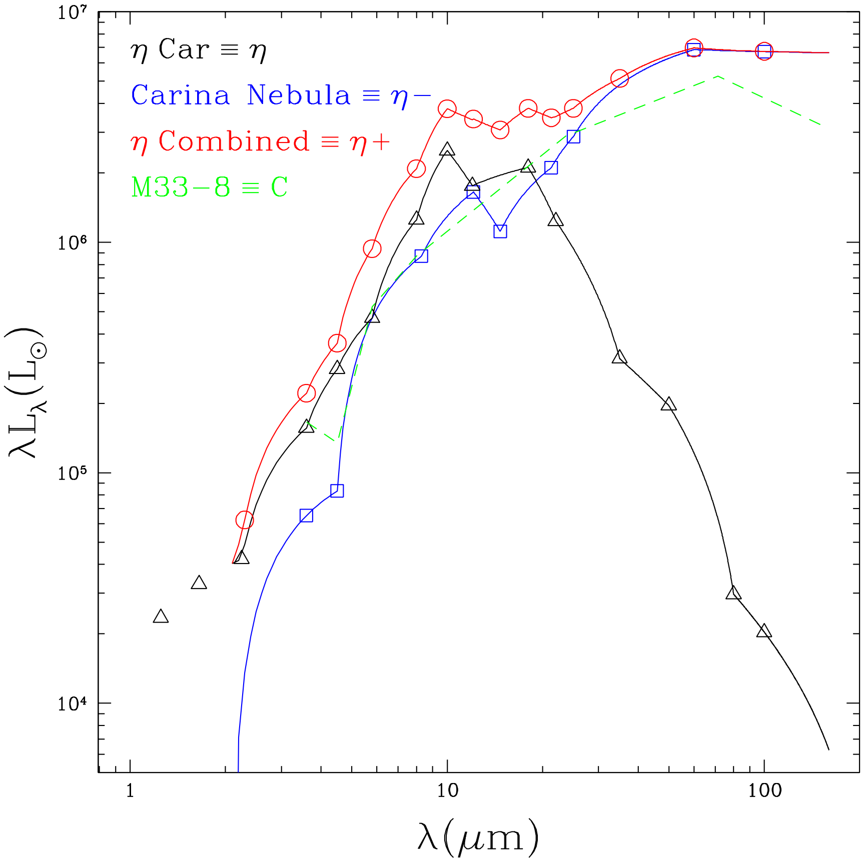

Fig. 4.6.— The SEDs of η Car ("η", black triangles, Humphreys & Davidson 1994), the Carina nebula excluding η Car itself ("η-", blue squares, Smith & Brooks 2007, and the entire dusty complex containing η Car and other massive stars including η Car ("$\eta+$", red circles, Section 4.2.4). The first two SEDs are spline interpolated and summed to produce the third. The SED of the compact cluster M 33-8 ("C", green dashed line, HST image in Figure 4.10) is shown for comparison. In Figures 4.2, 4.3, and 4.4 we label these η, $\eta-$, $\eta+$, and "C" respectively.

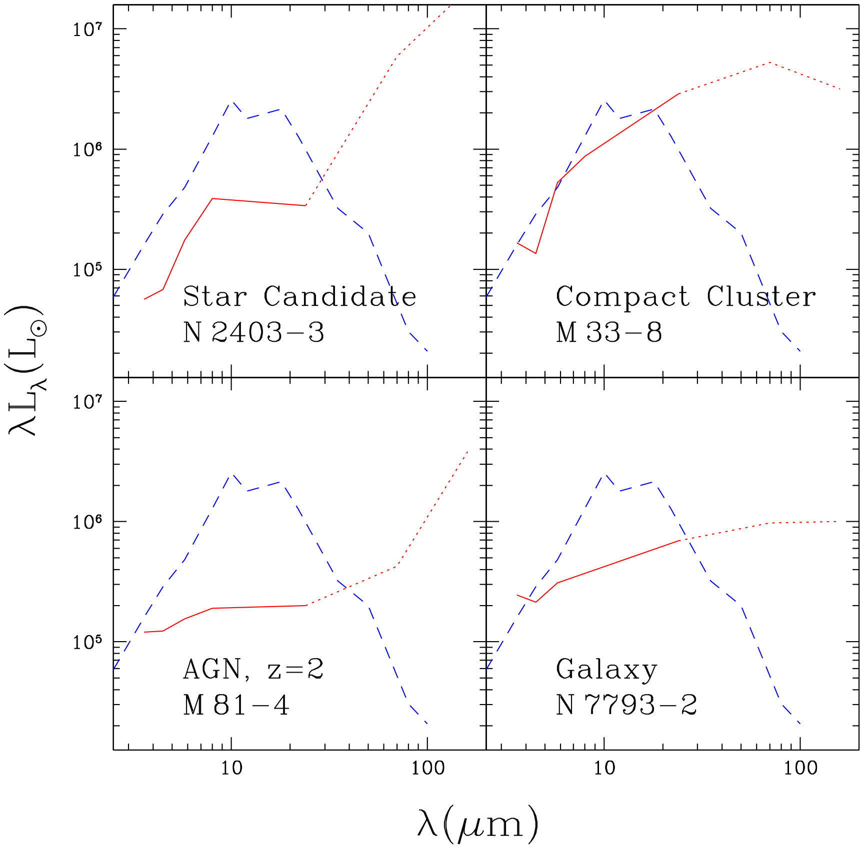

Fig. 4.7.— SEDs of four different classes of objects that met our selection criteria: a candidate dusty star in NGC 2403, a star-cluster in M 33, a QSO behind M 81, and a galaxy behind NGC 7793. Figure 4.10 shows IRAC and HST images of the compact cluster and the galaxy.

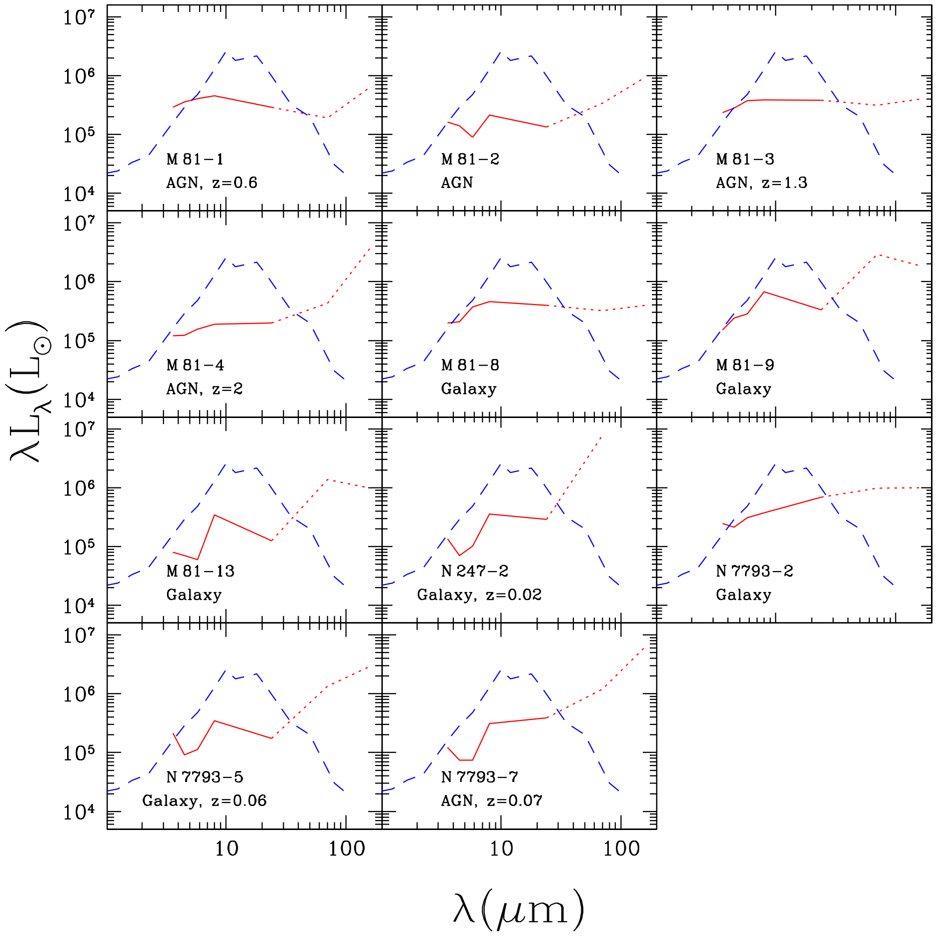

Fig. 4.8.— SEDs of sources that met our selection criteria but were rejected due to association with non-stellar sources. The dotted portions of the SEDs correspond to the MIPS 70 and 160 μm flux upper limits. The SED of η Car (dashed blue line) is shown for comparison.

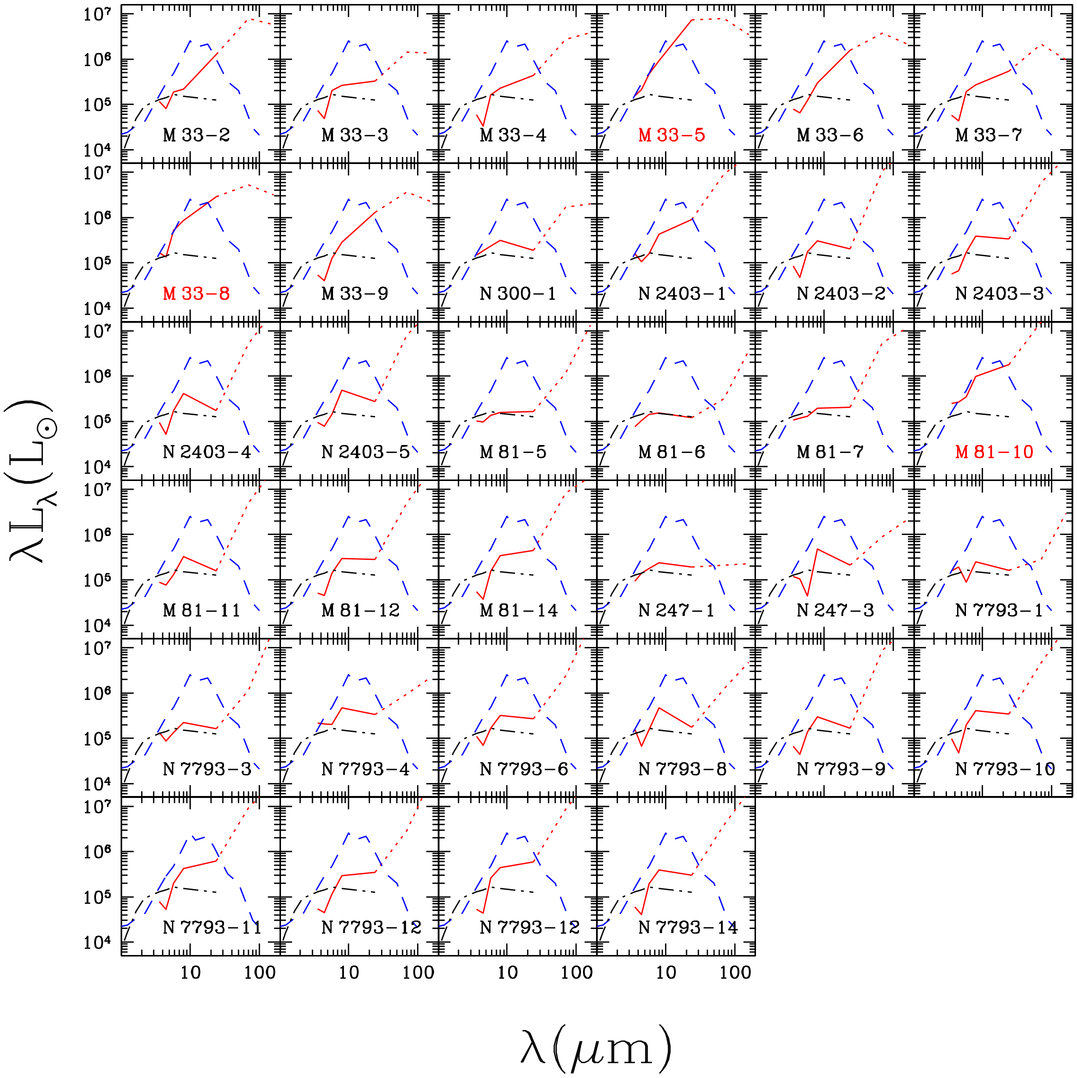

Fig. 4.9.— SEDs of sources that met our selection criteria and were *not* rejected due to association with non-stellar sources. The dotted portions of the SEDs correspond to the MIPS 70 and 160 μm flux upper limits. The SEDs of η Car (dashed blue line) and Object X (dot-dashed black line) are shown for comparison.

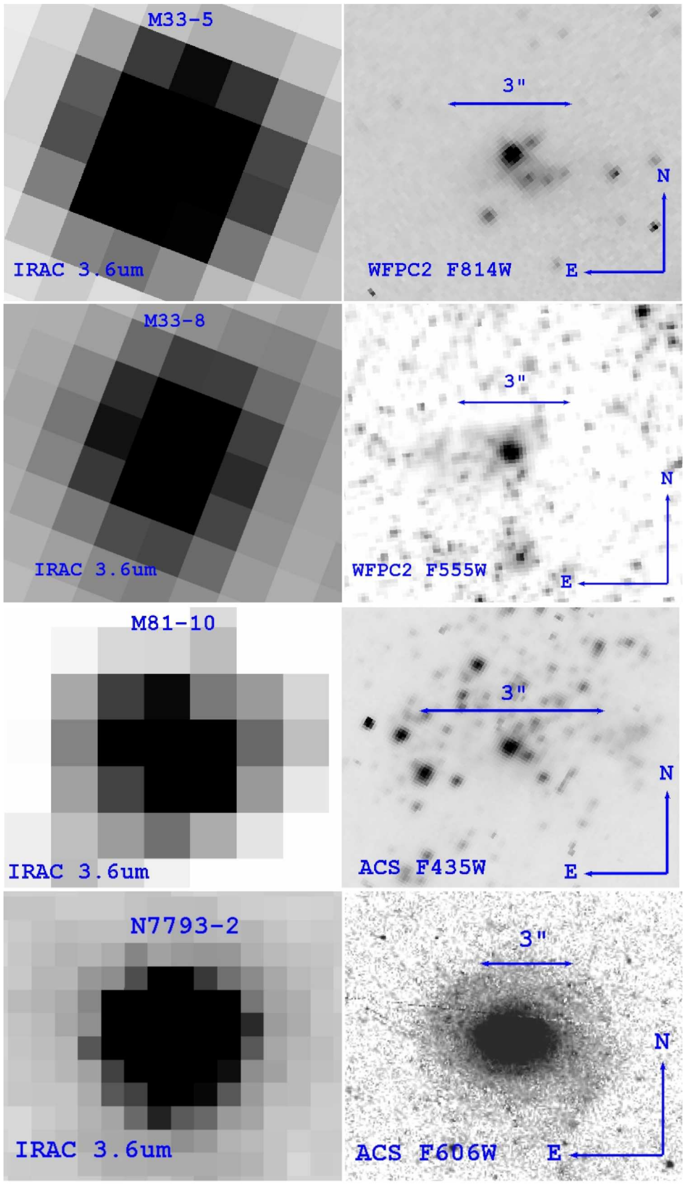

Fig. 4.10.— IRAC and HST images of the compact stellar clusters M 33-5, M 33-8, and M 81-10, and the background galaxy N 7793-2. The clusters are resolved in the HST images with FWHM of $0\farcs87 \simeq 4.1$ pc (M 33-5), $0\farcs77 \simeq 3.6$ pc (M 33-8) and $0\farcs34 \simeq 6.1$ pc (M 81-10). They are very luminous (few$\times 10^7\,L_\odot$) and their SED shapes are very similar to η Car (Figure 4.9).

Chapter 5: Identification of An Emerging Class of Extragalactic Self-Obscured Stars

Note: This chapter is based on the paper in preparation "Finding η Car Analogs in Nearby Galaxies Using Spitzer: II. Identification of An Emerging Class of Extragalactic Self-Obscured Stars", by R. Khan, C. S. Kochanek, K. Z. Stanek, and J. Gerke (Khan et al. 2014).

5.1. Introduction

Despite being very rare, massive stars such as luminous blue variable (LBVs), red super giants (RSGs), and Wolf-Rayet stars (WRs) play a pivotal role in enriching the interstellar medium (ISM) through mass loss, and they are an important source of heavier elements contributing to the chemical enrichment of galaxies (e.g., Maeder 1981). The deaths of these massive stars are associated with some of the highest energy phenomena in the universe such as core-collapse supernovae (ccSN) (ccSNe, Smartt et al. 2009), long-duration gamma-ray bursts (e.g., Stanek et al. 2003), neutrino bursts (e.g., Bionta et al. 1987) and gravitational wave bursts (e.g., Ott 2009). The physical mechanism, energetics and observed properties of these events depend on the structure and terminal mass of the evolved stars at core-collapse, which in turn are determined by stellar mass loss (see, e.g., review by Smith 2014). In addition, there is also evidence that some supernova (SN) progenitors undergo major mass ejection events shortly before exploding (e.g., Gal-Yam et al. 2007; Smith 2008; Ofek et al. 2013), further altering the properties of the explosion and implying a connection between some eruptive mass-loss events and death. It is generally agreed that the effects of winds are metallicity dependent (e.g., Meynet et al. 1994; Heger et al. 2003) and the SNe requiring a dense circumstellar medium (e.g., Schlegel 1990; Filippenko 1997) predominantly occur in lower metallicity galaxies (e.g., Stoll et al. 2011). This strongly suggests that the nature and distribution of stars undergoing impulsive mass loss will also be metallicity dependent and a full understanding requires exploring galaxies beyond the Milky Way.

Understanding the evolution of massive ($\mathrm{M} \gtrsim 30\,\mathrm{M}_\odot$) stars is challenging even when mass loss is restricted to continuous winds (e.g., Fullerton et al. 2006). However, shorter, episodic eruptions, rather than steady winds, may be the dominant mass loss mechanism in the tumultuous evolutionary stages toward the end of the lives of the most massive stars (e.g., Humphreys & Davidson 1984; Smith & Owocki 2006) as they undergo periods of photospheric instabilities leading to stellar transients ($M_V \lesssim -13$) followed by rapid ($\dot{M} \gtrsim 10^{-4}\, M_\odot$year) mass-loss in the last stages of their evolution (see Kochanek et al. 2012a; Smith 2014). Deciphering the rate of these eruptions and their consequences is challenging because No true analog of $\eta\,$Car in mass, luminosity, energetics, mass lost and age has been found (see Smith et al. 2011; Kochanek et al. 2012a), and the associated transients are significantly fainter than supernova explosions and are easily missed. These phases are as difficult to model theoretically as they are to simulate computationally. Dense winds tend to form dust, although for hot stars the wind must be dense enough to form a pseudo-photosphere in the wind (Davidson 1987) that shields the dust formation region from the UV emission of the star (Kochanek 2011b). The star will then be heavily obscured by dust for an extended period after the eruption (see, e.g., Humphreys & Davidson 1994). The Great Eruption of $\eta\,$Car between 1840 and 1860 is the most studied case of a stellar outburst (see, e.g., Humphreys et al. 2012).

The $\sim 10M_{\odot}$ ejecta are now seen as a dusty nebula around the star absorbing and then reradiating $\sim 90\%$ of the light in the mid-IR. This means that dusty ejecta are a powerful and long-lived signature of eruption. The emission from these dusty envelopes peaks in the mid-IR with a characteristic red color and a rising or flat spectral energy distribution (SED) in the *Spitzer* IRAC (Fazio et al. 2004) bands.

In the Galaxy, stars with resolved shells of dust emission are easily found at $24\,\mu$m (Wachter et al. 2010; Gvaramadze et al. 2010). The advantage of the $24\,\mu$m band is that it can be used to identify dusty ejecta up to $10^3 - 10^4$ years after formation. A minority of these objects are very luminous stars ($L \gtrsim 10^{5.5}$ $L_{\odot}$) with massive ($\sim 0.1 - 10$ $M_{\odot}$) shells (see summaries by Humphreys & Davidson 1994; Humphreys et al. 1999; Smith & Owocki 2006; Smith et al. 2009b; Vink 2012). These include AG Car (Voors et al. 2000), the Pistol Star (Figer et al. 1999), G79.29+0.46 (Higgs et al. 1994), Wray 17−96 (Egan et al. 2002), and IRAS 18576+0341 (Ueta et al. 2001). These systems are significantly older ($10^3 - 10^4$ years) than η Car, which makes it difficult to use the ejecta to probe the rate or mechanism of mass-loss. Still, the abundance of Galactic shells implies that the rate of η Car-like eruptions is on the order of a modest fraction of the ccSN rate (Kochanek 2011b). Their emission peaks in the shorter IRAC bands when they are relatively young ($\sim 10 - 100$ years) because, as the ejected material expands, the dust becomes cooler and the emission shifts to longer wavelengths (Kochanek et al. 2012a). It is difficult to quantify searches for such objects in our Galaxy because it is difficult to determine the distances to the sources and the survey volume because we have to look through the crowded and dusty disk of the Galaxy. Surveys of nearby galaxies are both better defined and build larger samples of younger systems whose evolution can be studied to better understand the mechanism. We previously demonstrated in Khan et al. (2010b, 2011) that it is possible to identify post-eruptive massive stars in galaxies beyond the local group using the mid-IR excess created by warm circumstellar dust despite crowding problems due to the limited spatial resolution of *Spitzer* at greater distances.

In Khan et al. (2013) ("Paper I" hereafter) we used archival *Spitzer* IRAC images of seven $\lesssim 4$ Mpc galaxies (NGC 6822, M 33, NGC 300, M 81, NGC 2403, NGC 0247 and NGC 7793) in a pilot study to search for extragalactic analogs of η Car. We found 34 candidates with flat or rising mid-IR spectral energy distributions (SEDs) and total mid-IR luminosity $L_{mIR} \gtrsim 5 \times 10^5 L_\odot$. In this Paper II, we characterize these sources and quantify the rate of episodic mass loss from massive stars in the last stages of evolution. We construct extended optical through far-IR SEDs using archival HST, 2MASS, and *Herschel* data as well as ground based data (Section 5.2). We classify the sources as either stellar or non-stellar based on properties of the extended SEDs and model the SEDs to infer the properties of the underlying star and the obscuring circumstellar medium (Section 5.3). We relate these properties to the observed ccSN rate of the targeted galaxies to quantify the rate of episodic mass loss in the last stages of massive star evolution (Section 5.4). Finally, we consider the implications of our findings for theories and observations of massive star evolution and their fates (Section 5.5).

5.2. Additional Wavelength Coverage

In this Section, we describe the details of how we obtained the photometric measurements at various wavelengths to determine the properties of the candidates from Paper I. The optical through far-IR photometry are reported in Table 5.2, and the extended SEDs are shown in Figures 5.7 and 5.8.

We utilized VizieR[1] (Ochsenbein et al. 2000) to search for other observations of the candidates, in particular for WISE (Wright et al. 2010, 12μm), 2MASS (Cutri et al. 2003, JHK_s), SDSS (Abazajian et al. 2009, *ugriz*) and X-ray detections. For M 33, we used the $UBVRI$ images from the Massey et al. (2006) optical survey, and archival HST images of NGC 300, NGC 2403, M 81, NGC 247 and NGC 7793. Finally, we used *Herschel* PACS data to supplement the *Spitzer* measurements.

For the *Spitzer* IRAC 3.6, 4.5, 5.8 and 8μm as well as MIPS (Rieke et al. 2004) 24, 70, and 160μm data, we use the measurements reported in Paper I. For M 33, our measurements were based on IRAC data from McQuinn et al. (2007) and MIPS data from the *Spitzer Heritage Archive*[2]. Data from the LVL survey (Dale et al. 2009) were used for NGC 300 and NGC 247, and data from the SINGS survey (Kennicutt et al. 2003) for NGC 6822, NGC 2403, and M 81.

We used the *Herschel* PACS (Poglitsch et al. 2010) 70, 100, and 160μm images available from the public *Herschel Science Archive*[3]. Although both MIPS and PACS cover the same far-IR wavelength range ($70 - 160\mu$m), Herschel has significantly higher resolution (see Figure 5.3). All three PACS band data were available for M 33 and NGC 7793, 70 and 160μm data were available for NGC 2403 and M 81, and 100 and 160μm data were available for NGC 300. There are no publicly available PACS images of the candidates in NGC 247. We used aperture photometry (IRAF[4] ApPhot/Phot) with the extraction apertures and aperture corrections from Balog et al. (2013) and given in Table 5.1. As with our treatment of the MIPS 70 and

---

[1] http://vizier.u-strasbg.fr/

[2] http://sha.ipac.caltech.edu/applications/Spitzer/SHA/

[3] http://herschel.esac.esa.int/Science_Archive.shtml

[4] IRAF is distributed by the National Optical Astronomy Observatory, which is operated by the Association of Universities for Research in Astronomy (AURA) under cooperative agreement with the National Science Foundation.

160μm measurements in Paper I, we treat the measurements obtained in the PACS bands as upper limits since the spatial resolution of these bands requires increasingly large apertures at longer wavelengths. For similar reasons, we also treat the WISE 12μm fluxes, where available, as upper limits.

For the optical photometry of the candidates in M 33, we used the Local Group Galaxies Survey *UBVRI* images (Massey et al. 2006). First we verified that the coordinates match with the IRAC images to within few$\times0\farcs1$ and then used $1\farcs0$ radius extraction apertures centered on the IRAC source locations. We transformed the aperture fluxes to Vega-calibrated magnitudes using zero point offsets determined from the difference between our aperture magnitudes and calibrated magnitudes for bright stars in the Massey et al. (2006) catalog of M 33.

For the candidates in NGC 300, M 81, NGC 2403, and NGC 247, we searched the ACS Nearby Galaxy Survey (ANGST, Dalcanton et al. 2009) B, V and (where available) I band point source catalogs derived using DOLPHOT (Dolphin 2000). We verified that the IRAC and HST astrometry of the NGC 300, NGC 2403 and NGC 247 images agree within (mostly) $\lesssim 0\farcs1$ to (in a few cases) $0\farcs3$. We corrected the astrometry of the M 81 HST images using the LBT images described later in this section to achieve similar astrometric accuracy. We also used the HST I-band photometry of M 81 from HST program GO-10250 (P.I. J. Huchra). We retrieved all publicly available archival HST images of NGC 7793 overlapping the IRAC source locations along with the associated photometry tables from the Hubble Legacy Archive[5]. The HST and *Spitzer* images have a significant (few$\times1\farcs0$) astrometric mis-match, and there are too few reference stars in the HST images to adequately improve the astrometry. Therefore, we utilized the IRAF GEOXYMAP and

---

[5] http://hla.stsci.edu/

GEOXYTRAN tasks to locally match the overlapping HST and *Spitzer* images of NGC 7793 within uncertainties of $0\farcs1 \sim 0\farcs3$.

We have variability data for the galaxies M 81 and NGC 2403 from a Large Binocular Telescope survey in the $UBVR$ bands that is searching for failed supernovae (Kochanek et al. 2008), and studying supernova progenitors and impostors (Szczygieł et al. 2012), and Cepheid variables (Gerke et al. 2011). We analyzed 27 epochs of data for M 81 and 28 epochs of data for NGC 2403, spanning a 5 year period. The images were analyzed with the ISIS image subtraction package (Alard & Lupton 1998; Alard 2000) to produce light curves (see Figure 5.5).

5.3. Characterizing the Candidates

In this section, we first discuss how we classify the candidates based on their SEDs. Next, we describe the non-stellar and stellar sources. Finally, we model the SEDs of the stellar sources to determine their physical properties. Figure 5.7 shows the SEDs of the stellar sources with the best fit SED models over plotted and Figure 5.8 shows the SEDs of the non-stellar sources.

5.3.1. Source Classification

We classify the candidates either as stellar or non-stellar based on their photometric properties. We focus on identifying two tell-tale signatures of the SED of a luminous star obscured by warm circumstellar dust — low optical fluxes or flux-limits compared to mid-IR luminosities and signs of a SED turning over between 8 μm and 24 μm. Towards longer wavelengths, emission from warm circumstellar dust should peak between the IRAC 8 μm and MIPS 24 μm bands, rather than beyond 24 μm as is expected for environments such as intra-cluster dust. Therefore, any SED that appears to have a steep slope between 8 and 24 μm is considered to be a likely cluster, rather than a single dust obscured star. Frequently these sources are also too luminous to be a single star. At the shorter wavelengths, we expect a dusty star to have relatively lower luminosity compared to its mid-IR luminosity and redder optical colors.

We examine the HST $B-V/V$ and the $V-I/V$ color magnitude diagrams (CMDs) for each source for which HST data is available. Either the presence of a very red optical counterpart, or the absence of a luminous star, supports the existence of significant dust obscuration. On the other hand, the presence of a blue or bright optical counterpart makes it likely that the source is a star cluster, a background galaxy/AGN, or a foreground star. First, we search for bright and/or red optical sources within the $0\farcs3$ matching radius that can be the obvious counterpart of the bright and red IRAC source. Next, if multiple bright and/or red optical matches are found, we identify the best astrometric match to the IRAC location. Finally, if no reasonable match is found, we adopt the flux of the brightest of the nearby sources as a conservative upper limit on the optical luminosity of the candidate.

To demonstrate the steps that we followed to classify these sources, we discuss the case of M 81-12 in detail. M 81-12 has a steeply rising optical and mid-IR SED (Figure 5.1) with two distinct peaks — one in the near-IR between the R-band and $3.6\,\mu$m, and another in the mid-IR between 8 and $24\,\mu$m. Figure 5.4 shows the HST optical CMD for sources near the location of M 81-12. Besides the sources within the $0\farcs3$ matching radius, it also shows all sources within $0\farcs3-2\farcs0$ of the candidate using a different symbol to emphasize the absence of any other unusual nearby sources. We detect a very red ($B=23.95$, $V=21.98$, $I=19.07$, $B-V\simeq 2$, $V-I\simeq 2.9$) HST counterpart with an excellent astrometric match ($<0\farcs1$, Figure 5.2) to the IRAC position. This source is the brightest, red HST point source within $2\farcs0$ of the IRAC location (Figure 5.4). The LBT V and R band light curves show a variable source with the correlated irregular variability (~0.4 mag, Figure 5.5) typical of many evolved massive stars (e.g., Kourniotis et al. 2014). Based on the SED shape and the unambiguous detection of a red, variable optical counterpart, we conclude that M 81-12 is a massive dust obscured single star.

In addition to Object X (M 33-1), we identified 17 additional dust obscured stars and classified 16 others as non-stellar. We left one source (N 7793-12) unclassified due to lack of sufficient data because (it falls on an HST/ACS chip gap). It could well be a dusty star, but we do not discuss it further.

5.3.2. The 18 Stars and 16 Non-stellar Sources

We identify 18 (including Object X/M 33-1) sources as dusty stars. Of these, four are in M 33 (1, 3, 4, 7), one is in NGC 300 (N 300-1), four are in NGC 2403 (2, 3, 4, 5), five are in M 81 (5, 6, 11, 12, 14), and four are in NGC 7793 (3, 9, 10, 13). These stars have low optical fluxes or flux limits and their SEDs turn over between 8 μm and 24 μm. Moreover, M 81-11, M 81-12 and N 2403-2 are detected as significantly variable sources in the LBT monitoring data. N 2403-3 is a saturated source in the HST images, and we use the LBT flux measurements as upper limits on its optical flux. N 2403-3 and N 2403-5 are not variable in the LBT data. M 81-5 is $0\farcs56$ from a variable X-ray source with maximum luminosity of 2×10^{38} ergs s^{-1} (Liu 2011), which is consistent with the source being an X-ray binary (Remillard & McClintock 2006). N 7793-3 is also a X-ray source (Liu 2011), with a maximum X-ray luminosity of 3.9×10^{37}ergs^{-1} and is classified as an HMXB by Mineo et al. (2012).

There are 16 candidates whose SEDs indicate that they are not self-obscured stars. Five sources in M 33 (2, 5, 6, 8, 9) have SEDs that nearly monotonically rise from the optical to 24 μm, unambiguously indicating the presence of cold dust associated with star clusters. As we discussed in Paper I, it is unlikely for an ultra-compact star cluster to host both evolved massive stars and significant amounts of intra-cluster dust. Eight sources cannot be dust obscured stars given their very high optical luminosities: N 2403-1 (likely a foreground star), M 81-7, M 81-10, N 247-3 (likely a foreground star, optical magnitudes from Space Telescope Science Institute & Osservatorio Astronomico di Torino 2001), N 7793-4, N 7793-8, N 7793-11, and N 7793-14. Among these, M 81-7, M 81-10 and N 2403-1 are not variable in the LBT data. We consider three more sources as most likely non-stellar due to reasons that are unique in each case —

- N 247-1 is located far from the plane of its edge-on host and is unlikely to be associated with the host.

- N 7793-1 is located at the edge of its host galaxy and the PACS far-IR flux limits are significantly lower than those of the sources that we classified as obscured stars, indicating an absence of the diffuse emission commonly associated with star forming regions.

- N 7793-6 has a SED that can conceivably be produced by a hot star with significant circumstellar material, although the near-IR peak seems too narrow. However, a close inspection of the HST image shows that this source is in a dense star-forming region with significant diffuse light indicating the presence of intra-cluster dust. None of the sources in the HST image are a good astrometric match to the IRAC location. It is more likely, in this case, that warm intercluster dust is producing the mid-IR flux excess. The optical fluxes adopted here are those of the most luminous HST source within a larger matching radius of $0\farcs5$.

In Paper I, we anticipated that further analysis would show that most, if not all, of the candidates are in fact non-stellar sources. Based on the expected surface density of extragalactic contaminants, of the 46 initial candidates we estimated that all but 6 ± 6 are background galaxies/AGN with 11 already being identified as such. Here we find that 18 (including Object X) of the candidates are dusty massive stars and very few of the other sources are background galaxies. We do not presently have an explanation for the fewer than expected background sources in the targeted fields.

5.3.3. SED Modeling

We fit the SEDs of the 18 self-obscured stars using DUSTY (Ivezic & Elitzur 1997; Ivezic et al. 1999; Elitzur & Ivezić 2001) to model radiation transfer through a spherical dusty medium surrounding a star and Figure 5.7 shows the best fit models. We estimate the properties of a black-body source obscured by a dusty shell surrounding it that would produce the best fit to the observed SED (see Figure 5.6 for an example). We considered models for either graphitic or silicate (Draine & Lee 1984) dust. We distributed the dust in a shell with a $\rho \propto 1/r^2$ density distribution. The models are defined by the stellar luminosity (L_*), stellar temperature (T_*), the total (absorption plus scattering) V-band optical depth (τ_V), the dust temperature at the inner edge of the dust distribution (T_d), and the shell thickness $\zeta = R_{out}/R_{in}$. The exact value of ζ has little effect on the results, and after a series of experiments with $1 < \zeta < 10$, we fixed $\zeta = 4$ for the final results. We embedded DUSTY inside a Markov Chain Monte Carlo (MCMC) driver to fit each SED by varying T_*, τ_V, and T_d. We limit T_* to a maximum value of 30,000 K to exclude unrealistic temperature regimes.

The parameters of the best fit model determine the radius of the inner edge of the dust distribution (R_{in}). The mass of the shell is

$$M_e = \frac{4\pi R_{in}^2 \tau_V}{\kappa_V} \tag{5.1}$$

where we simply scale the mass for a V band dust opacity of $\kappa_V = 100\,\kappa_{100}$ cm^2 g^{-1} and the result can be rescaled for other choices as $M_e \propto \kappa_V^{-1}$. Despite using a finite width shell we focus on R_{in} because it is well-constrained while R_{out} (or ζ) is not. We can also estimate an age for the shell as

$$t_e = \frac{R_{in}}{v_e} \tag{5.2}$$

where we scale the results to $v_e = 100\,v_{e,100}\,\mathrm{km\,s^{-1}}$.

For a comparison sample, we followed the same procedures for the SEDs of three well-studied dust obscured stars: η Car (Humphreys & Davidson 1994); the Galactic OH/IR star IRC+10420 (Jones et al. 1993; Humphreys et al. 1997; Tiffany et al. 2010); and M 33's Variable A, which had a brief period of high mass loss leading to dust obscuration over the last ~ 50 years (Hubble & Sandage 1953; Humphreys et al. 1987, 2006). We use the same SEDs for these stars as in Khan et al. (2013). In Table 5.4, we report χ^2, τ_V, T_d, T_*, R_{in}, L_*, M_e (Equation 5.1), and t_e (Equation 5.2) for the best fit models of these three sources as well as the newly identified stars. The stellar luminosities required for both dust types are mutually consistent because the optically thick dust shell acts as a calorimeter. However, because the stars are heavily obscured and we have limited optical/near-IR SEDs, the stellar temperatures generally are not well constrained. In some cases, for different dust types, equally good models can be obtained for either a hot ($> 25000\,K$, such as a LBV in quiescence) or a relatively cooler ($< 10000\,K$, such as a LBV in outburst) star.

Indeed, for many of our 18 sources, the best fit is near the fixed upper limit of $T_* = 30000\,K$. To address this issue, we also tabulated the models on a grid of three fixed stellar temperatures, $T_* = 5000\,K, 7500\,K, 20000\,K$, for each dust type. The resulting best fit parameters are reported in Tables 5.6 and 5.9.

Figure 5.9 shows the integrated luminosities of the newly identified self-obscured stars described in Section 5.3.2 as a function of M_e for the best fit graphitic models of each source. Object X, IRC+10420, M 33 Var A, and η Car are shown for comparison. Figure 5.10 shows the same quantities, but for various dust models and temperature assumptions. It is apparent from Figure 5.10 and Tables 5.4, 5.6 and 5.9 that the integrated luminosity and ejecta mass estimates are robust to these uncertainties. The exceptions are N 2403-4 and N 7793-3. Without any optical or near-IR data, many of the models of N 7793-3 are unstable so we simply drop it. The only models having a luminosity in significant excess of $10^6\,L_\odot$ are some of the fixed temperature models of N 2403-4. These models have a poor goodness of fit and can be ignored.

One check on our selection methods is to examine the distribution of shell radii. Crudely, we can see a shell until it either becomes optically thin or too cold, so the probability distribution of a shell's radius is

$$\frac{dN}{dR_{in}} = \frac{1}{R_{max}} = \text{constant} \tag{5.3}$$

for $R_{in} < R_{max}$. An ensemble of shells with similar R_{max} should then show this distribution. Figure 5.11 shows the cumulative histogram (excluding N 7793-3) of the inner shell radii (R_{in}). The curves show the expected distribution simply normalized at the point where $F\,(< R_{in}) \simeq 0.5$. The agreement shows that our sample should be relatively complete up to $R_{max} \simeq 10^{16.5}$-10^{17} cm which corresponds to a maximum age of

$$t_{max} \simeq 300\, v_{e,100}^{-1} \text{ years.} \tag{5.4}$$

Figure 5.12 shows the age ($t = R_{in}/v_{100}^{-1}$) of the shells as a function of M_e. We also show lines corresponding to optical depths of $\tau_V = 1, 10, 100$. As expected, we see no sources with very low or high optical depths, as we should have trouble finding sources with $\tau_V < 1$ due to a lack of mid-IR emission and $\tau_V \gtrsim 100$ due to the dust photosphere being too cold (peak emission in the far-IR). Indeed, most of the dusty stars have $1 < \tau < 10$ and none has $\tau > 100$. The large t estimate for η Car when scaled by $v_{e,100}$ is due to the anomalously large ejecta velocities ($\sim$ 600km s^{-1} along the long axis (Cox et al. 1995; Smith 2006) compared to typical LBV shells ($\sim$ 50km s^{-1}, Tiffany et al. 2010).

5.4. Implications

The advantage of surveying external galaxies with a significant supernova rate is that we can translate our results into estimates of abundances and rates. We scale our rates using the observed supernova rate of $R_{SN} = 0.15$ year^{-1} ($0.05 < R_{SN} < 0.35$ at 90% confidence). As we discussed in Paper I, this is significantly higher than standard star formation rate estimates for these galaxies, but the SN rate is directly proportional to the massive star formation rate rather than an indirect indicator, and similar discrepancies, although not as dramatic, have been noted in other contexts (e.g., Horiuchi et al. 2011). In this section we first outline how we will estimate rates, and then we discuss the constraints on analogues of η Car and the implications of our sample of luminous dusty stars.

We are comparing a sample of $N_{SN} = 3$ supernovae observed over $t_{SN} = 20$ years to a sample of N_c candidate stars which are detectable by our selection procedures for a time t_d. In Paper I we used DUSTY to model the detection of expanding dusty shells and found that a good estimate for the detection time period was

$$t_d = t_w + 66 \left(\frac{100 \text{ km s}^{-1}}{v_e} \right) \left(\frac{L_*}{10^6 L_\odot} \right)^{0.82} \left(\frac{M_e}{M_\odot} \right)^{0.043} \text{ years} \tag{5.5}$$

for shells with masses in the range $-1 \leq \log M_e/M_\odot \leq 1$ around stars of luminosity $5.5 \leq \log L_*/L_\odot \leq 6.5$ where t_w is the duration of the "wind" phase and the second term is an estimate of how long the shell will be detected after the heavy mass loss phase ends. The principle uncertainty lies in the choice of the velocity, v_e. If the rate of events in the sample is R_e, then we expect to find $N_e = R_e t_d$ candidates.

The transient rate in a sample of galaxies is less interesting than comparing the rate to the supernova rate. Let f_e be the fraction of massive stars that create the transients, where $f_e = (M_\eta/8M_\odot)^{-1.35}$ if we assume a Salpeter IMF (Kennicutt 1998), that all stars more massive than $8M_\odot$ become supernovae and that all stars more massive than M_η cause the transients. If each star undergoes an average of N_e eruptions, then the rate of transients is related to the rate of supernovae by $R_e = N_e f_e R_{SN} = F_e R_{SN}$. The interesting quantity to constrain is F_e rather than R_e. Poisson statistics provide constraints on the rates, where $P(D|R) \propto (Rt)^N \exp(-Rt)$ for N events observed over a time period t. This means that the probability of the rates given the data is

$$P(R_{SN}, R_e|D) \propto P(R_{SN}) P(R_\eta) (R_{SN} t_{SN})^3 (R_\eta t_d)^{N_c} \exp(-R_{SN} t_{SN} - R_\eta t_d) \tag{5.6}$$

where $P(R_{SN})$ and $P(R_\eta)$ are priors on the rates which we will assume to be uniform and we have set $N_{SN} = 3$. If we now change variables to compute F_e and marginalize over the unknown supernova rate, we find that the probability distribution for the ratio of the rates is

$$P(F_e|D) \propto F_e^{N_c} \left(F_e t_d + t_{SN}\right)^{-5-N_c} \tag{5.7}$$

with the standard normalization that $\int P(F_e|D) dF_e \equiv 1$. For our estimates of F_e we present either 90% confidence upper limits or the value corresponding to the median probability and symmetric 90% probability confidence regions. Note that the probability distribution really just depends on the product $F_e t_d$, so the results for any given estimate of t_d are easily rescaled.

5.4.1. No η Car Analogue Is Found

It is immediately obvious from Figure 5.9 that none of the sources we identified closely resemble η Car. Their typical luminosities of $10^{5.7\pm0.2} L_\odot$ correspond to $\sim 40 M_\odot$ stars (Maeder 1981; Maeder & Meynet 1987, 1988; Stothers & Chin 1996; Meynet et al. 1994) rather than the higher masses usually associated with LBV outbursts. Since we identify a significant population of fainter stars, this is unlikely to be a selection effect, and we conclude that these galaxies contain no analogs of η Car.

There are two ways we can interpret the result. First, we can ignore the existence of η Car, and set $N_c = 0$. Alternatively, we can acknowledge the existence of η Car, in which case $N_c = 1$, since η Car passes our selection criterion and mid-IR surveys of our Galaxy for objects as luminous as η Car are probably complete. For the first case, the 90% confidence upper limit is $F_e < 0.077 t_{d200}^{-1}$ where the period over which such systems can be detected is scaled to $t_d = 200 t_{d200}$ years. For the second case, where we include η Car, we find that $F_e = 0.046 t_{d200}^{-1}$ with

$0.0083 < F_e t_{d200} < 0.19$ at 90% confidence. In either case, the rate of transients comparable to η Car is a small fraction of the supernova rate.

Stars as massive as η Car are also rare, representing only $f_e = 0.02$ to 0.04 of all massive stars for a mass range from $70/100M_\odot$ to $200M_\odot$. If every sufficiently massive star had one eruption, the results including η Car correspond to a minimum mass of $M_\eta = 65M_\odot$ ($26M_\odot < M_\eta < 138M_\odot$). If every star has an average of two eruptions, the mass limits rise to $M_\eta = 94M_\odot$ ($42M_\odot < M_\eta < 162M_\odot$). Similarly the upper limit from ignoring the existence of η Car corresponds to $M_\eta > 48M_\odot$ for an average of one eruption or $M_\eta > 72M_\odot$ for an average of two. Kochanek (2011b) estimated that the abundance of lower optical depth shells found at 24μm around massive stars in the Galaxy was roughly consistent with all stars more massive than $M_\eta = 40M_\odot$ having an average of two eruptions, corresponding to $F_e \simeq 0.2$, which is consistent with the present results but close to the upper limits.

5.4.2. An Emerging Class of Dust Obscured Stars

All the newly identified stars have luminosities within a narrow range of $\log L/L_\odot \simeq 5.5$-6.0 (see Figure 5.10), which roughly corresponds to initial stellar masses of $M_{ZAMS} \simeq 25$-$60M_\odot$ (see Section 4 of de Jager 1998, and references therein). Local examples of evolved stars in this luminosity range are the Yellow Hypergiants (YHGs) such as IRC+10420, ρ Cas and HR 8752 (de Jager & Nieuwenhuijzen 1997; Smith & Owocki 2006), many of which are also partially obscured by dust ejecta. There is no means of cleanly surveying the Galaxy for these objects and they are so rare that samples in the Galaxy and the Magellanic Clouds do not provide good statistics for their abundances, life times or total mass loss. Our well-defined sample of likely extragalactic analogues provides a means of addressing some of these questions.

If we assume these objects are similar to stars like IRC+10420, their expansion velocities will be more like 50 km/s than the 100 km/s of the typical LBV shell. Hence, it seems more appropriate to scale the results to $t_d = 500 t_{d500}$ years. This also matches the estimated age of the phase of dusty mass loss by IRC+10420 (Tiffany et al. 2010). With 18 candidates, this detection period then leads to a median estimate that $F_e = 0.20 t_{d500}^{-1}$ with $0.086 < F_e t_{d500} < 0.55$. If we associate these with the mass range from 25 to $60 M_\odot$, they represent a fraction of $f_e \simeq 0.15$ of massive stars, so the average number of episodes per star, $N_e = F_e/f_e \simeq 1.3 t_{d500}^{-1}$ with a possible range of $0.58 < N_e t_{d500} < 3.7$, although this does not include the uncertainties in f_e

Figure 5.9 shows that the median mass causing the obscuration is $M_e \sim 0.5 M_\odot$. The total mass lost is then of order $N_e M_e$ which would be of order 0.3-$1.9 t_{d500}^{-1} M_\odot$. This implies that periods of (dust) optically thick mass loss cannot dominate the overall mass loss of the star. To make mass lost in these phases dominate either requires that we have grossly overestimated t_d, or that the mass range of the stars is much narrower. A related point is that these phases represent a negligible fraction of the post-main-sequence life times of the stars, at most lasting a few thousand years.

5.5. Conclusions

In our survey, we have found no true analogues of η Car. This implies that the rate of Great Eruption-like events is of order $F_e = 0.046 t_{d200}^{-1}$ $(0.0083 < F_e t_{d200} < 0.19)$ of the ccSN rate, which is roughly consistent with each $M \gtrsim 70 M_\odot$ undergoing 1 or 2 such outbursts in its lifetime. This is scaled by an estimated detection period of order $t_d = 200 t_{d200}$ years. We do identify a significant population of lower luminosity dusty stars that that are likely similar to IRC+10420. Stars enter this phase at the rate $F_e = 0.20 t_{d500}^{-1}$ $(0.086 < F_e t_{d500} < 0.55)$ compared to the ccSN rate and for a detection period of $t_d = 500 t_{d500}$ years. Here the detection period is assumed longer because the expansion velocities are likely slower. This rate is comparable to having all stars with $25 < M < 60 M_\odot$ undergoing such a phase once or twice.

If the estimated detection periods and mass ranges are roughly correct, and our completeness is relatively high, there are two interesting implications for both populations. First, these high optical depth phases represent a negligible fraction of the post-main sequence lifetimes of these stars, at most lasting a few thousand years. This implies that these events have to be associated with special periods in the evolution of the stars. The number of such events a star experiences is also small, one or two, not ten or twenty. Second, while a significant amount of mass is lost in the eruptions, they cannot be a dominant contribution to mass loss. For these high mass stars, standard models (e.g., Maeder 1981; Maeder & Meynet 1987, 1988; Stothers & Chin 1996; Meynet et al. 1994) typically strip the stars of their hydrogen envelopes and beyond, implying total mass losses of all but the last 5-10$M_\odot$. The median mass loss in Figure 5.9 is $M_e \sim 0.5 M_\odot$ and if every star underwent two eruptions, the typical total would be $N_e M_e \sim M_\odot$. Clearly there are some examples that require significantly larger M_e, but we simply do not find enough heavily obscured stars for this phase to represent more than a modest fraction of the total mass loss ($\sim 10\%$ not $\sim 50\%$).

For the stars similar to IRC+10420, this is consistent with the picture that the photospheres of blue-ward evolving Red Super Giants (RSGs) with $\log(L_*/L_\odot) = 5.6 \sim 6.0$ and $T_{star} \simeq$ 7000-12500 K, become moderately unstable, leading to periods of lower effective temperature and enhanced mass loss as the stars try to evolve into a “prohibited” region of the HR diagram that the authors termed the “yellow void” (de Jager & Nieuwenhuijzen 1997, de Jager 1998 and Nieuwenhuijzen & de Jager 2000). In this phase, the stars lose enough mass to evolve into a hotter, less massive star on the blue side of the HR diagram. This is also the luminosity regime of the "bistability jump" in wind speeds driven by opacity changes which Smith et al. (2004) hypothesizes can explain the absence of LBVs and the existence of YHGs with high mass loss rates and dust formation (Vink 2012) in this luminosity range. In fact, Humphreys et al. (2002) propose that IRC+10420, which is identified by our selection criterion, is such a star. While these arguments supply a unique, short-lived evolutionary phase, there may be problems with the absolute scale of the mass loss, since estimates are that IRC+10420 started with a mass of $\sim 40 M_\odot$ and has lost all but $6 \sim 15 M_\odot$ (Nieuwenhuijzen & de Jager 2000; Humphreys et al. 2002).

The only other similarly unique phase in the lives of these stars is the final post-carbon ignition phase. There are now many examples of stars which have had outbursts shortly before exploding as supernovae (e.g., Pastorello et al. 2007; Mauerhan et al. 2013; Prieto et al. 2013; Pastorello et al. 2012; Ofek et al. 2013) and superluminous supernovae that are most easily explained by surrounding the star with a large amount of previously ejected mass (Smith & McCray 2007; Gal-Yam et al. 2007; Smith 2008; Kozłowski et al. 2010; Ofek et al. 2013). Powering these supernovae requires mass ejected in the last years to decades of the stellar life (Chevalier & Fransson 1994; Chugai & Danziger 2003; Smith et al. 2009b; Moriya et al. 2014, e.g.,). It seems natural to associate these events with the mass ejections of LBVs like η Car (e.g., Smith & McCray 2007; Gal-Yam & Leonard 2009). The statistical properties and masses of either of the classes of dusty stars we discuss are well-matched to the statistical requirements for explaining these interaction powered supernovae if the instability is associated with the onset of carbon burning (see Kochanek 2011b). If there is only one eruption mechanism, it must be associated with a relatively long period like carbon burning (thousands of years) rather than the shorter, later nuclear burning phases, because we observe many systems like η Car that have survived far longer than these final phases last. If the mechanism for producing the ejecta around the superluminous supernovae is associated with nuclear burning phases beyond carbon, then we must have second eruption mechanism to explain η Car or other still older LBVs surrounded by massive dusty shells. If there indeed are two mass loss mechanisms — one commencing $\gtrsim 10^3$ years from core-collapse and the other occurring in the ~ 1 year prior to core-collapse — the self-obscured stars identified in this work may very well be experiencing the earlier of these two mechanisms.

The dusty stars can be further characterized by their variability, which will help to follow the evolution of the dust. For the optically brighter examples, it may be possible to spectroscopically determine the stellar temperatures, although detailed study may only become possible with the James Webb Space Telescope (*JWST*). It is relatively easy to expand our survey to additional galaxies. For very luminous sources like η Car analogues this is probably feasible to distance of 10 Mpc, while for the lower luminosity IRC+10420 analogues this is likely only feasible at the distances of the most distant galaxies in our sample (6 Mpc). Larger galaxy samples are needed both to increase the sample of dusty luminous stars (and hopefully find a true η Car analogue!), but also to have a sample with a larger number of supernovae, or equivalently a higher star formation rate. Our estimate of the abundance of IRC+10420 analogues is limited by the small number of ccSN (3) in our sample more than by the number of dusty stars (18) identified. Finally, while we have shown that surveys for the stars are feasible using archival Spitzer data, JWST will be a far more powerful probe of these stars. The HST-like sub-arcsecond resolution even at 24 μm (Gardner et al. 2006) will be enormously useful to either greatly reduce the problem of confusion or greatly expand the survey volume. Far more important will be the ability to carry out the survey at 24μm, which will increase the time over which dust shells can be identified from hundreds of years to thousands of years, greatly improving the statistics and our ability to survey the long term evolution of these systems and the relationship between stellar eruptions and supernovae.

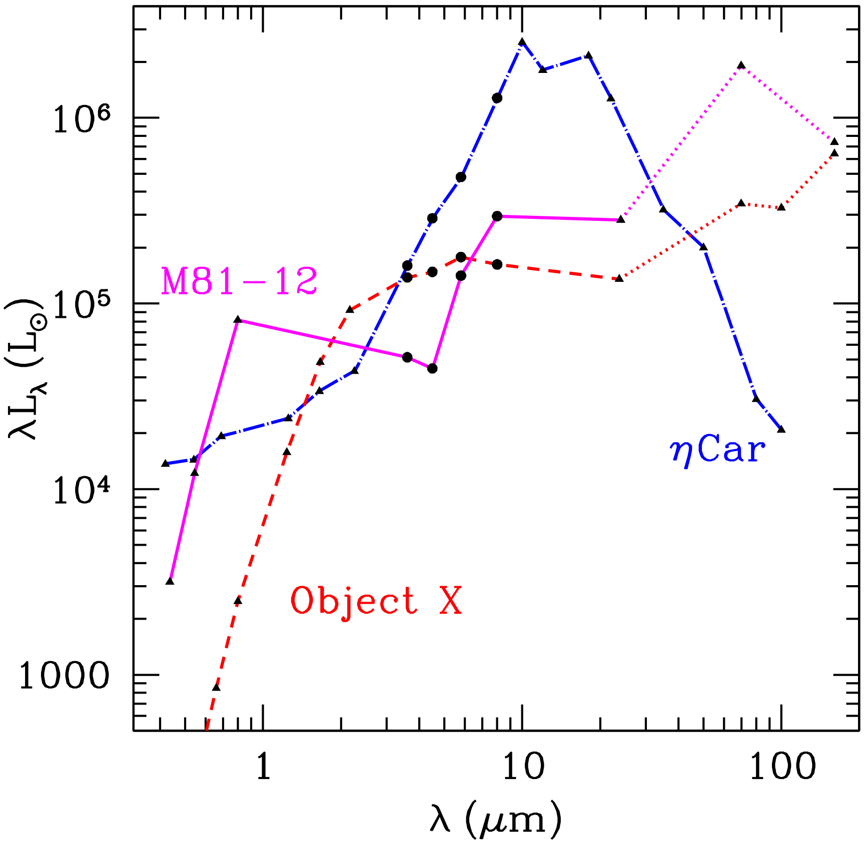

Fig. 5.1.— The spectral energy distributions (SEDs) of the dust-obscured massive star η Car (dash-dot line), "Object X" in M 33 (dashed line; Khan et al. 2011), and an obscured star in M 81 that we identify in this paper (M 81-12, solid line). All these stars have SEDs that are flat or rising in the *Spitzer* IRAC 3.6, 4.5, 5.8 and 8.0 μm bands (marked here by solid circles). The three shortest wavelength data-points of the M 81-12 SED are from HST BVI images. The 24 μm measurements of both Object X and M 81-12 are from *Spitzer* MIPS while the dotted segments of their SEDs show the *Herschel* PACS 70, 100, and 160 μm upper limits.

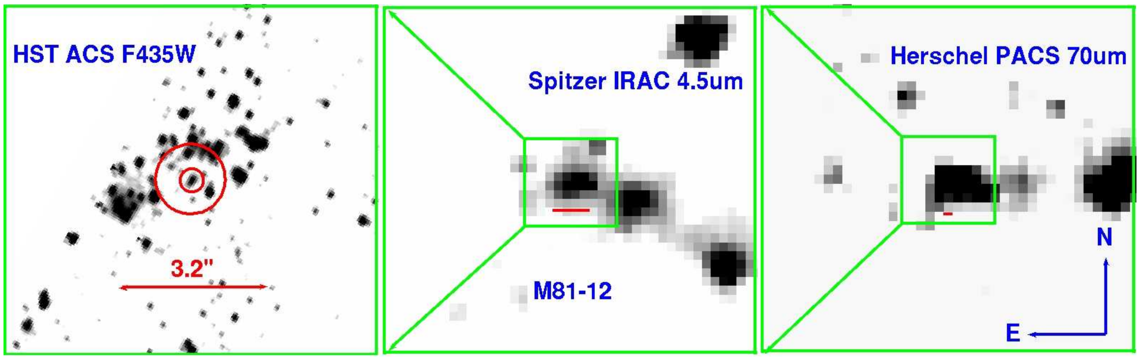

Fig. 5.2.— The *Hubble*, *Spitzer*, and *Herschel* images of the region around M 81-12. In the left panel, the radii of the circles are 0.″25 (5 ACS pixels) and 1.″43 (IRAC 4.5 μm PSF FWHM), and the source at the position of the smaller circle in the left panel is the brightest red point source on the CMD (Figure 5.4, *left* panel). The red line in each panel is the size of a PACS pixel (3.″2).

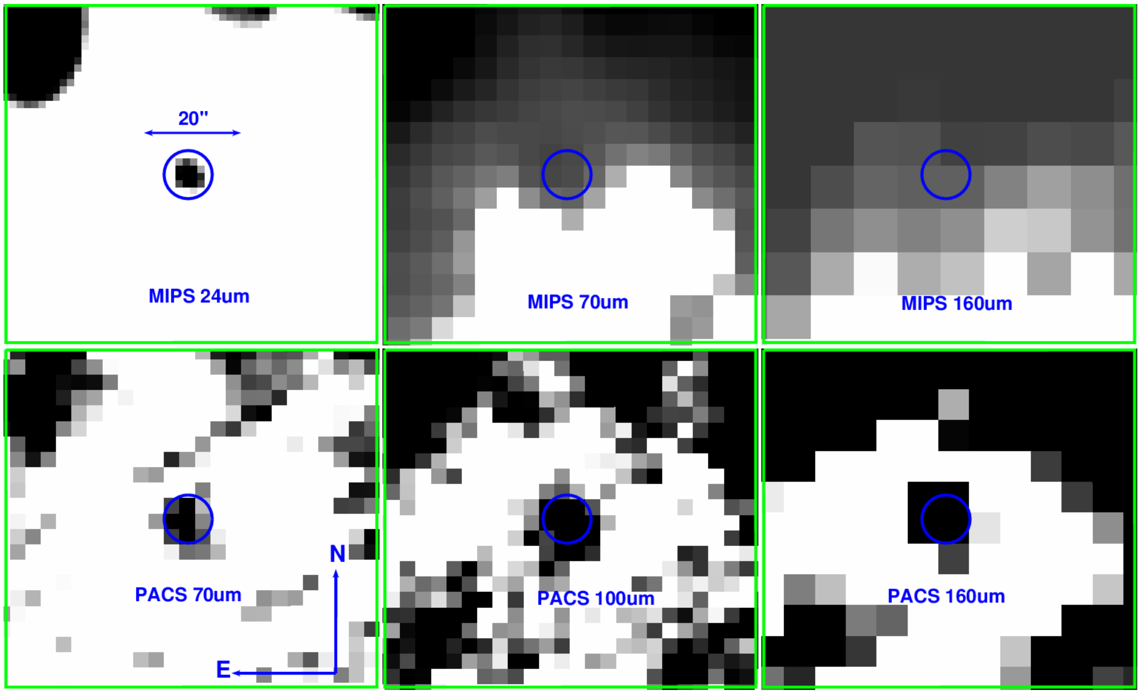

Fig. 5.3.— The *Spitzer* MIPS 24, 70 and 160 μm (top row) and *Herschel* PACS 70, 100 and 160 μm (bottom row) images of the region around the object N7793-9. The higher resolution of the PACS images helps us set tighter limits on the far-IR emission from the candidates.

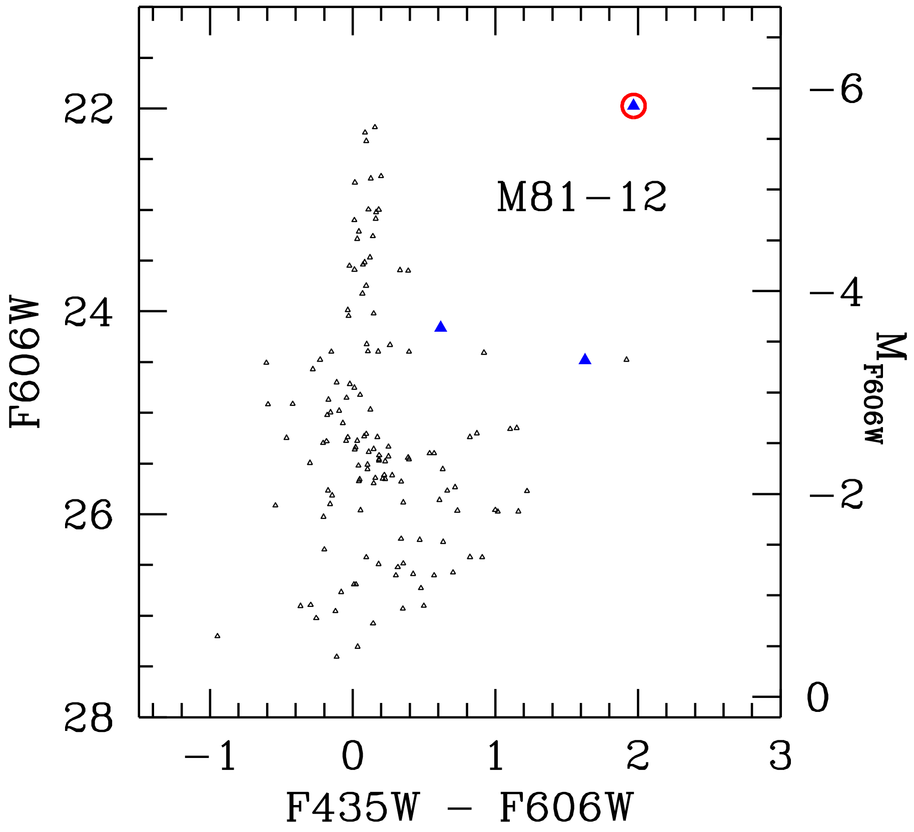

Fig. 5.4.— The $F606W$ (V) vs. $F435W - F606W$ ($B - V$) color magnitude diagram (CMD) for all HST point sources around M 81-12. The three large solid triangles denote sources located with the $0\farcs3$ matching radius. The small open triangles show all other sources within a larger $2\farcs0$ radius to emphasize the absence of any other remarkable sources nearby. The circle marks the source at the position of the smaller circle in the left panel of Figure 5.2, which is the brightest red point source on the CMD. The excellent ($< 0\farcs1$) astrometric match and the prior that very red sources are rare confirms that this source is the optical counterpart of the mid-IR bright red *Spitzer* source.

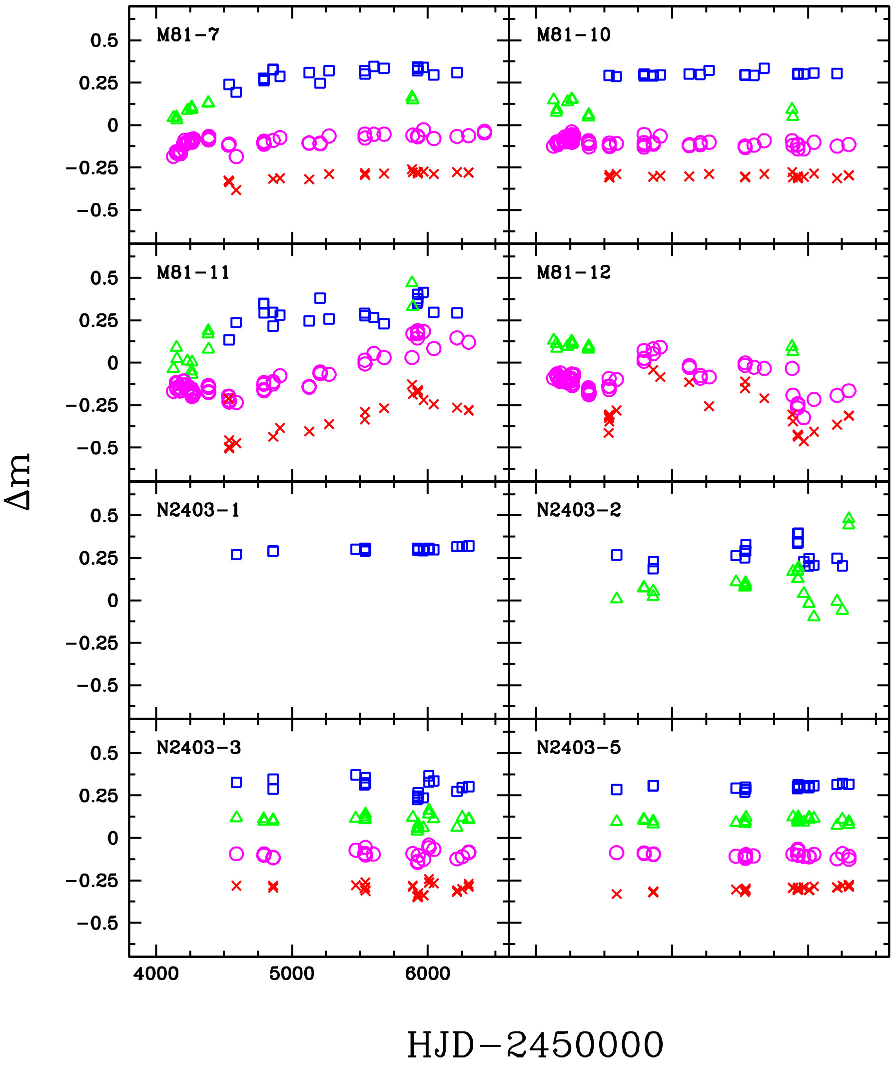

Fig. 5.5.— The differential light curves of some of the candidates in M 81 and NGC 2403 obtained from the Large Binocular Telescope. The data spans the period from March 2008 to January 2013. The *U* (squares), *B* (triangles), *V* (circles), *R* (crosses) differential magnitudes are offset by +0.3, +0.1, −0.1, −0.3 mag for clarity.

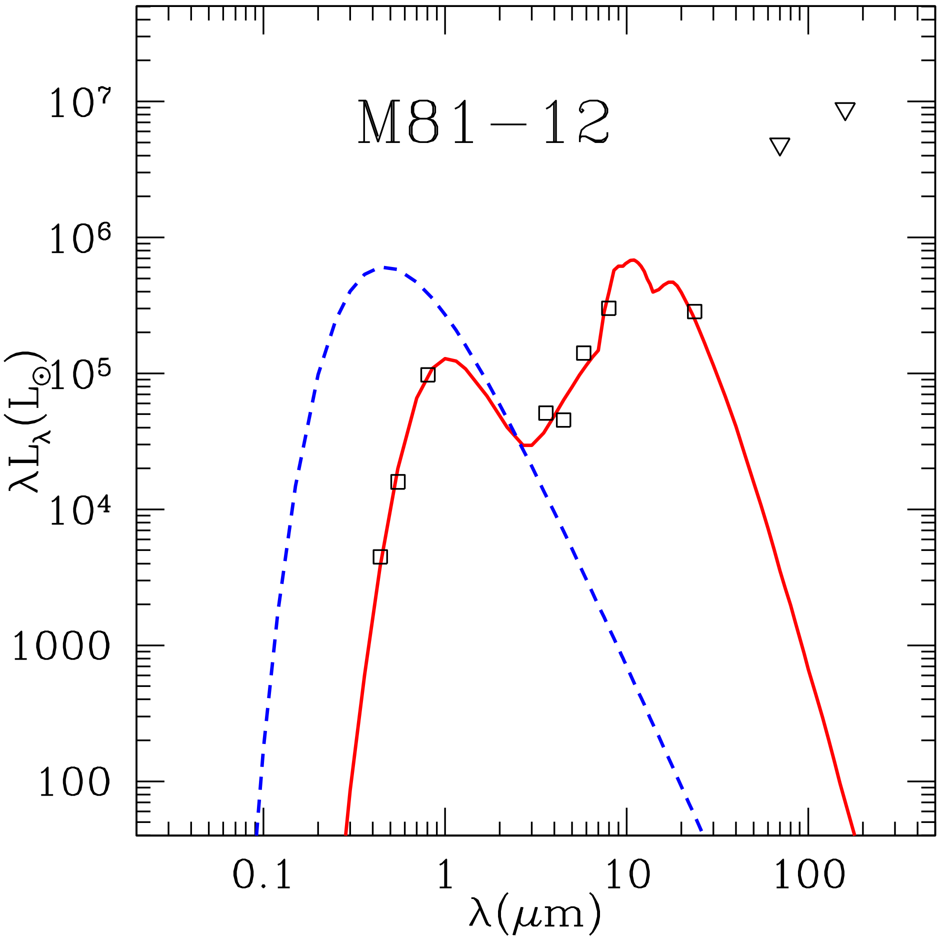

Fig. 5.6.— The best fit SED model for M 81-12. The solid line shows the best fit model of the observed SED, and the dashed line shows the SED of the underlying, unobscured star. The best fit is for a $L_* \simeq 10^{5.9}\,L_\odot$, $T_* \simeq 7900\,K$ star obscured by $\tau \simeq 8$, $T_d \simeq 530\,K$ silicate dust shell at $R_{in} = 10^{16.1}$ cm.

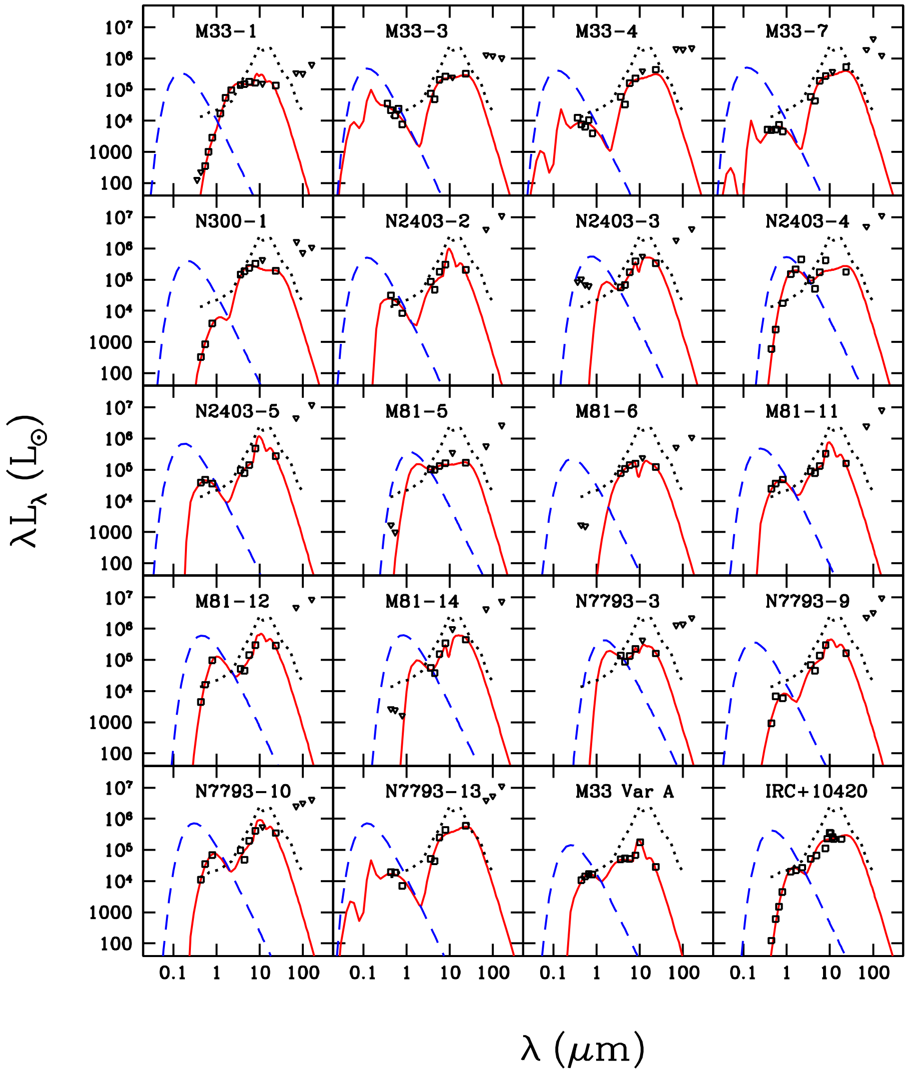

Fig. 5.7.— Same as Figure 5.6, but showing all the obscured stars that we identified as compared to M 33 Var A, *IRC* + 10420, and η Car. The solid line shows the best fit model of the observed SED, and the dashed line shows the SED of the underlying, unobscured star. M 33 Var A and *IRC* + 10420 are shown on separate panel while η Car is shown on every panel (dotted line).

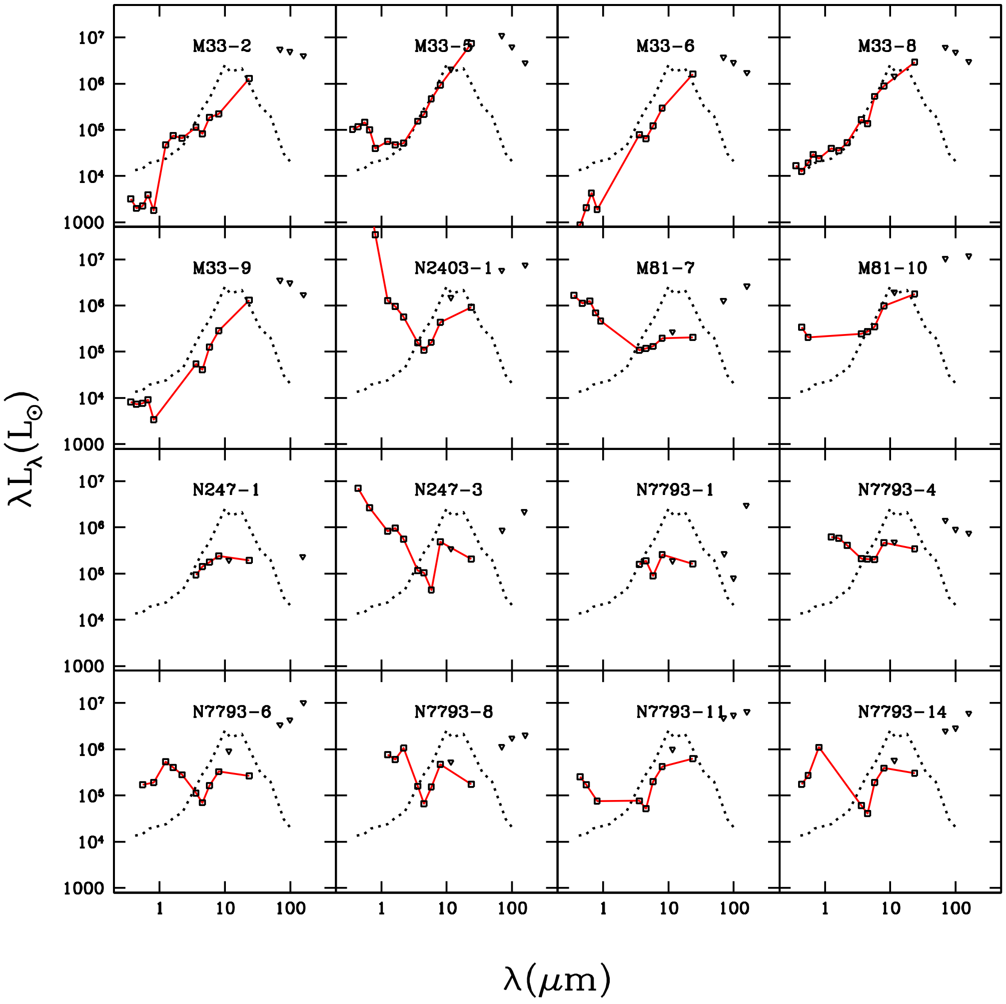

Fig. 5.8.— The SEDs of the 16 candidates that we concluded are not stars as compared to η Car (dotted line).

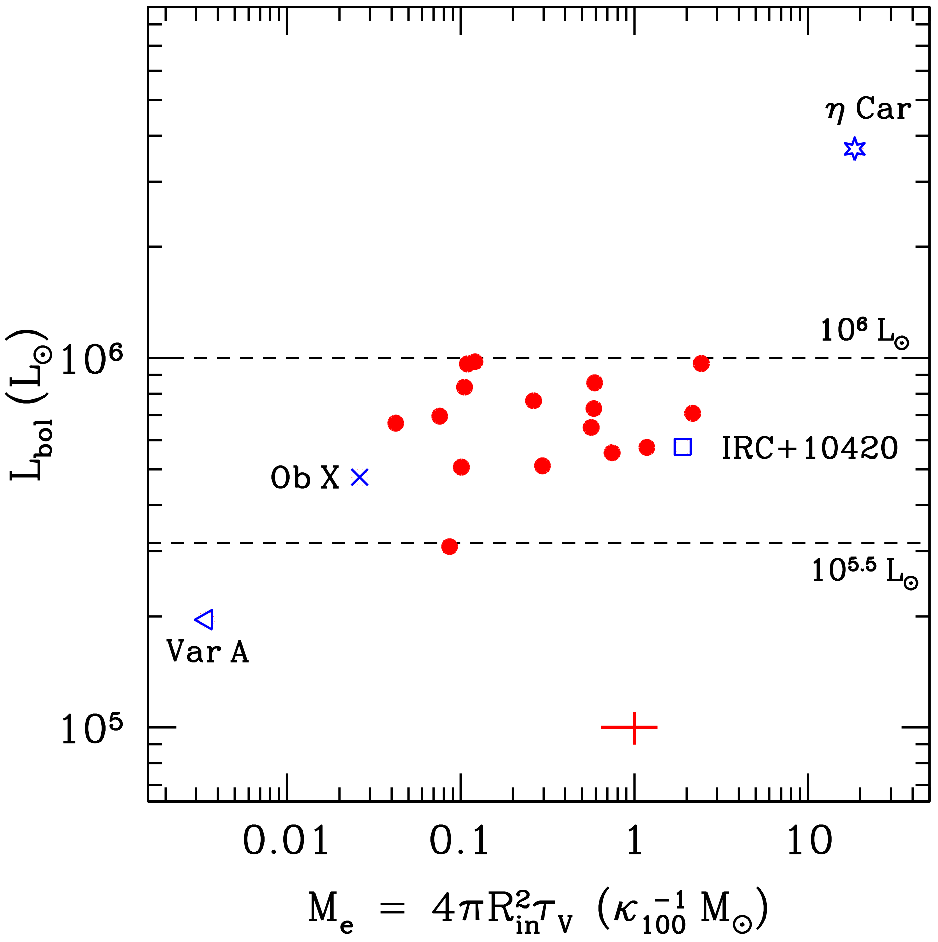

Fig. 5.9.— Luminosities of the obscured stars as a function of the estimated ejecta mass determined from the best fit model for each SED. The dashed lines enclose the luminosity range $\log(L/L_{sun}) \simeq 5.5-6.0$. We do not show N 7793-3 for which we have no optical or near-IR data. $IRC+10420$ (square), M 33 Var A (triangle), and η Car (star symbol) are shown for comparison. The error bar corresponds to the typical 1σ uncertainties on L_{bol} (±10%) and M_e (±35%).

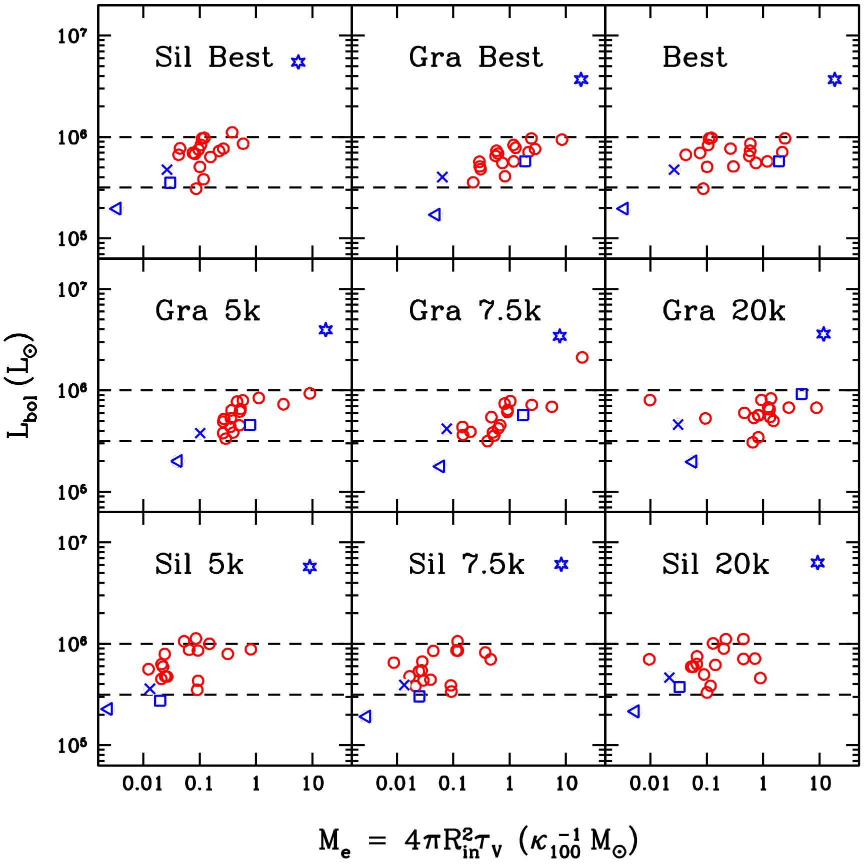

Fig. 5.10.— Same as Figure 5.9, but for different dust types and temperature assumptions. The top row shows the best silicate (left), graphitic (center), and the better of the two (right, same as Figure 5.9) models. The middle and bottom rows show the best fit models for graphitic and silicate dust at fixed stellar temperatures of 5000 K, 7500 K and 20000 K. The only higher luminosity case in the fixed temperature model panels is N 7793-13, for which the best fit models have significantly smaller χ^2 and lower luminosities for both dust types.

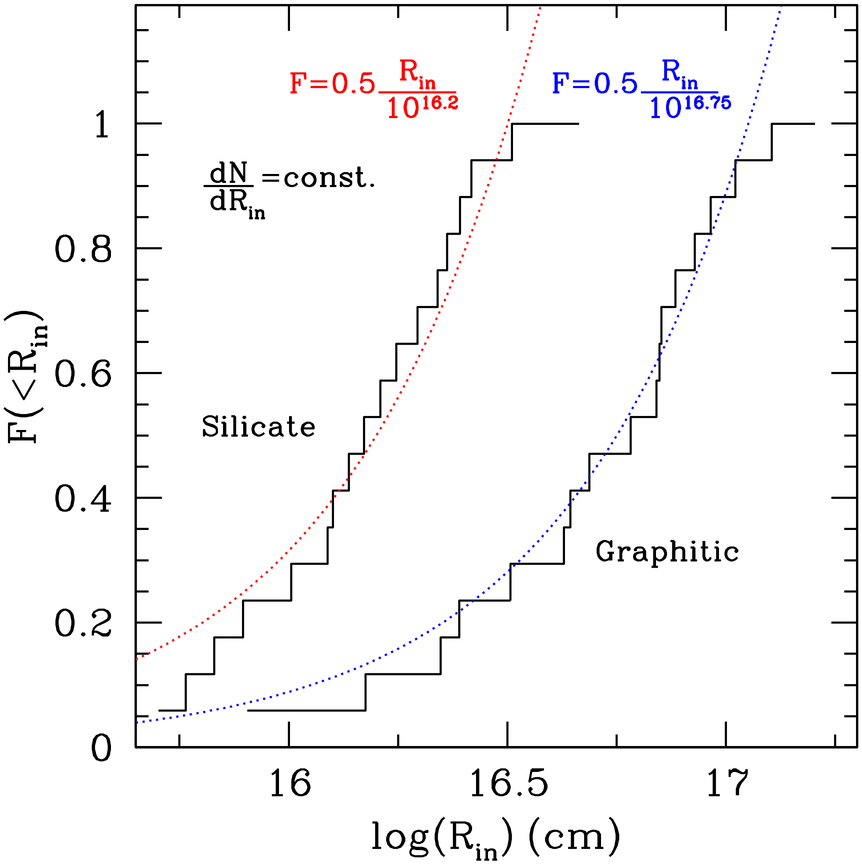

Fig. 5.11.— Cumulative histogram of the dust shell radius R_{in} for the newly identified stars excluding N 7793-3. The dotted lines, normalized to the point where $F(< R_{in}) = 0.5$, shows the distribution expected for shells in uniform expnsion observed at a random time.

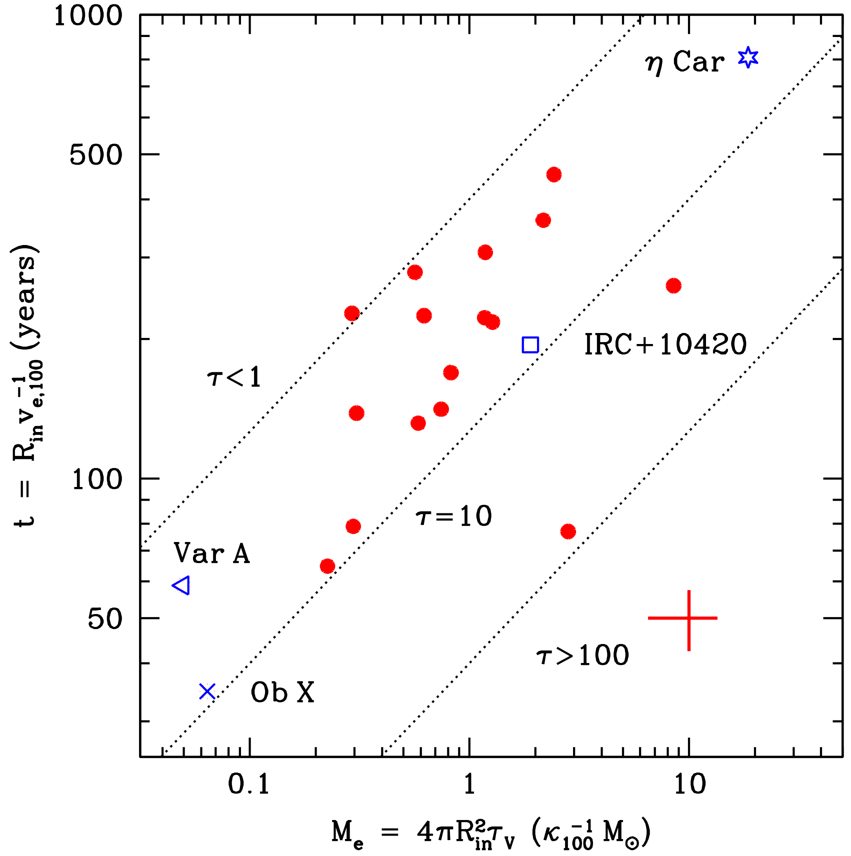

Fig. 5.12.— Elapsed time $t = R_{in}v_{e,100}^{-1}$ as a function of the estimated ejecta mass M_e for the best fit graphitic models. The mass and radius are scaled to $\kappa_V = 100\,\kappa_{100}\,\mathrm{cm}^2\,\mathrm{gm}^{-1}$ and $v_e = 100\,v_{e,100}\,\mathrm{km\,s}^{-1}$, and can be rescaled as $t \propto v_e^{-1}$ and $M_e \propto \kappa_V^{-1}$. The error bar shows the typical 1σ uncertainties on t ($\pm 15\%$) and M_e ($\pm 35\%$). The three dotted lines correspond to optical depths $\tau_V = 1, 10$ and 100. We should have trouble finding sources with $\tau_V < 1$ due to lack of mid-IR emission and $\tau_V \gtrsim 100$ due to the dust photosphere being too cold (peak emission in far-IR). The large t estimate for η Car when scaled by $v_{e,100}$ is due to the anomalously large ejecta velocities ($\sim 600\mathrm{km\,s}^{-1}$ along the long axis (Cox et al. 1995; Smith 2006)) compared to typical LBV shells ($\sim 50\mathrm{km\,s}^{-1}$, Tiffany et al. 2010).

Table 5.1:: PACS Aperture Definitions

Band (μm)	Pixel Scale	R_{ap}	R_{in}	R_{out}	Ap. Corr.
70 μm	$3''.2$	$6''.4$	$60''.8$	$70''.4$	0.72^{-1}
100 μm	$3''.2$	$6''.4$	$60''.8$	$70''.4$	0.69^{-1}
160 μm	$6''.4$	$12''.8$	$121''.6$	$140''.8$	0.78^{-1}

Table 5.2:: Optical and Near-IR Photometry[a]

ID	U	B	V	R	I	J	H	K_s
M 33 – 1	< 24.1	< 24.3	23.15	21.61	19.99	17.07	15.04	13.60
M 33 – 2	20.61	21.84	21.14	20.13	20.48	15.96	14.68	14.02
M 33 – 3	18.00	19.26	19.10	18.16	18.92	...	...	...
M 33 – 4	19.14	20.37	20.00	19.08	19.62	...	...	...
M 33 – 5	16.84	17.43	16.62	16.62	17.12	15.77	15.17	14.28
M 33 – 6	22.17	22.73	21.23	20.04	20.42	...	...	...
M 33 – 7	20.09	20.84	20.25	19.45	19.48	...	...	...
M 33 – 8	18.81	19.85	18.81	17.94	17.68	16.15	15.49	14.25
M 33 – 9	19.60	20.42	19.81	19.22	19.80	...	...	...

Continued on next page

Table 5.2 – continued from previous page

ID	U	B	V	R	I	J	H	K_s
N 300 − 1	…	25.23	23.68	…	21.13	…	…	…
N 2403 − 1	…	9.23	…	11.04	12.28	14.89	14.42	14.21
N 2403 − 2	…	21.3	21.3	…	21.3	…	…	…
N 2403 − 3	< 19.5	< 20.0	< 19.9	< 19.6	…	…	…	…
N 2403 − 4	…	25.6	23.5	…	20.5	17.21	16.05	14.45
N 2403 − 5	…	21.1	20.3	…	19.7	…	…	…
M 81 − 5	…	< 25	< 25	…	…	…	…	…
M 81 − 6	…	< 25	< 24.5	…	…	…	…	…
M 81 − 7[b]	17.55	17.57	17.09	17.46	17.66	…	…	…
M 81 − 10	…	19.25	19.20	…	…	…	…	…

Continued on next page

Table 5.2 – continued from previous page

ID	U	B	V	R	I	J	H	K_s
M 81 − 11	...	22.10	21.10	...	19.83	...	...	...
M 81 − 12	...	23.95	21.98	...	19.07	...	...	...
M 81 − 14	...	< 24.5	< 24	...	< 23.5	...	...	...
N 247 − 1	...	...	...	...	...	...	...	...
N 247 − 3	...	15.73	...	15.87	...	15.73	14.79	14.58
N 7793 − 1	...	...	...	...	...	...	...	...
N 7793 − 3	...	...	...	...	...	...	...	...
N 7793 − 4	...	...	...	...	...	16.30	15.59	15.17
N 7793 − 6	...	...	19.5	...	18.5	16.45	15.98	15.58
N 7793 − 8	...	...	...	...	...	16.07	15.56	14.14

Continued on next page

Table 5.2 – continued from previous page

ID	U	B	V	R	I	J	H	K_s
N 7793 − 9	…	25.7	23.0	…	22.3	…	…	…
N 7793 − 10	…	23.0	21.2	…	19.6	…	…	…
N 7793 − 11	…	19.6	19.5	…	19.5	…	…	…
N 7793 − 12	…	…	…	…	…	…	…	…
N 7793 − 13	…	22.4	21.9	…	22.1	…	…	…
N 7793 − 14	…	20.0	19.0	…	16.6	…	…	…

Table 5.3:: Mid and Far IR Photometry[a]

ID	[3.6]	[4.5]	[5.8]	[8.0]	[12]	[24]	[70]	[100]	[160]
M 33 − 1	11.73	10.92	9.97	9.08	7.85	5.71	278.1	377.1	1181
M 33 − 2	11.93	11.56	9.91	8.75	...	3.27	4503	5791	7501
M 33 − 3	12.39	12.11	9.80	8.56	7.35	4.75	1064	1407	1916
M 33 − 4	12.66	12.54	10.07	8.71	6.84	4.44	1648	2249	4017
M 33 − 5	11.61	10.51	8.91	7.20	5.06	1.38	8959	7250	5237
M 33 − 6	12.33	11.83	10.37	8.43	...	3.03	3026	3338	3250
M 33 − 7	12.68	12.26	9.89	8.52	6.91	4.22	1548	4955	2329
M 33 − 8	11.52	11.01	8.78	7.25	5.44	2.38	4955	5581	5607
M 33 − 9	12.74	12.31	10.33	8.48	...	3.24	2875	3590	3206

Continued on next page

Table 5.3 – continued from previous page

ID	[3.6]	[4.5]	[5.8]	[8.0]	[12]	[24]	[70]	[100]	[160]
N 300 − 1	13.22	12.23	11.22	9.91	8.33	6.90	0.96^{r}	200.1	475
N 2403 − 1	14.10	13.79	12.60	10.54	7.93	6.15	465.4	...	1385
N 2403 − 2	14.77	14.67	12.47	10.91	...	7.77	330.4	...	2045
N 2403 − 3	15.22	14.28	12.51	10.65	8.98	7.22	148.4	...	790.5
N 2403 − 4	14.65	14.60	12.50	10.59	...	7.94	408.8	...	2100
N 2403 − 5	14.64	14.13	12.74	10.41	...	7.45	369.4	...	2230
M 81 − 5	14.93	14.25	13.16	11.99	9.86	8.36	32.7	...	346.7
M 81 − 6	15.26	14.18	13.09	12.03	10.26	8.72	30.1	...	142.1
M 81 − 7	14.89	14.07	13.19	11.78	10.15	8.15	72.4	...	343.8
M 81 − 10	14.00	13.15	12.13	10.02	8.00	5.80	589.2	...	1534

Continued on next page

Table 5.3 – continued from previous page

ID	[3.6]	[4.5]	[5.8]	[8.0]	[12]	[24]	[70]	[100]	[160]
M 81 − 11	15.09	14.50	13.17	11.22	. . .	8.42	142.3	. . .	1067
M 81 − 12	15.70	15.10	13.10	11.31	. . .	7.79	275.6	. . .	1141
M 81 − 14	15.61	15.30	13.01	8.74	. . .	7.31	243.1	. . .	966.3
N 247 − 1	15.04	13.86	12.87	11.56	10.51	8.23	. . .	. . .	1.84^{r}
N 247 − 3	14.80	14.20	14.38	10.80	9.88	8.14	2.98^{r}	. . .	-0.59^{r}
N 7793 − 1	14.72	13.79	13.85	11.74	10.79	8.65	4.49^{r}	5.142	-0.69^{r}
N 7793 − 3	14.89	14.64	13.42	11.89	9.92	8.67	57.9	89.61	228.2
N 7793 − 4	14.40	13.70	12.97	11.08	9.77	7.85	63.7	58.18	76.83
N 7793 − 6	15.09	14.88	13.19	11.47	9.09	8.12	152.1	267.7	1044
N 7793 − 8	14.72	14.93	13.27	11.08	9.67	8.58	50.9	111.8	207.2

Continued on next page

Table 5.3 – continued from previous page

ID	[3.6]	[4.5]	[5.8]	[8.0]	[12]	[24]	[70]	[100]	[160]
N 7793 – 9	15.65	15.38	13.40	11.57	. . .	8.64	103.6	210.1	989.7
N 7793 – 10	15.26	15.29	13.00	11.23	9.62	7.83	114.0	205.1	426.1
N 7793 – 11	15.51	15.20	12.98	11.20	8.98	7.20	213.5	349.9	669.1
N 7793 – 12	15.89	15.37	13.58	11.57	. . .	7.84	63.3	121.0	666.7
N 7793 – 13	15.92	15.39	12.72	11.15	. . .	7.25	176	345.4	1141
N 7793 – 14	15.77	15.47	13.02	11.28	9.58	7.97	111.4	185.2	614.8

Table 5.4:: Best Fit Graphitic Models Obtained wth the MCMC Driver

ID	χ^2	τ_V	T_d (K)	T_* (K)	$\log(R_{in})$ (cm)	$\log L_*$ ($L_\odot$)	M_e ($M_\odot$)	t_e (years)
M 33 − 1	46	8.46	708	6749	16.04	5.60	0.026	34.79
M 33 − 3	34	1.16	416	29927	16.94	5.81	0.096	278.5
M 33 − 4	47	2.00	390	29977	16.99	5.76	0.156	307.3
M 33 − 7	29	2.67	381	29931	17.06	5.85	0.222	360.5
N 300 − 1	4	5.97	506	17129	16.65	5.74	0.083	141.1
N 2403 − 2	30	0.90	440	29988	16.85	5.76	0.076	227

Continued on next page

Table 5.4 – continued from previous page

ID	χ^2	τ_V	T_d	T_*	$\log(R_{in})$	$\log L_*$	M_e	t_e
			(K)	(K)	(cm)	$(L_\odot)$	$(M_\odot)$	(years)
N 2403 – 3	8	76.36	455	2533	16.38	5.88	0.263	76.89
N 2403 – 4	100	5.39	398	3790	16.62	5.86	0.045	131.7
N 2403 – 5	27	1.97	429	16146	16.85	5.84	0.109	224.6
M 81 – 5	1	7.60	428	3050	16.40	5.71	0.117	78.89
M 81 – 6	0	8.61	504	4897	16.31	5.55	0.086	64.76
M 81 – 11	17	2.56	463	10825	16.64	5.68	0.042	138.4
M 81 – 12	12	4.31	365	5548	16.84	5.89	0.105	217.5
M 81 – 14	14	20.08	341	4839	16.91	5.97	0.591	260.4
N 7793 – 3	...	...	...	...	...	...	...	...

Continued on next page

Table 5.4 – continued from previous page

ID	χ^2	τ_V	T_d	T_*	$\log{(R_{in})}$	$\log L_*$	M_e	t_e
			(K)	(K)	(cm)	$(L_\odot)$	$(M_\odot)$	(years)
N 7793 − 9	46	4.61	432	14632	16.73	5.61	0.101	169.2
N 7793 − 10	32	3.80	396	7406	16.85	5.92	0.121	222.3
N 7793 − 13	32	1.90	369	29943	17.15	5.99	0.377	452.2
IRC+10420	222	8.06	399	8157	16.79	5.76	0.030	194.2
M 33 Var A	43	2.29	536	11741	16.27	5.23	0.003	58.86
η Car	490	4.55	361	18134	17.41	6.57	5.611	809

Table 5.5:: Best Fit Silicate Models Obtained wth the MCMC Driver

ID	χ^2	τ_V	T_d	T_*	$\log{(R_{in})}$	$\log L_*$	M_e	t_e
			(K)	(K)	(cm)	$(L_\odot)$	$(M_\odot)$	(years)
M 33 − 1	18	10.70	1218	24602	15.80	5.68	0.064	19.8
M 33 − 3	55	2.63	649	29955	16.38	5.88	0.565	76.21
M 33 − 4	75	3.88	599	29991	16.40	5.80	1.182	80.14
M 33 − 7	57	4.79	599	29973	16.43	5.86	2.170	85.98
N 300 − 1	8	8.57	959	28956	16.09	5.83	0.744	39.24
N 2403 − 2	26	2.56	676	29942	16.34	5.84	0.292	68.79

Continued on next page

Table 5.5 – continued from previous page

ID	χ^2	τ_V	T_d (K)	T_* (K)	$\log(R_{in})$ (cm)	$\log L_*$ ($L_\odot$)	M_e ($M_\odot$)	t_e (years)
N 2403 − 3	2	25.27	499	4981	16.11	5.88	2.821	40.8
N 2403 − 4	146	10.00	568	4545	15.93	5.89	0.585	26.78
N 2403 − 5	5	3.56	662	20750	16.34	5.98	0.621	70.06
M 81 − 5	2	35.00	1117	29778	15.86	5.58	0.296	23.14
M 81 − 6	0	46.97	985	13885	15.73	5.49	0.226	17.15
M 81 − 11	3	4.54	746	15015	16.09	5.82	0.307	38.59
M 81 − 12	10	7.84	529	7910	16.16	5.92	1.275	46.34
M 81 − 14	8	29.47	416	4528	16.25	5.93	8.513	56.65
N 7793 − 3	. . .	. . .	. . .	. . .	. . .	. . .	. . .	. . .

Continued on next page

Table 5.5 – continued from previous page

ID	χ^2	τ_V	T_d	T_*	$\log{(R_{in})}$	$\log{L_*}$	M_e	t_e
			(K)	(K)	(cm)	($L_\odot$)	($M_\odot$)	(years)
N 7793 − 9	27	7.04	713	22072	16.18	5.70	0.825	47.86
N 7793 − 10	25	6.36	609	12175	16.24	5.99	1.174	55.18
N 7793 − 13	42	4.01	546	29989	16.59	6.05	2.431	122.6
IRC+10420	240	11.86	835	11780	15.80	5.55	1.900	20.17
M 33 Var A	8	4.11	1046	14549	15.56	5.29	0.050	11.54
η Car	853	7.99	468	26164	17.02	6.74	18.615	335.1

Table 5.6:: Best Fit Models for 5000 K Graphitic Dust

ID	τ_V	T_d	$\log(R_{in})$	$\log L_*$	M_e
		(K)	(cm)	($L_\odot$)	($M_\odot$)
M 33 − 1	8.17	595	16.15	5.58	0.102
M 33 − 3	2.50	400	16.61	5.69	0.261
M 33 − 4	3.14	400	16.56	5.58	0.260
M 33 − 7	3.69	400	16.59	5.64	0.351
N 300 − 1	6.52	501	16.41	5.72	0.271
N 2403 − 2	3.13	401	16.63	5.72	0.358
N 2403 − 3	18.58	404	16.71	5.86	3.070
N 2403 − 4	5.91	400	16.74	5.93	1.121

Continued on next page

Table 5.6 – continued from previous page

ID	τ_V	T_d (K)	$\log(R_{in})$ (cm)	$\log L_*$ $(L_\odot)$	M_e $(M_\odot)$
N 2403 − 5	2.78	400	16.71	5.89	0.460
M 81 − 5	14.32	514	16.32	5.58	0.393
M 81 − 6	14.55	535	16.25	5.52	0.289
M 81 − 11	2.81	406	16.66	5.80	0.369
M 81 − 12	3.77	399	16.67	5.79	0.518
M 81 − 14	21.78	350	16.91	5.97	9.040
N 7793 − 3	. . .	. . .	. . .	. . .	. . .
N 7793 − 9	7.50	400	16.61	5.66	0.506
N 7793 − 10	2.73	500	16.19	5.30	0.584

Continued on next page

Table 5.6 – continued from previous page

ID	τ_V	T_d (K)	$\log{(R_{in})}$ (cm)	$\log L_*$ ($L_\odot$)	M_e ($M_\odot$)
N 7793 − 13	5.74	300	17.34	6.60	0.528
IRC+10420	5.08	401	16.60	5.66	0.782
M 33 Var A	3.37	400	16.72	5.90	0.041
η Car	3.67	400	16.68	5.82	17.258

Table 5.7:: Best Fit Models for 7500 K Graphitic Dust

ID	τ_V	T_d (K)	$\log{(R_{in})}$ (cm)	$\log L_*$ ($L_\odot$)	M_e ($M_\odot$)
M 33 − 1	8.05	701	16.09	5.62	0.077
M 33 − 3	2.67	460	16.54	5.59	0.202
M 33 − 4	3.52	400	16.68	5.58	0.507
M 33 − 7	4.11	400	16.71	5.66	0.679
N 300 − 1	6.89	504	16.52	5.74	0.475
N 2403 − 2	2.99	493	16.45	5.56	0.149
N 2403 − 3	9.41	405	16.81	5.86	2.466
N 2403 − 4	7.09	300	17.32	6.33	19.435

Continued on next page

Table 5.7 – continued from previous page

ID	τ_V	T_d (K)	$\log(R_{in})$ (cm)	$\log L_*$ ($L_\odot$)	M_e ($M_\odot$)
N 2403 – 5	2.96	400	16.82	5.87	0.812
M 81 – 5	16.83	548	16.35	5.55	0.530
M 81 – 6	16.18	559	16.30	5.50	0.405
M 81 – 11	2.67	498	16.47	5.64	0.146
M 81 – 12	3.99	400	16.78	5.79	0.910
M 81 – 14	21.43	400	16.81	5.84	5.613
N 7793 – 3	...	...	...	...	...
N 7793 – 9	8.00	400	16.77	5.76	0.629
N 7793 – 10	2.74	500	16.27	5.25	1.030

Continued on next page

Table 5.7 – continued from previous page

ID	τ_V	T_d (K)	$\log(R_{in})$ (cm)	$\log L_*$ ($L_\odot$)	M_e ($M_\odot$)
N 7793 − 13	5.89	400	17.16	6.53	0.923
IRC+10420	5.25	424	16.64	5.63	1.743
M 33 Var A	3.59	400	16.83	5.89	0.060
η Car	3.86	400	16.79	5.81	7.732

Table 5.8:: Best Fit Models for 20000 K Graphitic Dust

ID	τ_V	T_d (K)	$\log(R_{in})$ (cm)	$\log L_*$ ($L_\odot$)	M_e ($M_\odot$)
M 33 – 1	5.88	900	15.96	5.66	0.031
M 33 – 3	1.89	400	16.92	5.76	0.821
M 33 – 4	4.53	614	16.26	5.72	0.094
M 33 – 7	3.18	400	16.91	5.74	1.321
N 300 – 1	5.47	500	16.69	5.75	0.824
N 2403 – 2	1.89	408	16.88	5.73	0.683
N 2403 – 3	6.55	417	16.92	5.83	2.849
N 2403 – 4	4.92	1182	15.75	5.91	0.010

Continued on next page

Table 5.8 – continued from previous page

ID	τ_V	T_d (K)	$\log{(R_{in})}$ (cm)	$\log L_*$ ($L_\odot$)	M_e ($M_\odot$)
N 2403 − 5	1.55	400	16.99	5.91	0.928
M 81 − 5	19.68	587	16.41	5.54	0.817
M 81 − 6	13.09	558	16.45	5.49	0.653
M 81 − 11	1.47	432	16.85	5.78	0.463
M 81 − 12	2.59	400	16.95	5.81	1.295
M 81 − 14	22.28	430	16.90	5.83	8.834
N 7793 − 3	…	…	…	…	…
N 7793 − 9	7.00	402	17.02	5.96	1.516
N 7793 − 10	1.12	500	16.45	5.30	1.371

Continued on next page

Table 5.8 – continued from previous page

ID	τ_V	T_d (K)	$\log(R_{in})$ (cm)	$\log L_*$ ($L_\odot$)	M_e ($M_\odot$)
N 7793 − 13	4.29	400	17.32	6.55	1.224
IRC+10420	4.00	400	16.89	5.70	4.823
M 33 Var A	2.18	400	17.00	5.92	0.056
η Car	2.45	400	16.95	5.83	11.767

Table 5.9:: Best Fit Models for 5000 K Silicate Dust

ID	τ_V	T_d (K)	$\log(R_{in})$ (cm)	$\log L_*$ ($L_\odot$)	M_e ($M_\odot$)
M 33 − 1	14.42	816	15.58	5.56	0.013
M 33 − 3	4.30	592	15.83	5.75	0.012
M 33 − 4	5.26	513	15.90	5.65	0.021
M 33 − 7	5.91	523	15.91	5.68	0.025
N 300 − 1	10.72	724	15.76	5.77	0.022
N 2403 − 2	5.56	583	15.89	5.80	0.021
N 2403 − 3	21.93	469	16.18	5.90	0.316
N 2403 − 4	9.81	505	16.09	5.93	0.093

Continued on next page

Table 5.9 – continued from previous page

ID	τ_V	T_d (K)	$\log(R_{in})$ (cm)	$\log L_*$ ($L_\odot$)	M_e ($M_\odot$)
N 2403 − 5	5.30	502	16.10	6.03	0.053
M 81 − 5	28.38	616	15.86	5.63	0.094
M 81 − 6	37.84	655	15.79	5.55	0.090
M 81 − 11	5.26	586	15.93	5.90	0.024
M 81 − 12	7.16	410	16.26	6.00	0.149
M 81 − 14	26.85	400	16.34	5.95	0.808
N 7793 − 3	...	...	...	...	...
N 7793 − 9	8.42	585	15.85	5.68	0.027
N 7793 − 10	6.24	472	16.17	6.05	0.086

Continued on next page

Table 5.9 – continued from previous page

ID	τ_V	T_d (K)	$\log{(R_{in})}$ (cm)	$\log{L_*}$ ($L_\odot$)	M_e ($M_\odot$)
N 7793 − 13	6.53	484	16.10	5.94	0.065
IRC+10420	10.99	600	15.73	5.44	0.020
M 33 Var A	5.04	793	15.44	5.36	0.002
η Car	9.94	250	17.08	6.76	9.026

Table 5.10:: Best Fit Models for 7500 K Silicate Dust

ID	τ_V	T_d (K)	$\log(R_{in})$ (cm)	$\log L_*$ ($L_\odot$)	M_e ($M_\odot$)
M 33 − 1	14.26	973	15.59	5.59	5.59
M 33 − 3	4.66	654	15.88	5.68	5.68
M 33 − 4	5.64	601	15.89	5.58	5.58
M 33 − 7	6.49	600	15.93	5.64	5.64
N 300 − 1	10.99	800	15.80	5.74	5.74
N 2403 − 2	5.66	641	15.92	5.73	5.73
N 2403 − 3	19.50	501	16.24	5.91	5.91
N 2403 − 4	9.72	1114	15.58	5.82	5.82

Continued on next page

Table 5.10 – continued from previous page

ID	τ_V	T_d (K)	$\log{(R_{in})}$ (cm)	$\log L_*$ ($L_\odot$)	M_e ($M_\odot$)
N 2403 − 5	5.35	600	16.06	5.93	5.93
M 81 − 5	28.71	705	15.85	5.59	5.59
M 81 − 6	35.40	722	15.81	5.53	5.53
M 81 − 11	5.38	650	15.96	5.83	5.83
M 81 − 12	7.33	500	16.21	5.93	5.93
M 81 − 14	25.47	496	16.23	5.85	5.85
N 7793 − 3	...	...	...	...	...
N 7793 − 9	8.67	617	15.93	5.65	5.65
N 7793 − 10	6.56	512	16.23	6.03	6.03

Continued on next page

Table 5.10 – continued from previous page

ID	τ_V	T_d (K)	$\log(R_{in})$ (cm)	$\log L_*$ ($L_\odot$)	M_e ($M_\odot$)
N 7793 − 13	6.88	500	16.21	5.93	5.93
IRC+10420	11.51	700	15.77	5.48	5.48
M 33 Var A	5.03	867	15.48	5.28	5.28
η Car	10.42	300	17.05	6.78	6.78

Table 5.11:: Best Fit Models for 20000 K Silicate Dust

ID	τ_V	T_d (K)	$\log(R_{in})$ (cm)	$\log L_*$ ($L_\odot$)	M_e ($M_\odot$)
M 33 − 1	10.86	1204	15.75	5.67	0.022
M 33 − 3	3.36	696	16.20	5.77	0.053
M 33 − 4	2.58	400	16.87	5.66	0.892
M 33 − 7	5.41	604	16.31	5.79	0.142
N 300 − 1	9.17	922	16.03	5.80	0.066
N 2403 − 2	3.65	702	16.20	5.78	0.058
N 2403 − 3	16.98	651	16.31	5.85	0.445
N 2403 − 4	7.95	1499	15.64	5.85	0.010

Continued on next page

Table 5.11 – continued from previous page

ID	τ_V	T_d (K)	$\log{(R_{in})}$ (cm)	$\log L_*$ ($L_\odot$)	M_e ($M_\odot$)
N 2403 − 5	3.41	628	16.39	6.00	0.129
M 81 − 5	24.38	913	15.94	5.59	0.116
M 81 − 6	29.17	957	15.87	5.52	0.101
M 81 − 11	3.36	702	16.25	5.88	0.067
M 81 − 12	5.62	517	16.55	6.05	0.444
M 81 − 14	21.68	601	16.36	5.85	0.715
N 7793 − 3	...	...	...	...	...
N 7793 − 9	6.80	701	16.16	5.70	0.089
N 7793 − 10	4.56	600	16.44	6.05	0.217

Continued on next page

Table 5.11 – continued from previous page

ID	τ_V	T_d (K)	$\log(R_{in})$ (cm)	$\log L_*$ ($L_\odot$)	M_e ($M_\odot$)
N 7793 − 13	4.81	589	16.41	5.95	0.200
IRC+10420	10.00	1000	15.86	5.57	0.033
M 33 Var A	2.67	962	15.75	5.33	0.005
η Car	8.49	400	17.12	6.80	9.272

Chapter 6: Summary

Massive star evolution is critical to many aspects of astrophysics, yet still poorly understood. To identify and characterize evolved massive stars, I take advantage of the enormous amount of data collected by the *Spitzer*, *HST*, and *Herschel* missions over the past decade. Since self-obscured stars with dusty envelopes reach their peak luminosities in the mid-IR, the large, publicly available, rich *Spitzer* data-sets are ideal for this research, while ancillary data from *HST* and *Herschel* are very useful for verifying the nature of the identified sources.

I have demonstrated, for the very first time, that it is possible to identify post-eruptive massive estars in galaxies beyond the local group using the mid-IR excess from warm circumstellar dust despite crowding problems created by the limited spatial resolution of *Spitzer*. I have identified 18 previously unknown luminous self-obscured extragalactic stars in galaxies up to 4 Mpc away. Only a handful of such objectss were previously known, almost all of them in the Galaxy, except for the Hubble-Sandage variable M 33 Var A.

The research presented here may have immense impact on various aspects of Astrophysics, including stellar evolution theory, determining core-collapse supernova rate, understanding the role of stellar feedback in chemical enrichment of galaxies and the metallicity evolution of our universe throughout cosmic history. I am investigating an unexplored regime of astrophysics, and I fully expected to encounter the unexpected. My identification of a large number of the “missing Luminous Blue Variables” demonstrates the discovery potential of my research.

The results of this project will be of significant interest to the astronomical community preparing for observations with *JWST*. In the long term, the sources I have identified will also be the best candidates for detailed physical analysis with *JWST* spectroscopy, just as luminous sources in the LMC were spectroscopically examined using the *Spitzer* IRS (SAGE-Spec, Woods et al. 2010). *JWST* will be more sensitive: even at 24 μm it will have sub-arcsecond resolution (Gardner et al. 2006) comparable to *HST* in the optical (see Figure 6.1). I will tackle some very interesting *JWST* science ahead of its launch utilizing existing data.

I have begun publishing detailed mid-IR point source catalogs of nearby galaxies that will have significant legacy value. The coming decade will take us through the age of 8 m class telescopes, *Gaia*, and Advanced LIGO to the era of 30 m class telescopes, JWST, and LISA. The results presented in this dissertation and the associated data products being made public will be useful for studying evolved stellar populations and compact clusters in the targeted galaxies as well as AGNs and background galaxies in the field, and become a valuable resource for planning future observing missions.

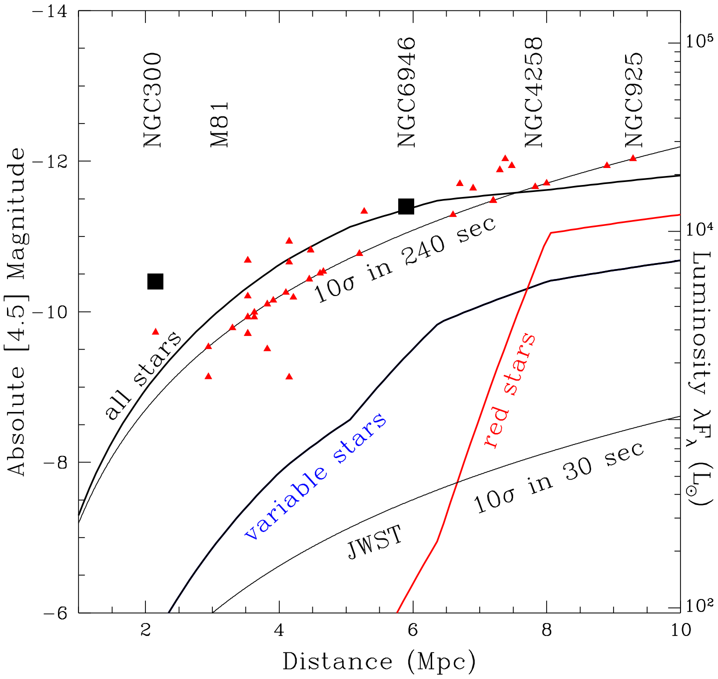

Fig. 6.1.— While *JWST* will be more sensitive, I will tackle some very interesting *JWST* science ahead of its launch utilizing existing data. Here, I compare the observing depths and crowding limits of *Spitzer* and *JWST*. As a function of target distance, the red triangles show the sensitivities of existing *Spitzer* data with acceptable depth. The solid lines show the 10σ detection limits of a 240 sec *Spitzer* IRAC 4.5μm exposure where all stars, variable stars and red stars become confused, compared to the 10σ limit for a single 30 sec exposure with the 6.5 m *JWST*.

References

Abazajian, K. N. et al. 2009, ApJS, 182, 543

Alard, C. 2000, A&AS, 144, 363

Alard, C. & Lupton, R. H. 1998, ApJ, 503, 325

Arbour, R. & Boles, T. 2008, Central Bureau Electronic Telegrams, 1234, 1

Arnett, W. D., Schramm, D. N., & Truran, J. W. 1989, ApJ, 339, L25

Ashby, M. L. N. et al. 2009, ApJ, 701, 428

Assef, R. J. et al. 2010, ApJ, 713, 970

Balog, Z. et al. 2013, Experimental Astronomy

Barmby, P. et al. 2006, ApJ Letters, 650, L45

Berger, E. et al. 2009, ApJ, 699, 1850

Bionta, R. M., Blewitt, G., Bratton, C. B., Casper, D., & Ciocio, A. 1987, Physical Review Letters, 58, 1494

Blöcker, T., Balega, Y., Hofmann, K., Lichtenthäler, J., Osterbart, R., & Weigelt, G. 1999, A&A, 348, 805

Blum, R. D. et al. 2006, AJ, 132, 2034

Bohlin, R. C., Savage, B. D., & Drake, J. F. 1978, ApJ, 224, 132

Bolatto, A. D. et al. 2007, ApJ, 655, 212

Bonanos, A. Z. et al. 2006, ApJ, 652, 313

—. 2009, AJ, 138, 1003

—. 2010, AJ, 140, 416

Bond, H. E. et al. 2009, ApJ, 695, L154

Botticella, M. T. et al. 2009, MNRAS, 398, 1041

Chevalier, R. A. & Fransson, C. 1994, ApJ, 420, 268

Chevalier, R. A. & Irwin, C. M. 2012, ApJ, 747, L17

Chiosi, C. & Maeder, A. 1986, ARA&A, 24, 329

Chugai, N. N. & Danziger, I. J. 2003, Astronomy Letters, 29, 649

Churchwell, E. et al. 2006, ApJ, 649, 759

Clark, J. S. et al. 2012, A&A, 541, A146

Conroy, C. & Gunn, J. E. 2010, ApJ, 712, 833

Conroy, C., Gunn, J. E., & White, M. 2009, ApJ, 699, 486

Conroy, C., White, M., & Gunn, J. E. 2010a, ApJ, 708, 58

—. 2010b, ApJ, 708, 58

Cox, P., Mezger, P. G., Sievers, A., Najarro, F., Bronfman, L., Kreysa, E., & Haslam, G. 1995, A&A, 297, 168

Crowther, P. A. et al. 2010, MNRAS, 408, 731

Cutri, R. M. et al. 2003, 2MASS All Sky Catalog of point sources., ed. R. M. Cutri et al.

Dalcanton, J. J. et al. 2009, ApJS, 183, 67

Dale, D. A. et al. 2009, ApJ, 703, 517

Davidson, K. 1987, ApJ, 317, 760

de Jager, C. 1998, A&A Rev., 8, 145

de Jager, C. & Nieuwenhuijzen, H. 1997, MNRAS, 290, L50

de Vaucouleurs, G. et al. 1991, Third Reference Catalogue of Bright Galaxies.

Dolphin, A. E. 2000, PASP, 112, 1383

Draine, B. T. & Lee, H. M. 1984, ApJ, 285, 89

Egan, M. P., Clark, J. S., Mizuno, D. R., Carey, S. J., Steele, I. A., & Price, S. D. 2002, ApJ, 572, 288

Elias, J. H., Frogel, J. A., & Schwering, P. B. W. 1986, ApJ, 302, 675

Elitzur, M. & Ivezić, Ž. 2001, MNRAS, 327, 403

Fazio, G. G. et al. 2004, ApJS, 154, 10

Figer, D. F., McLean, I. S., & Morris, M. 1999, ApJ, 514, 202

Filippenko, A. V. 1997, ARA&A, 35, 309

Flesch, E. 2010, *PASA*, 27, 283

Fullerton, A. W., Massa, D. L., & Prinja, R. K. 2006, ApJ, 637, 1025

Gal-Yam, A. et al. 2007, ApJ, 656, 372

Gal-Yam, A., & Leonard, D. C. 2009, Nature, 458, 865

Gardner, J. P. et al. 2006, Space Sci. Rev., 123, 485

Gehrels, N., Ramirez-Ruiz, E., & Fox, D. B. 2009, ARA&A, 47, 567

Gerke, J. R. & Kochanek, C. S. 2013, ApJ, 762, 64

Gerke, J. R., Kochanek, C. S., Prieto, J. L., Stanek, K. Z., & Macri, L. M. 2011, ApJ, 743, 176

Giallongo, E. et al. 2008, A&A, 482, 349

Gieren, W. et al. 2005, ApJ, 628, 695

—. 2006, ApJ, 647, 1056

Gogarten, S. M. et al. 2009, ApJ, 703, 300

Gordon, K. et al. 2007, in Spitzer Proposal ID #40245, 40245–+

Gordon, S. M., Duric, N., Kirshner, R. P., Goss, W. M., & Viallefond, F. 1999, ApJS, 120, 247

Gratier, P. et al. 2010, A&A, 522, A3+

Gruendl, R. A. & Chu, Y. 2009, ApJS, 184, 172

Gruendl, R. A. et al. 2008, ApJ, 688, L9

Gvaramadze, V. V., Kniazev, A. Y., & Fabrika, S. 2010, MNRAS, 405, 1047

Hartman, J. D., Bakos, G., Stanek, K. Z., & Noyes, R. W. 2004, AJ, 128, 1761

Hartman, J. D., Bersier, D., Stanek, K. Z., Beaulieu, J., Kaluzny, J., Marquette, J., Stetson, P. B., & Schwarzenberg-Czerny, A. 2006, MNRAS, 371, 1405

Heger, A., Fryer, C. L., Woosley, S. E., Langer, N., & Hartmann, D. H. 2003, ApJ, 591, 288

Higgs, L. A., Wendker, H. J., & Landecker, T. L. 1994, A&A, 291, 295

Hill, J. M., Green, R. F., & Slagle, J. H. 2006, in

Horiuchi, S., Beacom, J. F., Kochanek, C. S., Prieto, J. L., Stanek, K. Z., & Thompson, T. A. 2011, ApJ, 738, 154

Hubble, E. & Sandage, A. 1953, ApJ, 118, 353

Humphreys, R. M. & Davidson, K. 1984, Science, 223, 243

—. 1994, PASP, 106, 1025

Humphreys, R. M., Davidson, K., Jones, T. J., Pogge, R. W., Grammer, S. H., Prieto, J. L., & Pritchard, T. A. 2012, ApJ, 760, 93

Humphreys, R. M., Davidson, K., & Smith, N. 1999, PASP, 111, 1124

—. 2002, AJ, 124, 1026

Humphreys, R. M., Jones, T. J., & Gehrz, R. D. 1987, AJ, 94, 315

Humphreys, R. M. et al. 1997, AJ, 114, 2778

—. 2006, AJ, 131, 2105

Ivezic, Z. & Elitzur, M. 1997, MNRAS, 287, 799

Ivezic, Z., Nenkova, M., & Elitzur, M. 1999, arXiv:astro-ph/9910475

Jones, D. H. et al. 2009, MNRAS, 399, 683

Jones, T. J. et al. 1993, ApJ, 411, 323

Jordi, K., Grebel, E. K., & Ammon, K. 2006, A&A, 460, 339

Karachentsev, I. D. et al. 2004, AJ, 127, 2031

Kashi, A., Frankowski, A., & Soker, N. 2010, ApJ, 709, L11

Kasliwal, M. et al. 2013, Spitzer Proposal, 10136

Kennicutt, Jr., R. C. 1998, ApJ, 498, 541

Kennicutt, Jr., R. C. et al. 2003, PASP, 115, 928

—. 2008, ApJS, 178, 247

Khan, R., Stanek, K. Z., & Kochanek, C. S. 2013, ApJ, 767, 52

Khan, R., Stanek, K. Z., Kochanek, C. S., & Bonanos, A. Z. 2011, ApJ, 732, 43

Khan, R., Stanek, K. Z., Prieto, J. L., Kochanek, C. S., Thompson, T. A., & Beacom, J. F. 2010a, ApJ, 715, 1094

—. 2010b, ApJ, 715, 1094

Khan, R., Stanek, K. Z., Kochanek, C. S., & Gerke, J. 2014, to be submitted to ApJ

Kiewe, M. et al. 2012, ApJ, 744, 10

Kochanek, C. S. 2011a, ApJ, 741, 37

—. 2011b, ApJ, 743, 73

Kochanek, C. S., Szczygieł, D. M., & Stanek, K. Z. 2012a, ApJ, 758, 142

—. 2012b, ApJ, 758, 142

Kochanek, C. S. et al. 2008, ApJ, 684, 1336

—. 2012c, ApJS, 200, 8

Kourniotis, M. et al. 2014, A&A, 562, A125

Kozłowski, S. et al. 2010, ApJ, 708, 927

Larsen, S. S. 2004, A&A, 416, 537

Lee, J. C. et al. 2009, ApJ, 706, 599

Li, W., Filippenko, A. V., & Riess, A. G. 2001, ApJ, 546, 719

Liu, J. 2011, ApJS, 192, 10

Madore, B. F., Freedman, W. L., Catanzarite, J., & Navarrete, M. 2009, ApJ, 694, 1237

Maeder, A. 1981, A&A, 101, 385

Maeder, A. & Meynet, G. 1987, A&A, 182, 243

—. 1988, A&AS, 76, 411

Maraston, C. et al. 2006, ApJ, 652, 85

Marcillac, D. et al. 2006, A&A, 451, 57

Marigo, P., Girardi, L., Bressan, A., Groenewegen, M. A. T., Silva, L., & Granato, G. L. 2008, A&A, 482, 883

Massey, P. et al. 2006, AJ, 131, 2478

—. 2007, AJ, 134, 2474

Mauerhan, J. C. et al. 2013, MNRAS, 430, 1801

McMahon, R. G., Irwin, M. J., & Maddox, S. J. 2000, VizieR Online Data Catalog, 1267, 0

McQuinn, K. B. W. et al. 2007, ApJ, 664, 850

Meixner, M. et al. 2006, AJ, 132, 2268

Meynet, G., Maeder, A., Schaller, G., Schaerer, D., & Charbonnel, C. 1994, A&AS, 103, 97

Mineo, S., Gilfanov, M., & Sunyaev, R. 2012, MNRAS, 419, 2095

Miyaji, S., Nomoto, K., Yokoi, K., & Sugimoto, D. 1980, PASJ, 32, 303

Monard, L. A. G. 2008, IAU Circ., 8946, 1

Monet, D. 1998, USNO-A2.0, ed. Monet, D.

Monet, D. G. et al. 2003, AJ, 125, 984

Mora, M. D., Larsen, S. S., Kissler-Patig, M., Brodie, J. P., & Richtler, T. 2009, A&A, 501, 949

Morse, J. A., Davidson, K., Bally, J., et al. 1998, AJ, 116, 2443

Moriya, T. J., Maeda, K., Taddia, F., Sollerman, J., Blinnikov, S. I., & Sorokina, E. I. 2014, MNRAS, 439, 2917

Mould, J. et al. 2008, ApJ, 687, 230

Nantais, J. B., Huchra, J. P., McLeod, B., Strader, J., & Brodie, J. P. 2010, AJ, 139, 1413

Neill, J. D. et al. 2011, ApJ, 727, 15

Nieuwenhuijzen, H. & de Jager, C. 2000, A&A, 353, 163

Ochsenbein, F., Bauer, P., & Marcout, J. 2000, A&AS, 143, 23

Ofek, E. O. et al. 2007, ApJ, 659, L13

—. 2013, Nature, 494, 65

—. 2014a, ArXiv e-prints, 1401.5468

—. 2014b, ApJ, 781, 42

Ott, C. D. 2009, Classical and Quantum Gravity, 26, 204015

—. 2012, ArXiv e-prints, 1210.3568

—. 2007, Nature, 447, 829

Poelarends, A. J. T., Herwig, F., Langer, N., & Heger, A. 2008, ApJ, 675, 614

Poglitsch, A. et al. 2010, A&A, 518, L2

Prieto, J. L. 2008, The Astronomer's Telegram, 1550, 1

Prieto, J. L., Brimacombe, J., Drake, A. J., & Howerton, S. 2013, ApJ, 763, L27

Prieto, J. L. et al. 2008, ApJ, 681, L9

—. 2009, ApJ, 705, 1425

Pumo, M. L. et al. 2009, ApJ, 705, L138

Remillard, R. A. & McClintock, J. E. 2006, ARA&A, 44, 49

Richards, G. T. et al. 2009, ApJS, 180, 67

Rieke, G. H. et al. 2004, ApJS, 154, 25

Robinson, G., Hyland, A. R., & Thomas, J. A. 1973, MNRAS, 161, 281

Robitaille, T. P., Whitney, B. A., Indebetouw, R., & Wood, K. 2007, ApJ Supplement, 169, 328

Robitaille, T. P., Whitney, B. A., Indebetouw, R., Wood, K., & Denzmore, P. 2006, ApJ Supplement, 167, 256

Saha, A. et al. 2006, ApJS, 165, 108

Sahu, D. K. et al. 2006, MNRAS, 372, 1315

Santini, P., Fontana, A., & Grazian, A. 2009, in American Institute of Physics Conference Series, Vol. 1111, American Institute of Physics Conference Series, ed. G. Giobbi, A. Tornambe, G. Raimondo, M. Limongi, L. A. Antonelli, N. Menci, & E. Brocato, 212–215

Schlafly, E. F. & Finkbeiner, D. P. 2011, ApJ, 737, 103

Schlegel, D. J., Finkbeiner, D. P., & Davis, M. 1998, ApJ, 500, 525

Schlegel, E. M. 1990, MNRAS, 244, 269

Schneider, D. P. et al. 2010, AJ, 139, 2360

Sheth, K. et al. 2008, in Spitzer Proposal ID #60007, 60007

Siess, L. 2007, A&A, 476, 893

Silva-Villa, E. & Larsen, S. S. 2011, A&A, 529, A25

Skrutskie, M. F. et al. 2006, AJ, 131, 1163

Smartt, S. J. et al. 2009, MNRAS, 395, 1409

Smith, N. 2006, ApJ, 644, 1151

Smith, N. 2008, in IAU Symposium, Vol. 250, IAU Symposium, ed. F. Bresolin, P. A. Crowther, & J. Puls, 193–200

—. 2014, ArXiv e-prints

Smith, N. & Brooks, K. J. 2007, MNRAS, 379, 1279

Smith, N. & Frew, D. J. 2010, arXiv:astro-ph/1010.3719

Smith, N., Li, W., Silverman, J. M., Ganeshalingam, M., & Filippenko, A. V. 2011, MNRAS, 415, 773

Smith, N. & McCray, R. 2007, ApJ, 671, L17

Smith, N. & Owocki, S. P. 2006, ApJ, 645, L45

Smith, N., Vink, J. S., & de Koter, A. 2004, ApJ, 615, 475

Smith, N. et al. 2009a, ArXiv e-prints

—. 2009b, ApJ, 697, L49

Space Telescope Science Institute, . & Osservatorio Astronomico di Torino, . 2001, VizieR Online Data Catalog, 1271, 0

Stanek, K. Z. et al. 2003, ApJ, 591, L17

Stern, D. et al. 2005, ApJ, 631, 163

Stetson, P. B. 1992, 25, 297

Stoll, R. et al. 2011, ApJ, 730, 34

Stothers, R. B. & Chin, C.-W. 1996, ApJ, 468, 842

Szczygieł, D. M., Gerke, J. R., Kochanek, C. S., & Stanek, K. Z. 2012, ApJ, 747, 23

Thompson, T. A., Prieto, J. L., Stanek, K. Z., Kistler, M. D., Beacom, J. F., & Kochanek, C. S. 2009a, ApJ, 705, 1364

Thompson, T. A. et al. 2009b, ApJ, 705, 1364

Tiffany, C., Humphreys, R. M., Jones, T. J., & Davidson, K. 2010, AJ, 140, 339

Tully, R. B., Rizzi, L., Shaya, E. J., Courtois, H. M., Makarov, D. I., & Jacobs, B. A. 2009, AJ, 138, 323

Ueta, T., Meixner, M., Dayal, A., Deutsch, L. K., Fazio, G. G., Hora, J. L., & Hoffmann, W. F. 2001, ApJ, 548, 1020

van Dyk, S. D. 2005, in Astronomical Society of the Pacific Conference Series, Vol. 332, The Fate of the Most Massive Stars, ed. R. Humphreys & K. Stanek, 47

van Dyk, S. D. & Matheson, T. 2012, in Astrophysics and Space Science Library, Vol. 384, Astrophysics and Space Science Library, ed. K. Davidson & R. M. Humphreys, 249

Van Dyk, S. D. et al. 2000, PASP, 112, 1532

Véron-Cetty, M.-P. & Véron, P. 2010, A&A, 518, A10

Vink, J. S. 2012, 384, 221

Voors, R. H. M. et al. 2000, A&A, 356, 501

Wachter, S., Mauerhan, J. C., Van Dyk, S. D., Hoard, D. W., Kafka, S., & Morris, P. W. 2010, AJ, 139, 2330

Weis, K. & Bomans, D. J. 2005, A&A, 429, L13

Wesson, R. et al. 2009, MNRAS, 1823

Whelan, D. G., Johnson, K. E., Whitney, B. A., Indebetouw, R., & Wood, K. 2011, ApJ, 729, 111

Wood, K., Whitney, B. A., Robitaille, T., & Draine, B. T. 2008, ApJ, 688, 1118

Woods, P. M. et al. 2011, MNRAS, 411, 1597

Woosley, S. E. & Bloom, J. S. 2006, ARA&A, 44, 507

Woosley, S. E., Heger, A., & Weaver, T. A. 2002, Reviews of Modern Physics, 74, 1015

Wright, E. L. et al. 2010, AJ, 140, 1868

Woods, P. M. et al. 2010, MNRAS, 1801

Zhang, D. & Stanek, K. Z. 2012, Acta Astron., 62, 23